

**SIMULATION OF ENERGY STORAGE CHARACTERISTICS FOR  
ENGINEERED SOLID-STATE NANOCOMPOSITE MATERIALS**

A Dissertation  
Presented to  
The Academic Faculty

By

Blaine Costello

In Partial Fulfillment  
of the Requirements for the Degree  
Doctor of Philosophy in the  
College of Engineering  
Department of Electrical & Computer Engineering

Georgia Institute of Technology

August 2022

© Blaine Costello 2022

# **SIMULATION OF ENERGY STORAGE CHARACTERISTICS FOR ENGINEERED SOLID-STATE NANOCOMPOSITE MATERIALS**

Thesis committee:

Dr. Jeffrey A. Davis  
Department of Electrical & Computer Engineering  
*Georgia Institute of Technology*

Dr. John D. Cressler  
Department of Electrical & Computer Engineering  
*Georgia Institute of Technology*

Dr. Azad J. Naeemi  
Department of Electrical & Computer Engineering  
*Georgia Institute of Technology*

Dr. Hamid Garmestani  
School of Materials Science and Engineering  
*Georgia Institute of Technology*

Dr. Muhannad S. Bakir  
Department of Electrical & Computer Engineering  
*Georgia Institute of Technology*

Date approved: May 18, 2022

*Multiplicity is only apparent, in truth there is only one mind.*

*– Erwin Schrödinger*

For Savannah

## **ACKNOWLEDGMENTS**

I would like to thank the following people, without whom I would not be where I am today. My mother and father, who have given their unconditional love and who have shared their knowledge and insight from the beginning, motivating my pursuit of academic achievement and scientific discovery. My brothers, Zak and Luke Costello, who have given me foresight into the path laid before me. Through the lens of their own journeys through higher education they have instilled in me an appreciation for the fundamental laws of the nature. My advisor, mentor and friend, Dr. Jeffrey A. Davis, who has provided critical resources and knowledge for the refinement of my work and for my personal and professional growth.

I would also like to extend my thanks to the entire team at Georgia Tech's Partnership for Advanced Computing Environment. Their guidance enabled the utilization of critical computing infrastructure that led to the successful deployment of the simulator developed for this research. Finally, I extend my sincerest thanks and appreciation to the members of my committee, who have offered their time, attention, and perceptive insight through this arduous process.

## TABLE OF CONTENTS

<b>Acknowledgments . . . . .</b>	v
<b>List of Tables . . . . .</b>	x
<b>List of Figures . . . . .</b>	x
<b>List of Acronyms . . . . .</b>	xvi
<b>Summary . . . . .</b>	1
<b>Chapter 1: Introduction . . . . .</b>	3
1.1 Experimental Measurements Related to Energy Density in Nanoparticle Composites . . . . .	4
1.1.1 Polymer-Ceramic Composites . . . . .	5
1.1.2 Metal-Insulator Composites . . . . .	7
1.1.3 Negative Capacitance Phenomenon . . . . .	8
1.2 Modern Computational Models for Dielectric Composites . . . . .	10
1.3 Discussion of Research Opportunities . . . . .	12
1.3.1 Develop a Custom 3-D Dielectric Nanoparticle Composite Material Simulator . . . . .	12
1.3.2 Create Novel Physics-Based Breakdown Model . . . . .	13

1.3.3	Explore the Energy Density Limits of 2-Phase NP Composite Materials . . . . .	13
1.3.4	Characterize the Impact of Inclusion Conductivity on Metal-Insulator Composites . . . . .	14
1.3.5	Explore the Impact of Negative Capacitance Effects on the Dielectric Properties of Composites . . . . .	14
1.3.6	Simulate Engineered Core-Multishell Nanoparticles . . . . .	15
<b>Chapter 2: Simulator Design &amp; Implementation</b>	. . . . .	17
2.1	Discrete Representation of Simulated Nanoparticle Composite Materials . .	17
2.1.1	Percolation in Simulated Composites . . . . .	19
2.2	Quasi-Electrostatic Analysis of Simulated Composites . . . . .	20
2.2.1	Calculation of Dielectric Permittivity . . . . .	22
2.3	Verification & Validation . . . . .	24
2.4	Summary & Conclusion . . . . .	25
<b>Chapter 3: Modeling of Dielectric Breakdown in Simulated Nanoparticle Composite Materials</b>	. . . . .	27
3.1	Understanding Dielectric Breakdown . . . . .	28
3.2	Statistical Models for Dielectric Breakdown . . . . .	29
3.3	Physical Model for Dielectric Breakdown . . . . .	31
3.4	Comparison of Implemented Dielectric Breakdown Models . . . . .	32
3.5	Summary & Conclusion . . . . .	34
<b>Chapter 4: Energy Density Limits &amp; Variations in 2-Phase Nanoparticle Composites</b>	. . . . .	36
4.1	Quantifying Energy Density Limits . . . . .	36

4.1.1	Relationship Between Permittivity and Dielectric Breakdown . . . . .	37
4.1.2	Material Selection . . . . .	39
4.1.3	Simulation of Hypothetical Composites . . . . .	40
4.2	Results & Discussion . . . . .	40
4.3	Summary & Conclusion . . . . .	43
<b>Chapter 5: Quasi-Electrostatic Model Validation for Metal-Insulator Nanoparticle Composites . . . . .</b>		<b>45</b>
5.1	Model Validation Part 1: COMSOL Multiphysics® Comparisons . . . . .	48
5.2	Model Validation Part 2: Experimental Measurements . . . . .	50
5.3	Investigation of Anomalous Properties in Au and Ag Metal-Insulator-Composites	53
5.4	Summary & Conclusion . . . . .	56
<b>Chapter 6: Negative Capacitance and Internal Voltage Amplification . . . . .</b>		<b>57</b>
6.1	Negative Capacitance (NC) . . . . .	58
6.2	Simulating Voltage Amplification in Laminates . . . . .	61
6.2.1	Analytical Impedance Model . . . . .	61
6.2.2	QESIM Laminate Model . . . . .	65
6.2.3	Model Comparison . . . . .	66
6.3	Simulating Voltage Amplification in Stochastically-Arranged Composites .	68
6.3.1	Considerations for Nanoparticles With NC Interphases . . . . .	69
6.3.2	Validation Against Anomalous MIC . . . . .	71
6.4	Summary & Conclusions . . . . .	78
<b>Chapter 7: Exploration of Engineered Core-Multishell Nanoparticles . . . . .</b>		<b>81</b>

7.1	Simulation of Hypothetical Core-Multishell Nanoparticle Architectures . . . . .	81
7.2	Results . . . . .	83
7.2.1	Effective Permittivity . . . . .	84
7.2.2	Breakdown Field Strength . . . . .	85
7.2.3	Maximum Theoretical Energy Density . . . . .	86
7.3	Comparison to Hypothetical 2-Phase NP Composites . . . . .	87
7.4	Summary & Conclusions . . . . .	89
<b>Chapter 8: Conclusions &amp; Future Work</b>	. . . . .	<b>92</b>
8.1	Optimal Properties of Composites . . . . .	92
8.2	Exploration of Metal-Insulator Composites . . . . .	93
8.3	Simulation of Engineered Core-Multishell Nanoparticles . . . . .	94
8.4	Future Work . . . . .	95
<b>Appendices</b>	. . . . .	<b>97</b>
Appendix A: Derivations . . . . .	98	
<b>References</b>	. . . . .	<b>120</b>

## LIST OF TABLES

4.1	Table of material properties obtained from [52] and [16] used as host or inclusion materials in the simulation of hypothetical high-energy-density NP composites in [50] with the host material in bold for comparison. . . . .	40
6.1	Comparison of results from effective real permittivity ( $\epsilon'_{eff}$ ) approximation obtained using QESIM to equivalent data obtained using the analytical impedance model at 1kHz for bi-phase laminates as derived in this chapter. .	67
6.2	Comparison of results from effective conductivity ( $\sigma_{eff}$ ) approximation obtained using QESIM to equivalent data obtained using the analytical impedance model at 1kHz for bi-phase laminates as derived in this chapter. .	67
6.3	Constituent material simulation parameters used to recreate anomalous data reported in [22] and [21]. . . . .	71
7.1	Permittivity of constituent materials for best-case core-multishell NP architecture with a BaTiO <sub>3</sub> core and a P(VDF-HFP) host with possible analogous real materials and their measured permittivities as reported in [52]. .	90
7.2	Permittivity of constituent materials for best-case core-multishell NP architecture with a SiO <sub>2</sub> core and a P(VDF-HFP) host with possible analogous real materials and their measured permittivities as reported in [52]. . . . .	91

## LIST OF FIGURES

1.1 Juxtaposition of different classifications of capacitive energy storage materials based on (a) number of publications as reported in [2] and (b) dielectric permittivity, breakdown strength, and energy density from [4]. . . . .	4
2.1 Discretization scheme used to represent the analogous physical material systems simulated in this work. . . . .	18
2.2 3D visualization depicting (a) a single voxellated NP and (b) a simulated NP composite material geometry, each consisting of two distinct material phases. . . . .	18
2.3 Histogram representing the distribution of percolating configurations $\alpha$ , $\beta$ , and $\gamma$ with respect to volume fraction. . . . .	20
2.4 Cross-section of a simulated NP composite material geometry consisting of high-k NPs immersed in a low-k insulating dielectric host. The arrangement of NPs and the resultant electric fields both exhibit periodicity about the horizontal boundaries as intended. . . . .	23
2.5 Error convergence for QESIM's 7-point Laplace approximation, evaluating the error associated with effective permittivity ( $\varepsilon_{eff}$ ) in simulated (a) laminate-structured composites and (b) composites with spherical inclusions. . . . .	24
2.6 Comparison of simulated effective composite permittivity data for a simulated grid size of $65 \times 65 \times 65$ voxels with permittivity data reported in [16] and approximations obtained using the analytical Bruggeman model. . . . .	25
3.1 Cross-section of (a) the simulated internal electric field of a NP composite and (b) the breakdown path through the electric field at breakdown voltage ( $V_{BD}$ ). . . . .	32

3.2 Comparison of breakdown strength data reported in [16] to simulated composite breakdown field strength data obtained using (a) average electric field models, and (b) breakdown path model. . . . .	33
4.1 Inverse relationship between permittivity and breakdown field strength from [52] depicted as contours of constant energy density juxtaposed against measured data from [16], [53], and [10]. A black dotted line marks a supposed boundary imposed by the two materials with highest reported energy density among pure materials and blue, yellow, and red dotted lines represent constant energy densities equal to that of the pure host materials in [16],[53], and [10], respectively. . . . .	37
4.2 Simulated composite material data from four cases of different NP inclusion materials based on thin film measurements reported in [52]. The dashed lines represent contours of constant energy density corresponding to each constituent material. . . . .	41
4.3 Scatterplot with mean and $3\sigma$ variation overlay depicting the theoretical maximum energy density ( $u_{max}$ ) calculated with practicality factor $\zeta = 0.5$ . P(VDF-HFP) composites with inclusions of (a) BaTiO <sub>3</sub> , (b) SrTiO <sub>3</sub> ,(c) SiO <sub>2</sub> , and (d) HfO <sub>2</sub> are shown. Each data set consists of over 1200 simulated geometries. . . . .	42
4.4 Maximum theoretical energy density observed in simulation results for each geometric percolating configuration within each inclusion material data set. Pie charts at the top of each bar show the volume fraction of inclusions at which the maximum energy density value is observed. Listed below the x-axis is a table of the dielectric properties associated with each inclusion material obtained from [52]. . . . .	43
5.1 Validation of QESIM for conductive NPs in a lossy insulating host against analogous COMSOL model for nanolaminates with a single metallic layer of thickness equal to (a) 10 nm, (b) 20 nm, and (c) 30 nm. . . . .	49
5.2 Validation of QESIM for conductive NPs in a lossy insulating host against analogous COMSOL model for NPs with radius equal to (a) 20 nm, (b) 30 nm, and (c) 40 nm. . . . .	49
5.3 Comparison of measured data to analogous simulated data for (a) effective composite permittivity and (b) loss tangent consistent with experimental descriptions of Cu in a polyurethane host as provided in [20]. . . . .	51

5.4	Comparison of measured data to analogous simulated data for (a) effective composite permittivity and (b) loss tangent consistent with experimental descriptions provided in [19] for Cu in a PVC host. . . . .	52
5.5	Comparison of measured data to analogous simulated data for (a) effective composite permittivity and (b) loss tangent consistent with experimental descriptions provided in [19] for Al filler immersed in a PVC host. . . . .	53
5.6	Comparison of measured effective composite permittivity from (a) [22] at 1 MHz, and (b) [21] at 1kHz to analogous simulated data. . . . .	54
5.7	Comparison of measured effective loss tangent from (a) [22] at 1 MHz, and (b) [21] at 1kHz to analogous simulated data. . . . .	54
5.8	Comparison of measured effective breakdown strength from (a) [22] at 1 MHz, and (b) [21] at 1kHz to analogous simulated data. . . . .	55
6.1	Simplified internal voltage diagrams for MIM capacitor consisting of one insulating layer (white) adjacent to a layer (gray) with (a) equal permittivity, (b) higher permittivity, (c) infinite permittivity (i.e. conducting), and (d) negative permittivity, where the proportionality to internal voltage amplification across the white insulating layer is noted. . . . .	59
6.2	Circuit-level diagrams depicting of (a) physical model, (b) equivalent circuit model, (c) impedance model, and (d) lumped impedance model. . . . .	62
6.3	Plots of internal potential field within simulated MIM capacitors simulated at 1kHz, consisting of one 200nm dielectric insulating layer (white) adjacent to a 50nm layer (gray) exhibiting (a) equal permittivity, (b) higher permittivity, (c) conductive properties, and (d) negative capacitance. . . . .	66
6.4	Plots depicting the dependence of effective permittivity on NC layer thickness for bi-phase NC heterostructure at (a) high-frequency and (b) low-frequency, and the dependence of effective conductivity on NC layer thickness at (c) high-frequency, and (d) low-frequency. Design equations are employed to further express the efficacy of the analytical model for the prediction of geometric and material property combinations that lead to polarization catastrophe. . . . .	68

6.5 Illustration of internal electric field distribution within composites consisting of (a) positive dielectric adjacent to planar laminate metallic region, (b) positive dielectric adjacent to curved metallic region, (c) NC planar heterostructure adjacent to planar laminate metallic region, (d) NC curved heterostructure adjacent to curved metallic region, and a cross section of the simulated electric field from NP MIC showing (e) the relative width of high-electric-field regions adjacent to metallic spheres, and indicating the proposed shell thickness ( $t_{shell}$ ) as a function of the NP radius ( $r_{np}$ ). . . . .	70
6.6 Comparison of simulated effective permittivity data on Au-Al <sub>2</sub> O <sub>3</sub> MIC obtained using QESIM to measured data reported in [22] showing (a) a complete scatterplot including all simulated cases, (b) the mean and standard deviation of simulated data at each volume fraction, (c) a partial scatterplot showing the low-volume-fraction cases, and (d) the mean and standard deviation of simulated data for low-volume-fractions. . . . .	73
6.7 Comparison of simulated effective permittivity data on Ag-epoxy MIC obtained using QESIM to measured data reported in [21] showing (a) a complete scatterplot including all simulated cases, (b) the mean and standard deviation of simulated data at each volume fraction, (c) a partial scatterplot showing the low-volume-fraction cases, and (d) the mean and standard deviation of simulated data for low-volume-fractions. . . . .	74
6.8 Comparison of simulated loss tangent data on Au-Al <sub>2</sub> O <sub>3</sub> MIC obtained using QESIM to measured data reported in [21] showing (a) a scatterplot of NC data (blue) and non-NC data (red) and (b) the mean and standard deviation of simulated data at each volume fraction. . . . .	75
6.9 Comparison of simulated loss tangent data on Ag-epoxy MIC obtained using QESIM to measured data reported in [21] showing (a) a scatterplot of NC data (blue) and non-NC data (red) and (b) the mean and standard deviation of simulated data at each volume fraction. . . . .	75
6.10 Comparison of simulated breakdown field strength data on Au-Al <sub>2</sub> O <sub>3</sub> MIC obtained using QESIM to measured data reported in [21] showing (a) a scatterplot of NC data (blue) and non-NC data (red) and (b) the mean and standard deviation of simulated data at each volume fraction. . . . .	76
6.11 Comparison of simulated breakdown field strength data on Ag-epoxy MIC obtained using QESIM to measured data reported in [21] showing (a) a scatterplot of NC data (blue) and non-NC data (red) and (b) the mean and standard deviation of simulated data at each volume fraction. . . . .	76

6.12 Comparison of simulated maximum energy density on Au-Al <sub>2</sub> O <sub>3</sub> MIC obtained using QESIM to measured data reported in [22] showing (a) a scatterplot of NC data (blue) and non-NC data (red) and (b) the mean and standard deviation of simulated data at each volume fraction. . . . .	78
6.13 Average of simulated effective permittivity values obtained using QESIM with the NC interphase model (blue line), juxtaposed against non-NC QESIM data (red points) and measured data reported in [21] (black line). . . . .	79
7.1 Illustration of simulated core-multishell architectures with linear and logarithmically-graded permittivity shells at a single volume fraction of 6% (for $t_{shell} \approx 13nm$ ) for (a) no shells, (b) one shell, (c) two shells, (d) three shells, and (e) four shells. . . . .	82
7.2 Cross-sections of internal electric field magnitudes (scaled to the colorbar shown) within simulated NP architectures depicting the re-distribution of electric fields into the NP shell structure for (a) linearly-graded and (b) logarithmically-graded shell permittivities. . . . .	84
7.3 Effective composite permittivity of simulated core-multishell NP architectures with (a) linearly-graded shells with a total thickness of 6.5nm, (b) logarithmically-graded shells with a total thickness of 6.5nm, (c) linearly-graded shells with a total thickness of 13nm, and (d) logarithmically-graded shells with a total thickness of 13nm. . . . .	85
7.4 Effective dielectric breakdown field strength of simulated core-multishell NP architectures with (a) linearly-graded shells with a total thickness of 6.5nm, (b) logarithmically-graded shells with a total thickness of 6.5nm, (c) linearly-graded shells with a total thickness of 13nm, and (d) logarithmically-graded shells with a total thickness of 13nm. . . . .	87
7.5 Maximum theoretical energy density of simulated core-multishell NP architectures with (a) linearly-graded shells with a total thickness of 6.5nm, (b) logarithmically-graded shells with a total thickness of 6.5nm, (c) linearly-graded shells with a total thickness of 6.5nm, and (d) logarithmically-graded shells with a total thickness of 6.5nm. . . . .	88
7.6 Maximum theoretical energy density of core-multishell composites with logarithmically-graded shell permittivities and shell thickness $t_{shell} = 13nm$ . . . . .	89
A.1 Illustration of finite difference grid used to represent 3-D simulated window. . . . .	98

- A.2 illustration of localized spatial considerations for quadrature using uniform cubic finite difference grid showing (a) the dielectric permittivity cell grid and (b) the 7 indexed points that make up the localized scalar potential field. . . . . 103
- A.3 Circuit-level diagrams depicting of (a) physical model, (b) equivalent circuit model, (c) impedance model, and (d) lumped impedance model. . . . . 112

## SUMMARY

The objective of this research is to better understand the limits and opportunities of nanoparticle (NP) composite materials as solid-state capacitive energy storage media. As such, this dissertation explores the energy density characteristics and the inherent variations in a broad array of different nanocomposite materials through the development of a generalized, high-throughput simulation tool which accurately approximates the electric field and conduction current within a large number of randomly generated composite materials. In addition, a new physics-based model is developed, validated, and employed to accurately approximate the breakdown voltage of heterogeneous materials for capacitive energy storage devices. The resulting data sets allow for the accurate approximation of the energy storage properties associated with realistic nanoparticle composite materials given only the material properties and geometric arrangement of the constituent material phases. This simulation platform is initially validated against published measured data on effective permittivity, breakdown strength, loss characteristics, and energy density and is subsequently used to explore a number of hypothetical composites.

A series of simulation experiments performed in this research explore the limits and variations in energy storage properties for various hypothetical nanocomposite materials utilizing constituent materials with a broad range of dielectric properties. First, the energy density of various hypothetical polymer-ceramic composites is approximated, and it is found that, contrary to conventional wisdom, the optimal filler materials are actually those with lower permittivities and higher breakdown strengths. Next, metal-insulator composites (MIC) are simulated using a quasi-electrostatic model, which uncovers the possible formation of negative-capacitance domains for certain metal-insulator combinations. Subsequently, a set of equations are derived for the design of induced-polarization-catastrophe in laminate-structured composites with a negative capacitance (NC) layer that results in a dramatic increase in device capacitance. This concept is extrapolated into 3-D, and ex-

plored further in the context of metallic nanoparticle composite materials using the simulator developed in this work. It is found that the limits of effective permittivity in capacitive metal-insulator dielectrics are in fact much higher than predicted with traditional electromagnetic models for materials. Finally, an exploration into advanced nanoparticle engineering of core-multishell nanoparticles is performed, which indicates an opportunity for up to 28.5% increase in maximum energy density because of an enhancement of effective composite breakdown strength. In total, this research uses a custom material simulator to provide valuable insight into the limits and opportunities associated with a broad range of solid-state nanoparticle composite materials. This work aims to guide ongoing research efforts towards the development of next generation solid-state energy storage materials.

## CHAPTER 1

### INTRODUCTION

The present growing global energy demand necessitates continued research into energy storage technologies for the development of low cost, high energy density devices. Current state-of-the-art high energy density energy storage technologies, like lithium-ion cells and electrochemical double-layer capacitors (EDLC), rely on ionic charge transport and storage. Despite their high energy density, this mode of energy storage has several drawbacks. First, because ionic charge carriers are larger and have more mass than electrons, electrochemical energy storage devices tend to exhibit slower rates of charge transport and longer recharge/discharge cycle times compared to electrostatic energy storage devices [1]. Second, the size of charge carriers in electrochemical energy storage devices can lead to accelerated degradation and greater losses from excessively rapid charge and discharge cycles [2]. Finally, in terms of lifetime (i.e. recharge/discharge cycles), solid-state capacitive energy storage devices outperform electrochemical energy storage devices by an order of magnitude or more [3].

Recent research efforts have generated a broad body of work on the topic of capacitive energy storage technology with a current focus on polymer-based composites due to their low cost, flexibility, processability, etc. Specifically, analysis in [4] highlights the superior volumetric energy density and breakdown strength observed in polymer/ceramic composites as illustrated in Figure 1.1(b), and researchers in [5] support this by stating that energy densities associated with polymer/ceramic composites range from 10-30 [ $\frac{J}{cm^3}$ ]. The number of publications on materials for capacitive energy storage has also grown exponentially from 2008 to 2017 as indicated in Figure 1.1(a), with a steady increase in publications specifically studying polymer/ceramic composites [2].

As such, this chapter will start with an overview of current explorations of polymer/ceramic

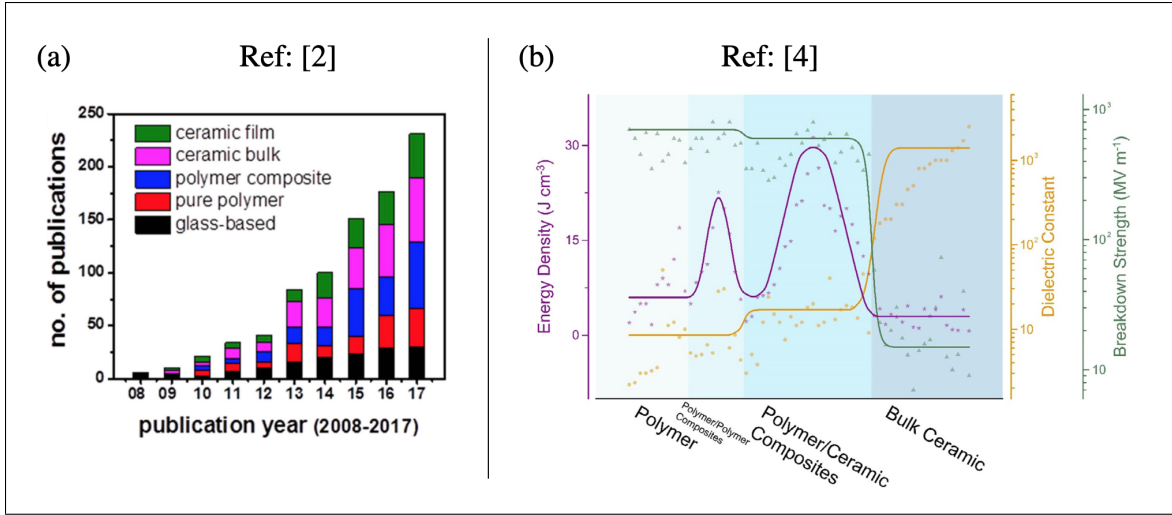


Figure 1.1: Juxtaposition of different classifications of capacitive energy storage materials based on (a) number of publications as reported in [2] and (b) dielectric permittivity, breakdown strength, and energy density from [4].

composite materials. Notable results from several experimental works are discussed to quantify the current measurements for energy density in polymer-ceramic composites. This overview on polymer/ceramic composites is then contrasted to several anomalous and unexplained phenomena reported in a series of works examining metal-insulator-composites. A body of literature centered around the concept of negative-conductivity and interphase chemistry is then presented for the first time as a possible explanation for such observed anomalies among metal-insulator composites. Finally, to provide a context for the simulation platform developed in this research, a number of publications that focus on computational modeling are summarized to understand the state-of-the-art of current numerical tools and analytical models.

## 1.1 Experimental Measurements Related to Energy Density in Nanoparticle Composites

The overarching goal of this body of work is to explore and quantify the limits and variations associated with the energy storage properties of a broad range of nanoparticle (NP) composite materials. As such, a myriad of inclusion materials are examined, and these

inclusion materials can be categorized as either conductive (e.g. metallic) or insulating (e.g. ceramic). This chapter examines the literature surrounding NP composite materials containing ceramic inclusions, metallic inclusions, or some combination of the two. Recent progress in the development of high energy density composites has shown that certain composites can match or even exceed energy densities generally associated with modern EDLC [4].

The foundation of a polymer-based composite is the host polymer matrix in which the NP inclusions are dispersed. Dielectric polymers in their purest form generally exhibit high breakdown strength but low energy densities because of their low permittivity. To improve the energy density of these materials, ceramic inclusions can be introduced to enhance certain dielectric properties [6] [7]. Many factors associated with the NP inclusion have been shown to influence the dielectric properties of the overall composite, including size and shape, material properties, volume fraction, NP separation, etc. Based on these factors, a wide range of approaches have been employed to boost energy density while maintaining a reasonably high charge-discharge efficiency. This subsection discusses both several polymer-ceramic composites that have been found to exhibit the highest energy densities in the current literature, and several metal-insulator composites that have been found to exhibit anomalous and seemingly inexplicable dielectric properties.

### 1.1.1 Polymer-Ceramic Composites

Analyses in [8] and [9] indicate that high-k inclusions are often associated with greater losses and lower breakdown strength, which are potentially caused by electric field gradients that are steeper near NP inclusions due to large differences between the permittivities of the NP and the host materials. To address this, several works have explored the effects of using surface-modified NPs immersed in a polymer host. For example [10] details the synthesis and characterization of BaTiO<sub>3</sub>/PVDF NP composites to test the effects of Polyvinylpyrrolidone (PVP) surface modifications on the energy density of resulting com-

posites. A maximum energy density of  $6.8 \text{ [J/cm}^3\text{]}$  was observed in the samples with surface modified NPs at a volume fraction of 10% which represents an 89% improvement over the samples with unmodified NP inclusions. It is suggested in [6] that these contributions to energy density could also be associated with the increased separation of NPs due to surface-modification, which is consistent with observations in [11], and [12].

Core-shell NP composites offer another solution to enhance the separation within NP composites. By encasing the NP cores in a different material, a third material phase is added to the composite that provides a barrier between NP cores that can prevent clustering and even percolation at higher volume fractions. The preparation of core-shell NP composites has also been associated with some improvements in breakdown strength and energy density [13]. The most notable example of these core-shell NP composites is discussed in [14], that exhibit energy densities of up to  $21.51 \text{ [J/cm}^3\text{]}$  in poly(glycidyl methacrylate) (PGMA) polymer films containing glycidyl methacrylate (GMA)-coated BaTiO<sub>3</sub> NPs. In addition, [15] details an exploration into core-multishell architectures that has shown promise in mitigating losses while maximizing energy density in composites with core-double-shell NP filler. Other works like [16] and [17] explore the effects of including surface modified NPs using fluorinated phosphoric acid and BaTiO<sub>3</sub> NPs, respectively.

While promising results have been reported in the realm of NP composite materials, analysis in [4] indicates that composites with non-spherical inclusions can exhibit a 35% improvement in energy density over similar NP composites. In [9], BaTiO<sub>3</sub> NPs are used to modify the exterior of cylindrical TiO<sub>2</sub> nanowires, and the resulting inclusions exhibit energy densities of up to  $9.95 \text{ [J/cm}^3\text{]}$ , which is nearly three times that of the biaxially-oriented polypropylene (BOPP) host polymer. In addition, a ternary composite containing a combination of boron nitride nanosheets and BaTiO<sub>3</sub> NPs has been shown to exhibit an energy density of as much as  $21.2 \text{ [J/cm}^3\text{]}$  in [18]. By far, however, the maximum observed energy density in any polymer composite to date is that of the novel nanofiber inclusions synthesized and characterized in [7]. These novel inclusions consist of BaTiO<sub>3</sub> NPs embedded

within  $\text{TiO}_2$  nanofibers, leading to an improvement in energy density of 84% and 27% when compared to composites containing only NPs or pure  $\text{TiO}_2$  nanofibers respectively. The maximum energy density achieved with these exotic composites is as much as 31.2  $[\frac{\text{J}}{\text{cm}^3}]$ , exceeding that of commercially available electrochemical capacitors. In total, this prior research underscores an opportunity for future development of optimal inclusions and material combinations that could lead to even higher energy densities, thereby paving the way to ultra-high energy density capacitive dielectrics.

### 1.1.2 Metal-Insulator Composites

Metal-insulator composites (MIC) have long been known to exhibit sub-optimal energy storage properties when compared to polymer-ceramic and other insulator-insulator composites. This is largely due to the excessive buildup of electric fields near the interfaces between the metal NP and the host dielectric [4]. Usually, this also leads to a lower breakdown strength and subsequently lower maximum theoretical energy density. These detrimental properties are generally only amplified as volume fraction is increased. As such, MIC have largely been neglected as energy storage media [3]. Instead, MIC are studied primarily for sensing applications, where the frequency dependence or temperature dependence of effective permittivity, conductivity, and loss characteristics are far more critical than breakdown strength or energy density.

The greater body of literature on MIC also suggests considerable variability among effective permittivity measurements reported for different MIC. While works like [19] and [20] exhibit slight improvements in dielectric permittivity when compared to the pure host material, recent results in [21] have shown significant improvements in effective relative permittivity up to 320 at a volume fraction of 22%. This represents an increase in effective permittivity of nearly two orders of magnitude compared to the pure epoxy host which has a relative permittivity of 3.6.

In some cases, exceptionally low volume fractions of metallic inclusions have resulted

in immense improvements in dielectric constants. Specifically, [22] reports permittivity values that are nearly four times that of the host dielectric at a volume fraction of Au inclusions of just 4%. This seemingly anomalous behavior underscores an opportunity for continued research into metal-insulator composites to better understand the phenomena that lead to such an exceptional result. One such phenomenon that is explored in later chapters of this work is the possible formation of negative capacitance regions at the interphase between metallic NPs and the insulating host dielectric. It is proposed for the first time in this dissertation that this particular type of interphase formation can result in extremely high effective permittivities at low frequencies for these low-volume-fraction MIC materials. This phenomenon could be similar to that which has been observed in the current literature in devices containing ferroelectric materials in series with a paraelectric material. The negative capacitance of ferroelectric materials has even been leveraged in a number of publications to improve the loss characteristics and switching time of MOSFET devices [23] [24].

### 1.1.3 Negative Capacitance Phenomenon

In recent years, the observation of negative capacitance (NC) in certain heterogeneous materials has become a subject of active research and development [24] [25] [26] [27]. Many recent publications highlight the complexity of materials that exhibit NC, noting that the current literature provides limited insight into the physical nature of NC [23] [27]. In essence, NC can be understood as an inverted polarization within one of multiple distinct dielectric material domains within a composite. The inverted polarization in the NC domain effectively amplifies the voltage across the adjacent dielectric material domains, which allows for stronger total polarization for the entire material system. Several works have likened this effect to the physical phenomenon that occurs in Schottky diodes, associated with the formation of a depletion region due to the diffusion of carriers and the built-in potential that forms across the metal-semiconductor junction [28] [29]. Unlike the Schottky

diode, however, bi-phase heterostructures containing one NC domain can also exhibit negative differential conductivity (NDC). This means that under certain conditions, increased applied potential can reduce current flux as well as internal electric field magnitude [30] [23].

The stability of NC effects in various material systems has been a subject of discussion in recent works like [28] and [29]. In [28], a phenomenological model is presented which relates the Curie temperature and temperature of device operation to the emergence of NC properties in the context of a linear, 1-dimensional chain of polarizable units. Alongside this model, it is stated that DC-stable NC effects would not be possible due to their assumed transient nature associated with their various dielectric relaxation times. It is also mentioned in [31] that this NC effect is generally unstable, which implies that the observation of NC in AC systems would not translate to DC systems. However, this limitation has more recently been refuted by [29], which indicates the possibility of stable NC effects at DC in materials consisting of a sufficiently thin NC layer that is adjacent to a traditional dielectric layer.

It is assumed in [26] that this NC effect is related to hysteretic polarization that occurs within ferroelectric materials, but recent work in the area of interphase chemistry indicates that hysteretic behavior can manifest at the interphase between certain combinations of materials. Many publications like [23] and [24] highlight the role of hysteretic polarization in the interphase between the ferroelectric and paraelectric domains which leads to negative differential conductivity and subsequently NC effects. Specifically, the researchers in [32] have noted the presence of a charge-trapping layer along the interphase of hydrogen-terminated diamond leading to the observation of NC in the absence of any ferroelectricity due to a high density of trap states in the interphase region. Like the hydrogen-terminated-diamond interphase, material interphases in a general sense are likely to contain a relatively high density of trap states, dangling bonds, and other defects [33] [34]. In [27], the emergence of NC properties in materials is attributed to photonic excitation in perovskite solar

cells, and it is stated that defect-induced energy band over-bending leads to interfacial charge-trapping in such systems. Furthermore, [35] discusses the inherent connection between the density of charge trapping states and hysteresis, suggesting that non-ferroelectric interphases can exhibit some ferroelectric properties due to an excessive density of trap states. Little is known about the emergence of such properties in interphase regions within composites; however, the greater body of research into composites and NC materials implies a possible connection between the emergence of NC properties at certain material interphases and anomalous properties observed in many experimental works like [34], [21], and [22].

With the complexity of interphase chemistry as a topic of active research and the lack of experimental data on the dielectric properties of exotic interphases, there are a multitude of unknowns and much to be discovered within this space. In essence, many works have described the same phenomenon in the context of various different applications and device types. This combined body of work points to the emergence of properties in heterogeneous material systems where opposing internal electric fields lead to a marked increase in the effective polarizability of the device as a whole while maintaining a reduction in losses. The mere existence of this effect implies a broad array of possible applications including energy storage, wherein equally-opposing electric fields may lead to greater energy densities in capacitive dielectrics than was previously thought to be possible. The work in this dissertation will take this NC effect into consideration when quantifying the limits and variations associated with the dielectric properties of composite materials.

## 1.2 Modern Computational Models for Dielectric Composites

The NP composite materials studied in this work can be generalized as highly disordered insulating materials due to the stochastic distribution of inclusions within the host matrix [36]. Modeling the dielectric properties of such materials generally involves the calculation of electric fields within some discrete simulation mesh that represents the internal

structure of the simulated composite. Ultimately, the difference in the dielectric properties between the inclusions and the host material leads to perturbations in the internal electric fields which presently cannot be directly measured through experimentation. The numerical methods discussed in this section calculate these perturbed internal electric fields to obtain a range of effective dielectric properties for simulated composites, such as effective dielectric permittivity and average breakdown field strength.

The effective dielectric permittivity of a material can be calculated from the total internal electric fields generated by an applied voltage across the material in a parallel-plate capacitor configuration [37]. To explore the permittivity associated with NP composite materials, measured data is compared to simulated values obtained using this method in [16], [38], and [39], which shows a high degree of correlation between measured and simulated permittivity. Similarly, nanofiber composites have been explored in [40], [41], and [9] illustrating the efficacy of this method for the prediction of dielectric permittivity in composites with high aspect-ratio inclusions as well.

The aforementioned works primarily focus on the calculation of permittivity and do not strongly consider the variances in breakdown strength associated with randomly dispersed inclusions. For example, in [39] and [16], the breakdown strength of the simulated composites is determined by simply comparing the average of the internal electric fields within the host to the breakdown strength of the host material. While this provides a rough estimate of breakdown strength, it fails to capture the geometry-induced variations due to the weakest-link behavior associated with breakdown events as discussed in [42].

Currently, the computational models most physically analogous to the process of dielectric breakdown are those which consider the propagation of electrical trees. Such methods are employed in [43], [44], and [45] to explore the relationship between the measured breakdown strength of materials and the breakdown strength obtained using electrical tree simulations. In each of these works, an iterative algorithm is employed based on the internal electric fields that simulates the propagation of electrical trees through a dielectric

over time under a range of applied voltages. The resulting electrical trees are used to determine the breakdown voltage at which a conductive path is formed from one electrode to the other. Each of these works also considers the degradation of devices over time due to non-destructive internal breakdown events that weaken the insulating material during normal operation. In general this method has been found to be highly effective in predicting the breakdown strength of composites [45]. It should be noted, however, that because this method generally operates in the time-domain, it is very computationally intensive, especially for large 3-D geometries.

### **1.3 Discussion of Research Opportunities**

This chapter has identified several opportunities for contributing to the greater body of knowledge in the area of composite materials for energy storage applications. This section summarizes the research opportunities that have been identified in the literature as detailed in previous sections. In addition, the core contributions to knowledge associated with each distinct research opportunity are briefly summarized.

#### 1.3.1 Develop a Custom 3-D Dielectric Nanoparticle Composite Material Simulator

Simulation efforts referenced in this chapter have illustrated the efficacy of various electric-field-based models for the calculation of the dielectric properties of composites related to energy storage. It is therefore reasonable to assume that similar computational models can be employed to guide the future development of optimal energy storage materials. The previously discussed works largely rely on data generated using only a small set of geometries due to the high computational load associated with such simulations. To date, the author is not aware of works focused on the simulation of notably large sets of randomly dispersed composite geometries that aim to quantify the limits and variability of the dielectric properties of composites.

Because this indicates an opportunity for exploration, the first contribution of this work

is the development of a custom simulator of internal electric fields within composite materials. This custom simulator, referred to as QESIM (Quasi-Electrostatic Simulator of Inhomogeneous Materials), provides a framework through which the dielectric properties for a large number of unique, stochastically-generated material arrangements can be approximated. QESIM is used in all future contributions of this body of work as it allows for the parallel simulation of a large number of pseudorandomly-generated NP composite geometries, as it is designed to utilize one of Georgia Tech's high performance computing (HPC) environments known as the Partnership for Advanced Computing Environment (PACE).

### 1.3.2 Create Novel Physics-Based Breakdown Model

Simulation frameworks referenced previously in this chapter primarily focus on the estimation of dielectric permittivity and largely neglect the approximation of breakdown field strength due to the significant computation time requirements. To address this, this second contribution centers around the development and implementation of a novel, physics-based breakdown model for the approximation of effective breakdown field strength in heterogeneous materials while using fewer computational resources. This new breakdown model is based on the physical process of dielectric breakdown and shows a marked improvement in its ability to approximate both the mean and variance of breakdown strengths for experimental data taken from real-world NP composite materials.

### 1.3.3 Explore the Energy Density Limits of 2-Phase NP Composite Materials

Few works in the literature simulate novel or hypothetical NP materials, but instead most only model material combinations that have experimental counterparts. There are still a multitude of unexplored NP-host combinations. To address this, a set of new inclusion material combinations are selected in this thesis and simulated within a polymer host. The resulting composites are compared based on their maximum theoretical energy density as

determined by QESIM. These results highlight distinct opportunities for the exploration of low-k, high dielectric strength NPs that could lead to high breakdown strength composites, thereby maximizing their energy densities. Some of the results in this thesis oppose the common notion that the optimization of energy density is best approached through the inclusion of high-permittivity filler. Further support for these findings is provided in later chapters, providing potentially unique guidance towards the development of next-generation energy storage materials with moderate permittivity and high dielectric strength.

#### 1.3.4 Characterize the Impact of Inclusion Conductivity on Metal-Insulator Composites

The anomalous experimental results in the literature for metal-insulator composites (MIC) necessitate additional simulated exploration into such composite materials. As such, this fourth contribution aims to validate the accuracy of QESIM for the simulation of composites consisting of metallic inclusions immersed in an insulating dielectric host material. The validated simulator and the results obtained therein provide insight into the fundamental limits of MICs at low volume fractions. This exploration has uncovered a possible negative capacitance effect in these materials which could provide a possible explanation for the anomalous results observed in Au and Ag NP composites that are reported in [21] and [22].

#### 1.3.5 Explore the Impact of Negative Capacitance Effects on the Dielectric Properties of Composites

One byproduct of the exploration associated with the previous contribution has been the realization of the potential for unusual material properties at various types of interphases. In particular, recent research points to the possibility of ferroelectric domain formation within specific interphase regions between NP and host due to a high density of charge-trapping states. To address this in the context of the simulation efforts detailed in this work, an analytical impedance model for bi-phase heterostructures containing a single NC

domain is developed and used to obtain frequency-dependent material design equations. These design equations are intended to provide insight into the material and geometric parameters required to induce internal voltage amplification. The design equations are then used to define interphase properties capable of reproducing the anomalous data observed in certain metal-insulator-composites using the QESIM material simulation framework. The successful prediction of experimental data implies a possible explanation for the anomalous data reported in a number of works in the area of MIC. Furthermore, later chapters will introduce the concept of internal voltage amplification as a mechanism through which total energy within a composite can be maximized beyond the limits of traditional dielectric materials. This further underscores the importance of breakdown strength in energy storage materials as the true limiting factor of energy density.

### 1.3.6 Simulate Engineered Core-Multishell Nanoparticles

Many experimental works have explored core-shell NP composite materials as a means to enhance NP separation and prevent NP clustering within a material. They have been associated with enhanced breakdown strength in [13] and observations of consistent high efficiency under high electric fields in [15] are met with the suggestion of further research into the topic of core-multishell NPs in [46]. Because of the difficulty associated with fabricating core-multishell NP, however, the engineering of core-multishell NP is an area of research that remains largely unexplored in the literature. To quantify the possible energy density limits that could be expected in core-multishell NP composites, this final contribution centers around a series of simulations that aim to identify optimal-energy-density core-multishell NP architectures. It is hypothesized that these core-shell NP architectures can be engineered to enhance the breakdown field strength in NP composites, thus leading to greater maximum energy densities. This contribution seeks to provide valuable insight into optimal NP composite architectures that have not yet been studied by experimentation toward the future development of next-generation energy storage materials that contain

engineered core-multishell NP fillers.

## CHAPTER 2

### SIMULATOR DESIGN & IMPLEMENTATION

This chapter focuses on how first-principles physics has guided the design and implementation of the core simulator employed in this document. The simulator discussed here has been designed to generate large quantities of simulated data to predict the dielectric properties associated with specific composites consisting of two or more unique material phases. The core assumption here is that the mean and variance of a large set of randomly-generated geometries, each with a relatively small simulated window, can be used to accurately predict properties of real-world composite materials, including their theoretical limits and expected material fluctuations due to variations in microstructure. Specifically, this work examines NP composite materials because of the high surface-area-to-volume ratio associated with nano-scale spherical inclusions. This simulator can be considered in two parts; (1) material generation and (2) quasi-electrostatic analysis.

#### **2.1 Discrete Representation of Simulated Nanoparticle Composite Materials**

The first stage of this simulator is the generation of the geometric configuration of the simulated material. In order to obtain a numerical approximation for parameters relating to energy storage, a model must be created that is both physically and functionally analogous to a real-world capacitive energy storage device. In this simulation space volume, two or more unique material phases may exist, each with unique material properties that lead to geometry-dependent electric field fluctuations within the volume. Mathematically, if the geometric state is specified in sufficient detail, it is possible to use this geometric arrangement to predict the effective dielectric properties of the resulting bulk composite. The uniform, cubic-cell finite difference grid that represents the simulated window ( $\Omega$ ) for a single composite geometry is illustrated in Figure 2.1.

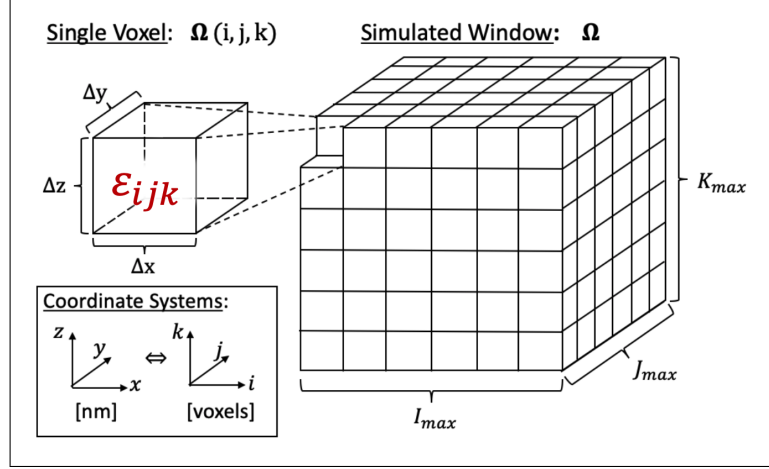


Figure 2.1: Discretization scheme used to represent the analogous physical material systems simulated in this work.

The geometry is arranged such that the cubic cell at location  $\Omega_{ijk}$  has material properties consistent with the constituent phase at point  $(i, j, k)$ . The voxel at each index represents one of the constituent phases, and the entire 3-D volume represents an abstraction of a real nanoparticle (NP) composite system as pictured in Figure 2.2. The material generation code used to generate Figure 2.2 was built to generate pseudorandom geometric arrangements of spherical NPs. This allows for the acquisition (and statistical analysis) of large sets of simulated data.

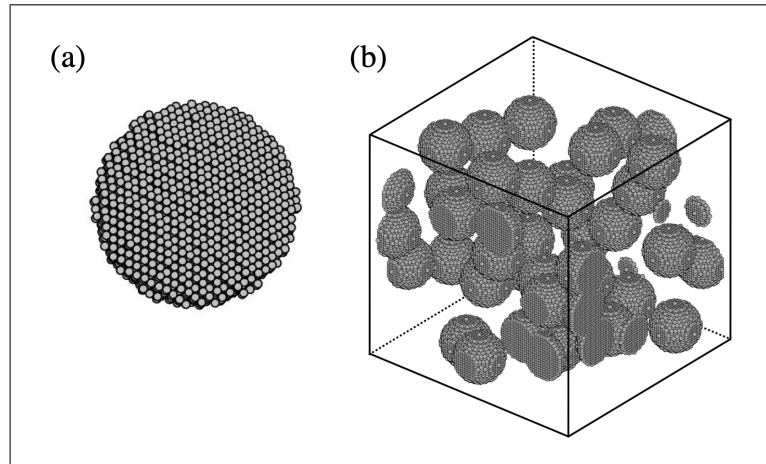


Figure 2.2: 3D visualization depicting (a) a single voxellated NP and (b) a simulated NP composite material geometry, each consisting of two distinct material phases.

The statistical analysis of such large data sets can shed light on the variability and possible yield for such devices which is especially important when considering composites with non-insulating inclusions. Furthermore, simulating a diverse set of randomly-generated composites may also enable the identification of previously unknown optimality conditions when considering the energy storage properties of capacitive dielectrics.

### 2.1.1 Percolation in Simulated Composites

One avenue for the exploration of potential optimization lies in the demarcation of geometries as percolating or non-percolating. In general, composites are often noted as being percolating at higher volume fractions or non-percolating at lower volume fractions of inclusions. This distinction relates to a specific concentration threshold, known as the percolation threshold. Composites that are considered to be percolating contain a continuous “percolating” path of connected inclusions between the anode and cathode of the device. These composites typically have concentrations of inclusions that are greater than the percolation threshold and exhibit non-ideal properties like excessive losses and low breakdown strength. Conversely, a composite that is considered non-percolating has no continuous path between the anode and cathode, and has a concentration of inclusions that is less than the percolation threshold.

In experimentation, because it is common to observe anomalous dielectric properties at or near the percolation threshold, “near-percolation” composites have become a compelling subject of research [4] [47] [48]. When these distinctions are assigned to real systems, however, they are based purely on the filler concentration and not on the actual geometric arrangement of the filler within the insulating matrix. Because of this, it is possible for a material near the percolation threshold to be non-percolating, nearly percolating, or fully percolating, and so large variations are expected near the percolation threshold. To more comprehensively explore this phenomenon, the material generation component of this simulator scans through each pseudorandom geometry to determine whether it is percolating,

near-percolating, or non-percolating. This allows for additional statistical analysis that is used to indicate whether a composite may benefit from enhanced inclusion separation or not. It also allows for further insight into the optimal range of inclusion concentrations.

For initial validation, the simulator was used to generate over 1200 pseudorandom NP composite geometries, where each of which was noted as either being percolating, near-percolating, or non-percolating. Figure 2.3 illustrates the distribution of these geometries over the range of simulated volume fractions, and shows a percolation threshold at a volume fraction of approximately 30%.

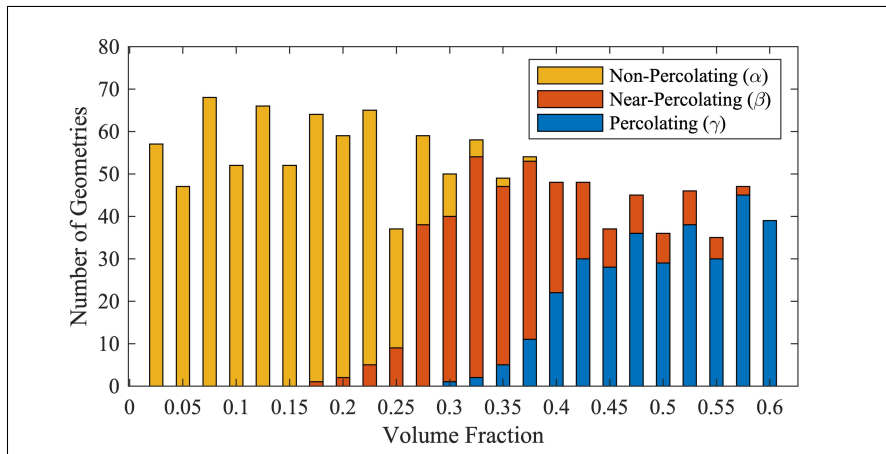


Figure 2.3: Histogram representing the distribution of percolating configurations  $\alpha$ ,  $\beta$ , and  $\gamma$  with respect to volume fraction.

## 2.2 Quasi-Electrostatic Analysis of Simulated Composites

After constructing the NP composite 3-D geometry of voxels, the second stage of this simulation platform uses a control volume technique to solve the 3-D Laplace equation [49][50]. Dirichlet boundary conditions are applied to the top and bottom of the simulated window which correspond to the electrodes of a parallel plate capacitor with an applied potential difference of  $V_{sim}$ . A discrete set of matrix equations are constructed using a finite difference method applied to the Laplace equation such that the continuous Laplace equation for a heterogeneous material is given by Equation 2.1, where  $\varepsilon(x, y, z)$  is the

permittivity as a function of position in the heterogeneous composite.

$$\nabla \cdot \nabla \varepsilon(x, y, z) V(x, y, z) = 0 \quad (2.1)$$

As seen in Appendix A1, successive application of the Euler approximations and second-order trapezoidal quadrature in a rectangular volume with dimension  $\Delta x$  by  $\Delta y$  by  $\Delta z$ , yields a set of discrete equations that use seven nearest-neighbor voltages for each point in the 3-D rectangular mesh geometry. Equation 2.2 is a representative equation that is centered around the point  $(i, j, k)$  in the 3-D mesh.

$$\begin{aligned} V_{ijk} & \left( - \left( \frac{\Delta z \Delta y}{4 \Delta x} + \frac{\Delta z \Delta x}{4 \Delta y} + \frac{\Delta y \Delta x}{4 \Delta z} \right) \times \right. \\ & \left. \left( \varepsilon_{r[000]} + \varepsilon_{r[010]} + \varepsilon_{r[001]} + \varepsilon_{r[011]} + \varepsilon_{r[100]} + \varepsilon_{r[110]} + \varepsilon_{r[101]} + \varepsilon_{r[111]} \right) \right) + \\ & V_{i+1jk} \left( \frac{\Delta z \Delta y}{4 \Delta x} \right) \left( \varepsilon_{r[100]} + \varepsilon_{r[101]} + \varepsilon_{r[110]} + \varepsilon_{r[111]} \right) + \\ & V_{i-1jk} \left( \frac{\Delta z \Delta y}{4 \Delta x} \right) \left( \varepsilon_{r[000]} + \varepsilon_{r[010]} + \varepsilon_{r[001]} + \varepsilon_{r[011]} \right) + \\ & V_{ij+1k} \left( \frac{\Delta z \Delta x}{4 \Delta y} \right) \left( \varepsilon_{r[010]} + \varepsilon_{r[110]} + \varepsilon_{r[011]} + \varepsilon_{r[111]} \right) + \\ & V_{ij-1k} \left( \frac{\Delta z \Delta x}{4 \Delta y} \right) \left( \varepsilon_{r[000]} + \varepsilon_{r[100]} + \varepsilon_{r[001]} + \varepsilon_{r[101]} \right) + \\ & V_{ijk+1} \left( \frac{\Delta y \Delta x}{4 \Delta z} \right) \left( \varepsilon_{r[001]} + \varepsilon_{r[011]} + \varepsilon_{r[101]} + \varepsilon_{r[111]} \right) + \\ & V_{ijk-1} \left( \frac{\Delta y \Delta x}{4 \Delta z} \right) \left( \varepsilon_{r[000]} + \varepsilon_{r[010]} + \varepsilon_{r[100]} + \varepsilon_{r[110]} \right) = 0 \end{aligned} \quad (2.2)$$

These sets of equations are arranged into a single matrix equation given by Equation 2.3, where  $\mathbf{A}$  is the transformation matrix that contains the coefficients from Equation 2.2. The column vector  $\hat{v}$  contains the voltage values at each discrete point in the grid. The column vector  $\hat{b}$  typically contains non-zero values only for the Dirichlet boundary conditions.

$$\mathbf{A}\hat{v} = b \quad \Rightarrow \quad \hat{v} = \mathbf{A}^{-1}b \quad (2.3)$$

Solving Equation 2.3 results in an approximation of the electrostatic scalar potential field ( $\hat{v}$ ) within the simulated composite. This scalar potential field,  $\hat{v}$ , is converted back to a 3-D scalar function representing the potential at all points within the simulated space ( $\mathbf{V}(i, j, k)$ ). This is then used to compute the 3-D electric field by taking the negative gradient of the electrostatic potential throughout the entire simulated window as given by Equation 2.4.

$$\mathbf{E}(i, j, k) = -\nabla \mathbf{V}(i, j, k) \quad (2.4)$$

The magnitude of this electric field ( $|\mathbf{E}|$ ) at each voxel is subsequently used to compute the effective composite permittivity ( $\epsilon_{eff}$ ), effective composite breakdown field strength ( $E_{BD}$ ), and maximum energy density ( $u_{max}$ ). These calculations are detailed in later sections of this chapter, and additional modifications to the breakdown model are detailed in Chapter 3.

Figure 2.4 depicts a cross-section of the electric fields within a single simulated NP geometry consisting of high-k NPs immersed in a low-k dielectric host matrix. This cross-section illustrates not only the distribution of electric fields within the simulated volume, but also the periodicity of the internal NP arrangement and of the internal electric fields. Using the elements of  $\vec{\mathbf{E}}(x, y, z)$  in conjunction with the dielectric properties at each respective position in the simulated volume, it is then possible to compute a range of effective dielectric properties that best describe how the simulated composite is likely to perform as energy storage media.

### 2.2.1 Calculation of Dielectric Permittivity

One of the major dielectric parameters that contributes to the energy density of materials is the effective permittivity ( $\epsilon_{eff}$ ). To calculate this quantity for a given material geometry, the discrete approximation of its internal electric fields is converted to a scalar electric field

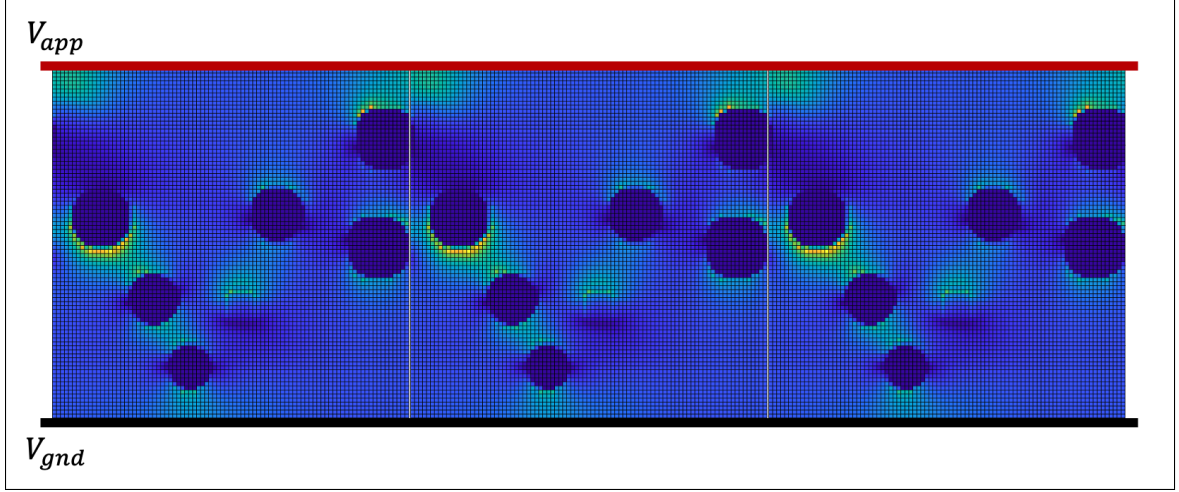


Figure 2.4: Cross-section of a simulated NP composite material geometry consisting of high-k NPs immersed in a low-k insulating dielectric host. The arrangement of NPs and the resultant electric fields both exhibit periodicity about the horizontal boundaries as intended.

representing the magnitude of each electric field vector ( $|\vec{\mathbf{E}}|_{ijk}$ ) by Equation 2.5.

$$|\vec{\mathbf{E}}|_{ijk} = \sqrt{|\mathbf{E}_{x_{ijk}}|^2 + |\mathbf{E}_{y_{ijk}}|^2 + |\mathbf{E}_{z_{ijk}}|^2} \quad (2.5)$$

This quantity is used to determine the total energy ( $E_{total}$ ), and the relationship given in Equation 2.7 is rearranged to solve for the effective permittivity of the simulated volume as given by Equation 2.8. Note that Equation 2.7 and Equation 2.8 rely on the assumption that the simulated device can be accurately described as an ideal parallel plate capacitor, which is granted by the previously discussed periodic boundary conditions in  $\hat{x}$  and  $\hat{y}$ .

$$E_{total} = \sum_{i=1}^{I_{max}} \sum_{j=1}^{J_{max}} \sum_{k=1}^{K_{max}} \left[ \frac{1}{2} \varepsilon_0 \varepsilon_{ijk} |\vec{\mathbf{E}}|_{ijk}^2 \Delta x \Delta y \Delta z \right] \quad (2.6)$$

$$C = \frac{2E_{total}}{V_{sim}^2} = \varepsilon_{eff} \frac{\varepsilon_0 A}{d} \quad (2.7)$$

$$\varepsilon_{eff} = \frac{2E_{total}(\Delta z K_{max})}{V_{sim}^2 \varepsilon_0 (\Delta x I_{max})(\Delta y J_{max})} \quad (2.8)$$

## 2.3 Verification & Validation

Initial validation of this approach has shown a linear error convergence rate of  $O(\Delta)$  when compared to the analytical solution associated with pure materials. This is clearly shown in Figure 2.5(a) a 90% / 10% bi-phase laminate structure, and in Figure 2.5(b) for a single NP centered in the simulated window with a volume fraction of 2%. The analytical solutions for the laminate case assumes an ideal parallel plate capacitor around a 2-phase dielectric slab as given by Equation 2.9.

$$\varepsilon_{eff} = \frac{\varepsilon_1 \varepsilon_2 d_s}{\varepsilon_1 d_2 + \varepsilon_2 d_1} \quad (2.9)$$

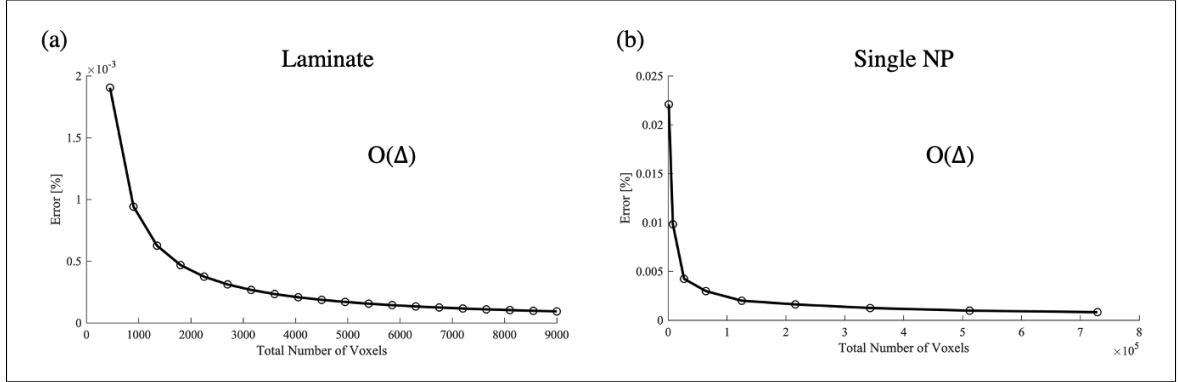


Figure 2.5: Error convergence for QESIM’s 7-point Laplace approximation, evaluating the error associated with effective permittivity ( $\varepsilon_{eff}$ ) in simulated (a) laminate-structured composites and (b) composites with spherical inclusions.

Similarly, the exact solution used for the effective permittivity ( $\varepsilon_{eff}$ ) of the spherical case is given by the analytical Bruggemann equation for mixing of 3-D composites as given by Equation 2.10, where  $f$  is the volume fraction of inclusions,  $\varepsilon_1$  and  $\varepsilon_2$  are the relative permittivities of the inclusion and host, respectively,  $d_1$  and  $d_2$  represent the thickness of constituent layers, and  $d_s$  represents the total thickness of the laminate structure.

$$0 = (f) \frac{\varepsilon_1 - \varepsilon_{eff}}{\varepsilon_1 + 2\varepsilon_{eff}} + (1 - f) \frac{\varepsilon_2 - \varepsilon_{eff}}{\varepsilon_2 + 2\varepsilon_{eff}} \quad (2.10)$$

Efforts to achieve an error convergence rate of  $O(\Delta^2)$  are ongoing, but it is worth noting that additional complexity will inevitably lead to a marked increase computation time and resources. While subsequent versions of this simulator aim to implement higher order solutions, this simulator has already achieved sufficiently accurate results with electric field error under 1% for geometries of  $N_I > 300000$  voxels when simulating pure materials and two-phase layered composites. In addition the approximation of dielectric permittivity has been validated against real-world measured data obtained from [16]. The results obtained from simulating composites analogous to those studied in [16] are pictured in Figure 2.6. When compared to empirical data in this figure, it is clear that this simulator outperforms the widely-used, analytical Bruggeman model in the prediction of effective composite permittivity.

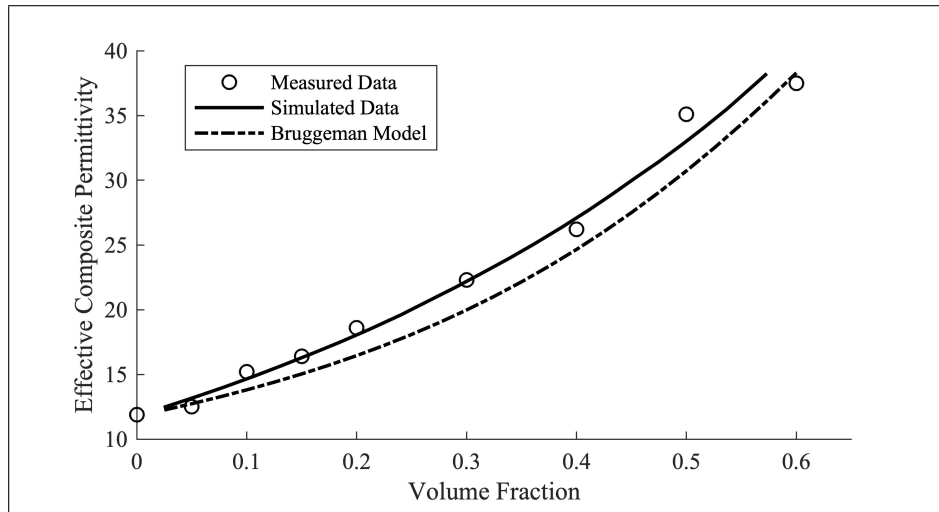


Figure 2.6: Comparison of simulated effective composite permittivity data for a simulated grid size of  $65 \times 65 \times 65$  voxels with permittivity data reported in [16] and approximations obtained using the analytical Bruggeman model.

## 2.4 Summary & Conclusion

In this chapter, a simulator (QESIM) has been designed and implemented to generate pseudorandom NP composite geometries and, subsequently, approximate the internal electric fields that arise in the presence of an applied voltage. The internal electric fields within

each simulated composite have been used in the calculation of the effective composite permittivity for a large number of unique microstructures. The convergence of this effective permittivity approximation has been verified against analytical solutions for both laminate structured composites and for NP composites as shown in Figure 2.5, and exhibits a linear convergence rate of  $O(\Delta)$ . The data obtained from simulation has subsequently been used to validate the efficacy of QESIM as illustrated in Figure 2.6. Based on this, it has been concluded that the simulator developed in this chapter provides sufficient accuracy for the approximation of internal electric fields within real polymer-ceramic NP composite materials.

## CHAPTER 3

### MODELING OF DIELECTRIC BREAKDOWN IN SIMULATED NANOPARTICLE COMPOSITE MATERIALS

With the goal of simulating energy storage properties of both existing and hypothetical materials, several parameters are required. Based on Maxwell's equations, the theoretical maximum energy density stored in an electric field within a pure material with relative permittivity  $\varepsilon_r$  is given by Equation 3.1

$$u_{max} = \frac{1}{2}\varepsilon_0\varepsilon_r E_{bd}^2 \quad (3.1)$$

where  $E_{bd}$  is the breakdown field strength of the material (i.e. the electric field beyond which a the material allows conduction) and  $\varepsilon_r$  is the relative permittivity of the material therein. Because theoretical energy density in Equation 3.1 is related to the square of breakdown strength, engineering of the next generation of energy storage media calls for a more comprehensive understanding of how internal electric fields can act on materials to cause excessive leakage and breakdown events. To this end, the computational models developed in this work discretizes real-world electrostatic phenomena in an effort to better understand critical phenomena like dielectric breakdown.

In the previous chapter, the calculation of effective relative permittivity ( $\varepsilon_{eff}$ ) is outlined and validated against measured data from [16]. Therefore, to accurately quantify the theoretical limits of energy density associated with capacitive dielectric energy storage devices, it is necessary to approximate  $E_{bd}$  for simulated composite materials. Furthermore, while many publications focus on the dielectric permittivity of composites, the squared relationship between energy density and breakdown strength as in Equation 3.1 necessitates a closer look into the internal electric fields and fundamental mechanisms that lead to break-

down. In this chapter, several computational models are explored in this work which aim to predict the effective composite breakdown field strength of a wide range of NP composites.

### 3.1 Understanding Dielectric Breakdown

In experimentation, dielectric breakdown strength is measured by ramping up the applied voltage until a short circuit is detected. In order for a short circuit to form through an insulator, a conductive path for charge carriers must be formed. Therefore, the simulated breakdown path consists of a series of adjacent conductive voxels which form a complete path in 3-dimensions between the anode and cathode boundaries of the simulated window. This concept is elucidated in Figure 3.1, where a cross-section of the electric field is shown in (a) and the resulting breakdown path is highlighted in (b). It should be noted that this model is similar to electrical treeing breakdown models employed in [45] and [43]; however, the model developed in this work utilizes only the magnitude of the electrostatic field instead of a time-dependent scalar voltage field. Future work intends to compare the efficacy of both models to determine which is favorable on the grounds of computation time and accuracy. However, initial simulations show that the model in this work provides comparable accuracy with significantly fewer computations.

In experimentation, dielectric breakdown is obtained by applying incremental voltage to a sample and measuring the current until it appears to have significant conduction (i.e. when the sample shows a linear V-I relationship). This voltage is then recorded as the ‘breakdown voltage’  $V_{bd}$  of the device and  $E_{bd}$  is calculated by dividing  $V_{bd}$  by the sample thickness ( $t_s$ ). Because of relatively large variations in the measured breakdown voltages for seemingly identical materials, dielectric breakdown is considered to be a stochastic process, but physically, dielectric breakdown is a deterministic process driven by energy minimization. The apparent stochasticity that has been observed in experimentation arises from the inherent stochasticity of the internal structure of materials, which is determined by fabrication processes and various environmental factors. Even in pure materials the pres-

ence of defects or impurities in pure materials will have an impact on breakdown strength. The core assumption behind this chapter states that with a sufficiently detailed description of the internal material structure of a composite, it is possible to approximate the breakdown strength of that composite within a reasonable degree of accuracy. This assumption will be tested through comparisons to real experiments from published data.

### 3.2 Statistical Models for Dielectric Breakdown

The first two breakdown models explored in this chapter (the  $(\mu)$ -field model and the  $(\mu\sigma)$ -field model) are closely related in that they both utilize statistical descriptions of the internal electric field to determine the breakdown voltage of composites. These two models are based on the breakdown models employed in [39] and [16], and are intended to provide a baseline accuracy in approximating the breakdown strength of composites while using minimal computation time and resources. Put simply, the first statistical model posits that breakdown occurs at ( $V_{bd}$ ) when the volumetric average of the electric field within each phase exceeds the breakdown strength of that particular phase; the second posits that breakdown occurs when the average plus the standard deviation of the electric field within each phase exceeds the breakdown strength of that phase.

For each of these models, the first phase to break down dictates the breakdown strength of the entire device, as described in Equation 3.2. The first statistical model is used as a baseline for comparison to real data and other models presented in this section. The conditions for breakdown in the first model is obtained by the expression given in Equation 3.3, which states that when the average electric field within phase  $i$  exceeds the known breakdown strength of that material a breakdown event is expected. Equation 3.4 and Equation 3.5 are extensions of this condition which show how the simulated voltage is scaled to the breakdown voltage by the relationship between the average internal electric fields  $\langle |E|_{(i)} \rangle$  and the breakdown field strength  $E_{bd_{(i)}}$  of each  $i^{th}$  phase.

$$V_{bd} = \min \left( V_{bd_{(1)}}, V_{bd_{(2)}}, \dots, V_{bd_{(N)}} \right) \quad (3.2)$$

$$E_{bd(i)} \leq \langle |\vec{E}|_{(i)} \rangle \Big|_{V_{bd}} \quad (3.3)$$

$$E_{bd(i)} = \frac{V_{bd(i)}}{V_{sim}} \langle |\vec{E}|_{(i)} \rangle \Big|_{V_{sim}=1v} \quad (3.4)$$

$$V_{bd(i)} = V_{sim} \frac{E_{bd(i)}}{\langle |\vec{E}|_{(i)} \rangle \Big|_{V_{sim}}} \quad (3.5)$$

Because of potentially breakdown-inducing fluctuations in the electric fields due to the NP inclusions, it is expected that this average model will produce an optimistic result that overestimates the breakdown voltage of simulated composites as seen in Figure 3.2. In realistic heterogeneous materials, highly variant electric fields can lead to breakdown events at much lower voltages. The magnitude of such fluctuations can be quantified as the standard deviation of the electric field. Therefore, the second statistical model operates under the assumption that a breakdown event will occur when the sum of the average and standard deviation of the electric field within each phase of a composite exceeds the breakdown field strength of that phase. This can be mathematically described by setting the breakdown condition for each phase to  $\langle |\vec{E}|_{(i)} \rangle$  plus the standard deviation of electric field magnitudes within each phase ( $\sigma_{E(i)}$ ) as given by Equation 3.6.

$$V_{bd(i)} = V_{sim} \frac{E_{bd(i)}}{\left( \langle |\vec{E}|_{(i)} \rangle + \sigma_{E(i)} \right) \Big|_{V_{sim}}} \quad (3.6)$$

As one may expect, this modified statistical model provides a more accurate approximation of breakdown strength of materials, but one thing this study aims to provide is more comprehensive information on the variability of breakdown strength of composites.

This second statistical model fails to capture the variability associated with breakdown strength in randomly structured composites that was observed experimentally in [16], as can be plainly seen in Figure 3.2(a). As such, the next section details the development, implementation, and validation of a more accurate physics-based breakdown model for the approximation of both the mean and variance of breakdown strength in randomly structured composites.

### 3.3 Physical Model for Dielectric Breakdown

In an effort to better understand the physical process of breakdown in composites, a third breakdown model is developed which uses the internal electric fields in a given microstructure to simulate the formation of conductive breakdown paths in a specific composite material subject to an applied voltage that is increased incrementally. This new model operates by examining each voxel in the simulated window to determine if the electric field within that voxel constitutes a local breakdown event. As the voltage is incrementally increased, more and more voxels have sufficient electric field strength to trigger a percolating breakdown event. When a voxel experiences breakdown, it is considered to be conductive, and when a single continuous path of voxels forms from anode to cathode through the insulating media, the simulated device has experienced a breakdown event. Once a path is detected, the lowest voltage at which that conductive path exists is stored as the breakdown voltage ( $V_{bd}$ ) for that particular simulated composite. In Figure 3.1 (a), the electric field magnitudes within a cross-section of a simulated NP composite can be seen, and in Figure 3.1 (b) the region highlighted in yellow represents the breakdown path through the simulated volume. It should be noted that the breakdown path propagates in 3-dimensions, and so only a segment of the continuous conductive path is pictured in this single cross-section.

Algorithmically, this model mimics the physical process of breakdown by the propagation of electrical trees, using only a fraction of the computational resources. This is made possible by the use of electric field magnitudes rather than the entire 3-D time-dependent

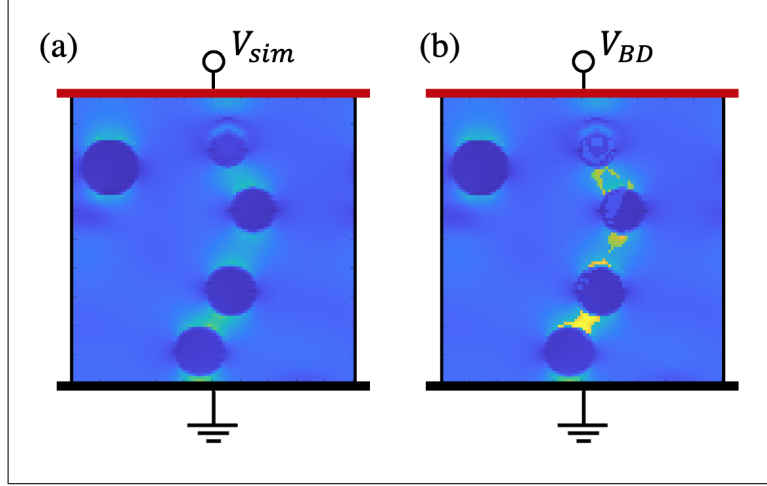


Figure 3.1: Cross-section of (a) the simulated internal electric field of a NP composite and (b) the breakdown path through the electric field at breakdown voltage ( $V_{BD}$ ).

vector quantity that is commonly used as in [44], [45], and [43]. This deviation from the traditional electrical treeing approach was chosen to mimic the conditions leading up to breakdown events within realistic solid state materials while reducing the computation time necessary to estimate the breakdown path within a single simulated composite geometry.

### 3.4 Comparison of Implemented Dielectric Breakdown Models

In this section, these three models are compared with measured data as reported in [16] to determine which one most accurately captures the stochastic breakdown behavior observed in real NP composites. To this end, the set of simulated composites ( $N_\Omega > 1200$ ) that was used in the previous chapter has been analyzed further to approximate the breakdown strength of each simulated geometry using each of the breakdown models discussed in this chapter. In Figure 3.2(a), the statistical models (red, blue) are juxtaposed against measured breakdown field strength of real NP composites as reported in [16], and in Figure 3.2(b), the physics-based breakdown path model (yellow) is juxtaposed against the same measured data.

In Figure 3.2 (a), it is clear that the average model provides a highly optimistic estimate for breakdown strength, while the additional consideration of standard deviation largely

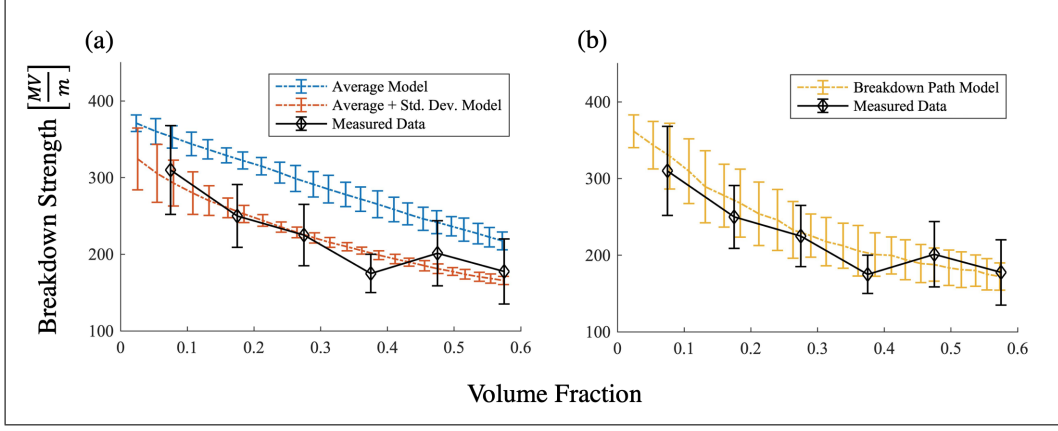


Figure 3.2: Comparison of breakdown strength data reported in [16] to simulated composite breakdown field strength data obtained using (a) average electric field models, and (b) breakdown path model.

corrects this optimism. When compared with the data reported in [16], which has an average variance of  $174.7[\frac{MV}{m}]^2$ , the RMSE value for the first statistical model (shown in blue in Figure 3.2) is  $62.09[\frac{MV}{m}]$ . More significantly, the average variance,  $\langle \sigma^2 \rangle$ , for all volume fractions of data obtained using this model is  $23.23[\frac{MV}{m}]^2$ , which is nearly an order of magnitude lower than that of measured data. Likewise, the second statistical model (shown in red in Figure 3.2) has a RMSE value of  $20.33[\frac{MV}{m}]$  with an average variance of  $27.76[\frac{MV}{m}]^2$ . Again, this is nearly an order of magnitude lower than the average variance of the measured data reported in [16]. Despite the apparent close correlation with measured data (when considering the average breakdown strength of all simulated composites), the variability of estimated breakdown strength values obtained using each of these models fails to effectively replicate that which has been observed in [16]. While these models provide a way to quickly approximate the breakdown strength of a simulated composite, it does not accurately model the high variability in breakdown strength that has been observed in real NP composites.

In Figure 3.2 (b), the new physics-based breakdown path model provides the most effective approximation of both the mean and variance of breakdown strength as observed in real-world NP composite materials. The RMSE of the data obtained using the break-

down path detection model compared to the measured data reported in [16] is  $18.27[\frac{MV}{m}]$ . This model provides the lowest RMSE for the estimation of the average, and it is clear that the breakdown path model also provides a significantly closer correlation to the average variance observed in the measured data. In the set of over 1200 unique, pseudo-random geometries, the values of breakdown strength computed using this model have an average variance of  $114.3[\frac{MV}{m}]^2$ , which is almost an order of magnitude more accurate than the mean and standard deviation models when compared to the measured data. In light of this comparison, all subsequent chapters utilize the new physics-based model discussed in this chapter to approximate the breakdown strength of simulated composites.

### 3.5 Summary & Conclusion

To quantify the breakdown strength of simulated NP composite materials, three models have been incorporated into QESIM and have been compared to real-world measured data. When compared to data reported in [16], the two statistical models provide a reasonable estimate for the mean expected breakdown strength in simulated composites. Unlike the two statistical models, however, the breakdown path model is based on the physical process of dielectric breakdown, and has proven to be the most accurate of the three models studied in this chapter. The breakdown path model not only provides an accurate estimate of the mean breakdown strength when compared to the measured data, but it also accurately predicts the average variance with much greater accuracy than other two models. As such, it is concluded that the new breakdown model provides the most accurate estimate of breakdown strength in the simulated heterogeneous composites, and so it will be used in all subsequent chapters to quantify the expected breakdown strength of simulated composites.

While several works employ techniques for the simulation of internal electric fields that are similar to those used in this simulator like in [51], many tend to utilize existing tools for the generation and simulation of finite element grids. This work is further differentiated from those that utilize finite difference grids with the employment of a novel algorithm

for the physics-based estimation of breakdown field strength in composites. It should be noted that while some works like [45] and [43] use electrical treeing models, which can be highly computationally intensive, others like [51] use statistical models that tend to be less accurate for complex internal geometries.

## CHAPTER 4

### ENERGY DENSITY LIMITS & VARIATIONS IN 2-PHASE NANOPARTICLE COMPOSITES

The simulation experiments carried out in this chapter utilize the simulation framework discussed in previous chapters in conjunction with the validated models for the approximation of internal electric fields ( $\mathbf{E}$ ), effective permittivity ( $\varepsilon_{eff}$ ), and breakdown field strength ( $E_{bd}$ ). With this, it is possible to calculate the maximum theoretical energy density ( $u_{max}$ ) as in Equation 4.1.

$$u_{max} = \frac{1}{2}\varepsilon_{eff}\varepsilon_0(E_{bd})^2 \quad (4.1)$$

This equation is then applied to the data obtained from simulations of three unique hypothetical composite materials to highlight possibly optimal configurations between host and inclusion materials that lead to optimal energy densities in NP composite materials. In general, this body of work aims to examine the potential of certain NP composite materials as capacitive dielectric energy storage media. Leveraging the high breakdown strength of dielectric polymers as host material, in conjunction with the high permittivity of various dielectric inclusion materials, it is hypothesized that certain material combinations may lead to significant improvements in theoretical maximum energy density. The remainder of this chapter is dedicated to a computational exploration of these results in the context of composite materials.

#### 4.1 Quantifying Energy Density Limits

In a perfect world, the successful fabrication of composites that increase both  $\varepsilon_{eff}$  and  $E_{bd}$  would lead to a significant improvement in energy density. However, one major issue with such reasoning centers around a proposed fundamental inverse relationship between  $\varepsilon_{eff}$

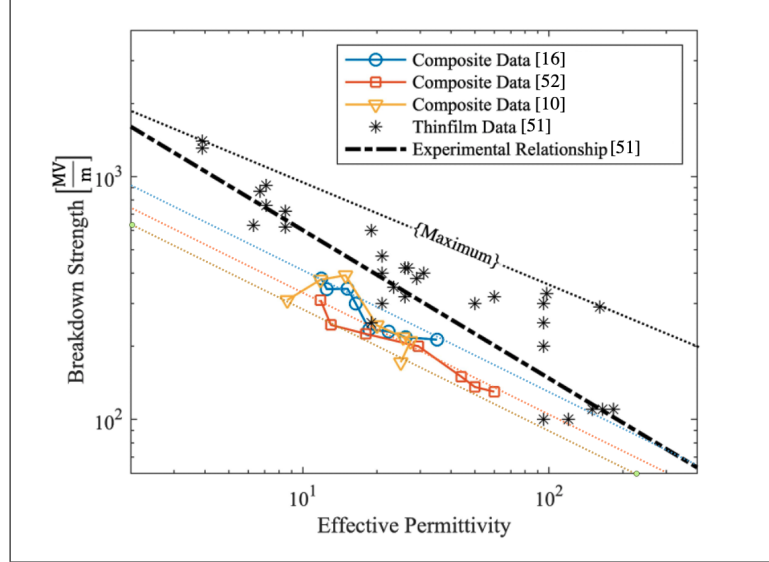


Figure 4.1: Inverse relationship between permittivity and breakdown field strength from [52] depicted as contours of constant energy density juxtaposed against measured data from [16], [53], and [10]. A black dotted line marks a supposed boundary imposed by the two materials with highest reported energy density among pure materials and blue, yellow, and red dotted lines represent constant energy densities equal to that of the pure host materials in [16],[53], and [10], respectively.

and  $E_{bd}$ , which has been explored and quantified in [52]. The researchers state that this relationship holds true for a broad range of insulating dielectric materials, and so it is considered to be a fundamental limiting factor for energy density in capacitive dielectrics. As such, this work aims to explore the limits and variations of energy density in realistic composite materials comprised of multiple phases, each with dielectric properties that adhere to this fundamental relationship. To this end, several real-world materials are chosen from [52] for further exploration as filler in hypothetical polymer/ceramic composites.

#### 4.1.1 Relationship Between Permittivity and Dielectric Breakdown

To explore this proposed fundamental relationship, the pure material data reported in [52] has been juxtaposed against composite material data reported in [16], [10], and [53] in Figure 4.1, with  $\varepsilon_{eff}$  and  $E_{bd}$  on the  $\hat{x}$  and  $\hat{y}$  axes respectively. In this plot the energy density is highest for points nearest to the upper right corner. Thus, it can be inferred that composite

materials may generally exhibit lower energy densities than pure materials, which is largely consistent with the current literature. More importantly, some composites at optimal volume fractions do exhibit significantly improved energy density when compared to that of the pure host material. This is illustrated by the triangular yellow points above the yellow dotted line which represent composites with energy densities greater than that of the pure host material in [10].

To further support this proposed relationship, Equation 4.3 defines the fundamental relationship between  $\varepsilon_{eff}$  and  $E_{bd}$  that is needed for a constant energy density  $u_{max}$ . The relationship derived in [52] suggests that in the set of materials studied, the low-k materials tend to exhibit higher energy densities than their high-k counterparts. This is seen by comparing Equation 4.2 with Equation 4.3 to obtain Equation 4.4. Interestingly, this deviates from the common notion that high-k inclusions lead to higher energy density composites [3]. This relationship was observed and empirically fit to Equation 4.2, which closely resembles a form obtained by assuming that energy density is constant among pure ceramics as given by Equation 4.3.

$$E_{bd} = 22.5 \varepsilon_{eff}^{-0.64} \quad (4.2)$$

$$u_{max} = \frac{1}{2} \varepsilon_{eff} \varepsilon_0 E_{bd}^2 \rightarrow E_{bd} = \left( \sqrt{\frac{2u_{max}}{\varepsilon_0}} \right) \varepsilon_{eff}^{-0.5} \quad (4.3)$$

$$u_{max} = \frac{(11.25)(\varepsilon_0)}{(\varepsilon_{eff})^{0.28}} \quad (4.4)$$

The relationship given by Equation 4.4 further supports the notion that low-k materials may exhibit higher energy densities than high-k materials, indicating a possible opportunity for higher energy densities using low-k materials that are excited with electric fields near their breakdown limits. It is therefore hypothesized that low-permittivity inclusions will lead to greater improvements in theoretical maximum energy density compared to high-k inclusions due to the enhancement of effective permittivity by the host material and the

enhancement of breakdown strength due to the NP inclusions. To test this hypothesis, the three materials are selected from those studied in [52] based on their reported energy density, breakdown strength, and permittivity.

#### 4.1.2 Material Selection

The filler materials selected for further exploration in this chapter are those which exhibit the greatest  $u_{max}$  as calculated from  $\varepsilon_{eff}$  and  $E_{bd}$  data reported in [52]. The set of selected materials was chosen to vary greatly in  $\varepsilon_{eff}$  (and consequently  $E_{bd}$ ) so as to provide a better picture of the energy density limits for a broad range of possible parameter combinations. Based on this observed relationship between the two parameters most critical in the calculation of energy density stored in an electric field, three materials have been selected for additional exploration as possible NP composite filler. The selected inclusion materials have been chosen to include materials with a range of dielectric properties. For example,  $\text{SrTiO}_3$  exhibits high permittivity but low breakdown strength,  $\text{SiO}_2$  exhibits low permittivity but high breakdown, and  $\text{HfO}_2$  exhibits mid-range permittivity and mid-range breakdown strength. Two of these materials can clearly be seen in Figure 4.1 where the dashed line labeled 'maximum' intersects with points from [52] at high and low permittivity values.  $\text{BaTiO}_3$  is also included for comparison to data that was previously used for validation against real-world composites.

Using the same geometric parameters as the materials studied in [16] with alternative constituent materials selected from the set of materials studied in [52], three additional hypothetical material cases were simulated. These cases all consist of a P(VDF-HFP) host matrix with embedded NPs of (1)  $\text{SrTiO}_3$ , (2)  $\text{SiO}_2$ , and (3)  $\text{HfO}_2$ . The P(VDF-HFP) host matrix has a permittivity of 11.8 and a breakdown strength of  $380[\frac{MV}{m}]$  as reported in [16].

Table 4.1: Table of material properties obtained from [52] and [16] used as host or inclusion materials in the simulation of hypothetical high-energy-density NP composites in [50] with the host material in bold for comparison.

Material	$\varepsilon_r$	$E_{bd} \frac{MV}{m}$
<b>P(VDF-HFP)</b>	<b>11.8</b>	<b>380</b>
BaTiO <sub>3</sub>	80	150
SrTiO <sub>3</sub>	161	290
SiO <sub>2</sub>	3.9	1400
HfO <sub>2</sub>	21	470

#### 4.1.3 Simulation of Hypothetical Composites

For each material combination, over 1200 unique geometries were simulated and analyzed. The dielectric properties of the materials simulated in this chapter are listed in Table 4.1. Each simulated geometry represents a cubic volume ( $250\text{nm} \times 250\text{nm} \times 250\text{nm}$ ), and consists of exactly one million individual cubic voxels (or cells). As discussed in previous chapters, the boundary conditions are such that each individual geometry represents a capacitive energy storage device that extends infinitely in  $\hat{x}$  and  $\hat{y}$ , but is terminated by Dirichlet electrodes at the  $\hat{z}$  boundaries. The NPs within each geometry have a diameter of 40nm, and are allowed to overlap slightly (up to 5nm), as is commonly observed in NP composites of this scale. From this, the internal electric fields within each composite geometry are estimated and subsequently used to calculate  $\varepsilon_{eff}$ ,  $E_{bd}$ , and finally  $u_{max}$ . The results of these simulations are detailed in the next section.

## 4.2 Results & Discussion

From this study, four large data sets ( $N_\Omega > 1200$ ) were obtained which give insight into possible optimal material combinations that have been previously underexplored. In Figure 4.3(b),(c), and (d), a large number of outliers are observed, leading to high variations in energy density among samples differing only in NP volume fraction and microstructural geometry. This is due to the differences in breakdown strength among simulated compos-

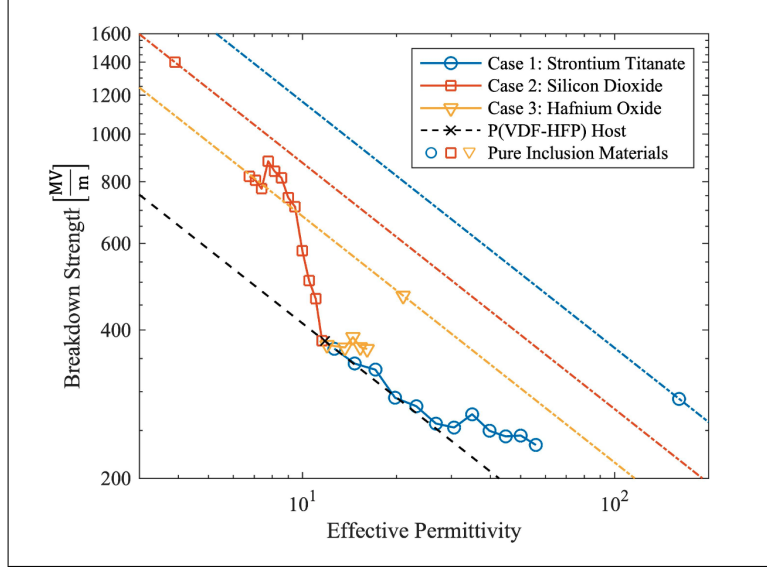


Figure 4.2: Simulated composite material data from four cases of different NP inclusion materials based on thin film measurements reported in [52]. The dashed lines represent contours of constant energy density corresponding to each constituent material.

ites, and indicates possible opportunities for energy density optimization. In particular, a large variation is observed in the  $\text{SiO}_2$  case pictured in Figure 4.3(c). These results further support the thought that low-k inclusions with high dielectric strength could lead to exceptionally high energy density composites. Figure 4.4 shows the maximum energy densities of each percolating configuration within each For practicality, the maximum theoretical energy density is calculated by a modified version of Equation 4.1 which includes a practicality factor of  $\zeta = 0.5$ , as given by Equation 4.5.

$$u_{max} = \frac{1}{2} \varepsilon_{eff} \varepsilon_0 (\zeta E_{bd})^2 \quad (4.5)$$

In Figure 4.2, much like in Figure 4.1, the energy density is highest towards the upper right corner of the plot, where the diagonal blue, red, and yellow lines represent contours of constant energy density. Noting that the theoretical maximum energy density is highest for pure strontium titanate, as per the diagonal blue line, it may seem as though the pure high-k dielectric would provide optimal energy storage properties. This line of thinking, however, neglects the consideration of loss characteristics within such materials. In the case of pure

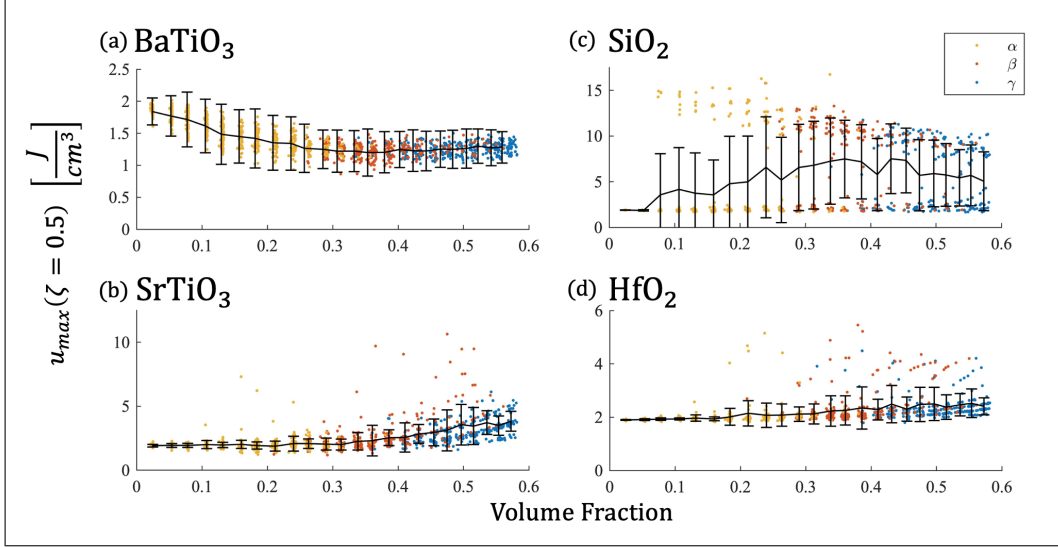


Figure 4.3: Scatterplot with mean and  $3\sigma$  variation overlay depicting the theoretical maximum energy density ( $u_{max}$ ) calculated with practicality factor  $\zeta = 0.5$ . P(VDF-HFP) composites with inclusions of (a)  $\text{BaTiO}_3$ , (b)  $\text{SrTiO}_3$ , (c)  $\text{SiO}_2$ , and (d)  $\text{HfO}_2$  are shown. Each data set consists of over 1200 simulated geometries.

high-k dielectrics losses tend to be excessively high, rendering such materials an imprudent choice for energy storage applications. Thus, it is favorable to employ composites that contain high-k inclusions rather than pure materials so that the losses are mitigated via the separation of high-k domains by the dielectric polymer host. Looking at the results obtained from the hypothetical P(VDF-HFP)-based composites also included in Figure 4.2, it is clear that optimal energy storage characteristics have been achieved by the simulated composites containing  $\text{SiO}_2$  NPs.

In addition to this, it is important to note the glaring difference between high and low energy density geometries (i.e. percolation and non-percolation). As shown in Figure 4.4, it has been found that a more uniform separation between NPs (i.e. non-percolating or near-percolating geometries) tend to exhibit higher energy densities. This is consistent with the widely understood notion that clustering of inclusions leads to higher leakage and losses, as well as a lower breakdown strength [3] [54]. It follows that enhanced separation of inclusions would more effectively distribute the electric fields and, therefore, contribute to higher dielectric strength and improved loss characteristics. As such, this analysis has led to

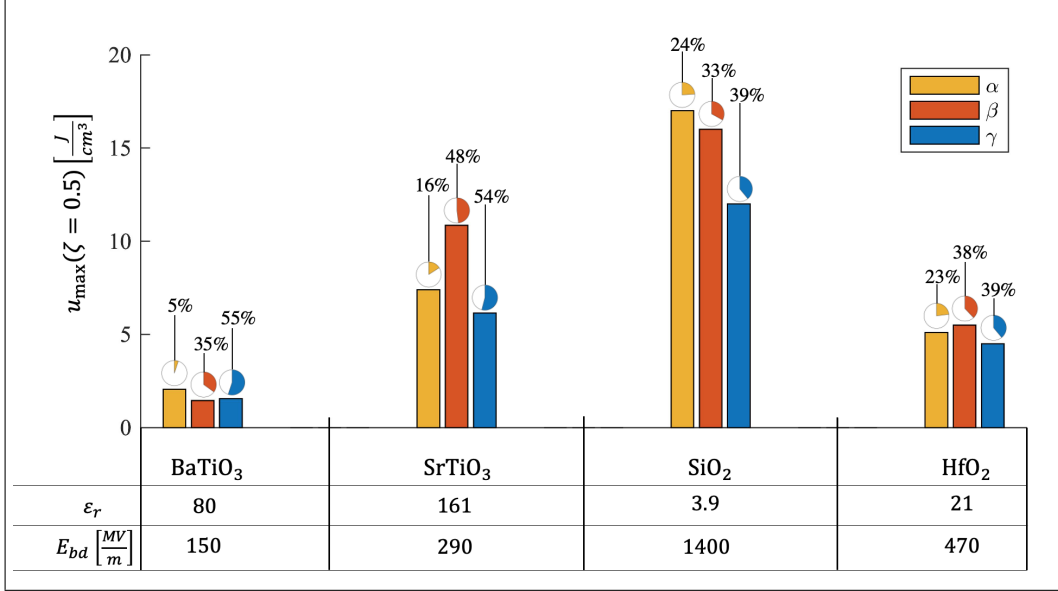


Figure 4.4: Maximum theoretical energy density observed in simulation results for each geometric percolating configuration within each inclusion material data set. Pie charts at the top of each bar show the volume fraction of inclusions at which the maximum energy density value is observed. Listed below the x-axis is a table of the dielectric properties associated with each inclusion material obtained from [52].

the conclusion that utilizing a low-k inclusion material of high dielectric strength immersed in a host material with a high degree of separation between inclusions will produce optimal energy storage characteristics for 2-phase composites. Using the average parametric values for each volume fraction simulated in this chapter, Figure 4.2 and Figure 4.3 were created to give better insight into how these hypothetical composites push the limits of energy density for composite materials.

### 4.3 Summary & Conclusion

To quantify the limits and variations associated with NP composite materials consisting of different constituent phases, QESIM has been employed to simulate four promising hypothetical composite materials. Each of the hypothetical composites are simulated with material parameters obtained from experimental thin film data reported in [52]. Figure 4.3 and Figure 4.4 indicate that the inclusion material with the lowest dielectric permittiv-

ity exhibits the highest maximum theoretical energy density of the simulated hypothetical material combinations. It was found that the  $\text{SiO}_2$  NP filler led to a maximum increase in energy density of nearly an order of magnitude at a volume fraction of 24% when compared to the pure P(VDF-HFP) host. These results illustrate the advantages of low-k dielectric fillers as a means by which to reduce the high electric fields within the host material that often lead to reductions in breakdown strength. While most literature aims to enhance the effective permittivity of composites through the incorporation of high-k inclusions, the optimal filler material for maximum theoretical energy density is actually the low-k material. This is due to the fact that higher electric fields tend to accumulate within low-k regions, and the high breakdown strength of these inclusions ultimately leads to improvements in effective breakdown strength. Therefore, it is concluded that in the context of energy density optimization, the choice of inclusions to enhance the breakdown strength of a composite material is preferable to one that would enhance its effective permittivity.

## CHAPTER 5

### QUASI-ELECTROSTATIC MODEL VALIDATION FOR METAL-INSULATOR NANOPARTICLE COMPOSITES

The primary goal of this chapter is to explore the simulation of a broader range of material combinations. Specifically, composites containing high-conductivity material domains are to be simulated so that their energy storage properties can be quantified. It is worth noting that parameter approximation for heterogeneous material systems containing both conductive and insulating domains is inherently difficult owing to a number of factors. First, experiments in this thesis have shown that metal-insulator-composites (MIC) tend to exhibit a greater variability in permittivity and breakdown strength than composites studied in previous chapters. Second, the large difference in conductivity between inclusion and host materials can lead to error-inducing numerical artifacts. Moreover, MIC are generally excluded from consideration as effective energy storage media due to their tendency to exhibit greater AC losses and lower breakdown strength despite exhibiting enhanced localized charge density due to Maxwell-Wagner interfacial polarization [55]. Of the publications that explore the energy storage properties properties of MIC, very few find them to be advantageous in energy storage applications, as the reductions in breakdown strength generally offset any significant permittivity enhancements [21].

To ensure this simulator adequately handles the approximation of dielectric properties for both insulating and conductive filler material, the model outlined and validated in previous chapters has been modified to utilize complex permittivity for the quasi-electrostatic approximation of complex electric fields within the simulated volume. These modifications boil down to a single expression, as given by Equation 5.1, but later sections will reveal additional considerations that contribute to this particular model's greater overall complexity. Specifically, as noted in [56] and [47], exceptionally high polarizability enhancements have

been observed in composites that include both metallic and insulating phases and have been attributed to a broad range of different mechanisms. Equation 5.1 provides a general form for the definition of both complex permittivity ( $\varepsilon^*(\omega)$ ) and complex relative permittivity ( $\varepsilon_r^*(\omega)$ ). In each case, the frequency dependence of both permittivity and conductivity are explicitly shown. In Equation 5.2, this relationship between complex permittivity, real permittivity, and conductivity is arranged to express the relationship between the effective dielectric properties of materials and the loss characteristics therein. The real permittivity ( $\varepsilon'$ ) and the imaginary permittivity ( $\varepsilon''$ ), as defined in Equation 5.1, can also be used to determine both quality factor ( $Q$ ) and loss tangent ( $\tan \delta$ ) for some applied frequency,  $\omega_0$ .

$$\begin{aligned}\varepsilon^*(\omega) &= \varepsilon'(\omega) - j\varepsilon''(\omega) \\ &= \varepsilon_r(\omega)\varepsilon_0 - j\frac{\sigma(\omega)}{\omega} \\ \varepsilon_r^*(\omega) &= \varepsilon_r(\omega) - j\frac{\sigma(\omega)}{\omega\varepsilon_0}\end{aligned}\tag{5.1}$$

$$\tan(\delta) = \frac{\varepsilon''_{eff}}{\varepsilon'_{eff}} = Q^{-1} = \frac{\sigma_{eff}}{\varepsilon_{eff}\omega_0}\tag{5.2}$$

The relationships expressed in Equation 5.1 and Equation 5.2 are the fundamental basis of computational methods used in this chapter. As discussed in previous chapters, the discretization of the simulated space necessitates specific handling of these equations. To avoid numerical artifacts often associated with complex floating-point arithmetic, the calculation of  $\varepsilon'_{eff}$  and  $\varepsilon''_{eff}$  are performed separately. This is critical in the simulation of MIC as the difference in conductivity between the conducting and insulating phases leads to both underflow and overflow, and when multiplied a loss of precision is effectively unavoidable without drastically increasing computation time [57]. While the calculation of  $\varepsilon'_{eff}$  simply remains identical to that outlined in Equation 2.6 through Equation 2.8, the calculation of  $\varepsilon''_{eff}$  requires several additional considerations. The method described here is based on the

relationship between power dissipated in each voxel ( $P_{ijk}$ ), the internal electric field magnitude, and the conductivity of each phase within the composite. The method described below is supported by Ohm's Law, which states that the volumetric power density in a given volume is related to the product of conductivity and electric field magnitude squared (i.e.  $P = \sigma E^2$ ). This concept is discretized through the simulated space to obtain the total power and subsequently the effective conductivity of the simulated composite.

First, the total power dissipated within the simulated material  $P_{tot}$  is determined by superposition of the power dissipated in every voxel ( $P_{ijk}$ ) within the simulated space, as noted in Equation 5.3 and Equation 5.4.

$$P_{tot} = \sum_{\forall ijk}^{\in \Omega} [P_{ijk}] \quad s.t. \quad P_{ijk} = \sigma_{ijk} |\vec{E}|_{ijk}^2 (\Delta x \Delta y \Delta z) \quad (5.3)$$

$$P_{tot} = \sum_{\forall ijk}^{\in \Omega} \left[ \sigma_{ijk} |\vec{E}|_{ijk}^2 \right] (\Delta x \Delta y \Delta z) \quad (5.4)$$

This total power is then used to determine the effective composite conductivity ( $\sigma_{eff}$ ) as given by Equation 5.5, and  $\varepsilon''_{eff}$  is then calculated using the relationship given by Equation 5.6.

$$\sigma_{eff} = \frac{P_{tot}}{|\vec{E}|_{app}^2 (\Delta x \Delta y \Delta z) (I_{max} J_{max} K_{max})} \quad (5.5)$$

$$\varepsilon''_{eff} = \frac{\sigma_{eff}}{\varepsilon_0 \omega} \quad (5.6)$$

The final expression that defines the discrete approximation of loss tangent is given by Equation 5.7.

$$\tan(\delta) = \frac{\sum_{\forall ijk}^{\in \Omega} \left[ |\vec{E}_{ijk}|^2 (\sigma_{ijk}) \right]}{|\vec{E}_{app}|^2 I_{max} J_{max} K_{max} (\omega \varepsilon_0 \varepsilon_r)} \quad (5.7)$$

Where  $|\vec{E}|_{ijk}^2$  represents the square magnitude of the electric field at voxel  $(i, j, k)$ ,  $|\vec{E}|_{app}^2$  represents the square magnitude of the applied electric field, and  $I_{max}$ ,  $J_{max}$ , and  $K_{max}$

represent the index limits of the simulated window along their respective axes. The full derivation is provided in Appendix A2. As discussed in subsequent sections of this chapter, thorough validation has indicated that the loss characteristics in MIC arise largely from the large electric field buildup within regions of the insulating host material that are adjacent to conductive NP domains. The model discussed here has been validated against data obtained from fixed geometries analyzed using COMSOL Multiphysics® that feature a single NP inclusion or a single nanolaminate layer, each with varying size and conductivity. These simulations are detailed in the next section, and this initial validation is then followed by additional validations which compare data obtained from the simulation of a large set of pseudorandomly-generated NP composite geometries to that of experimental real-world composite materials as reported in several published works.

## 5.1 Model Validation Part 1: COMSOL Multiphysics® Comparisons

To examine the effects of inclusion conductivity on effective composite permittivity, two notable validation experiments were carried out. In the first experiment, three laminate geometries are simulated using QESIM and COMSOL, each containing a single layer of metal of incremental thickness ( $t$ ) that is sandwiched between equal volumes of a lossy insulating host. In the second experiment, three NP geometries are simulated using QESIM and COMSOL, each containing a single metallic NP with incremental radius ( $r$ ) that is positioned directly in the center of the simulated volume, and surrounded by a lossy insulating host. The results of these simulations (as well as the geometries simulated) are illustrated in Figure 5.1 and Figure 5.2 respectively.

Note that in each of these validation experiments shown in Figure 5.1 and Figure 5.2 the error does not exceed 5%. This provides validation for the accuracy of QESIM when compared to traditional vetted simulation tools. Examining these figures more closely, it becomes apparent that several other notable features warrant further discussion. Most importantly, the transition region just below  $\sigma_i = 10^{-4}$  indicates that QESIM accurately

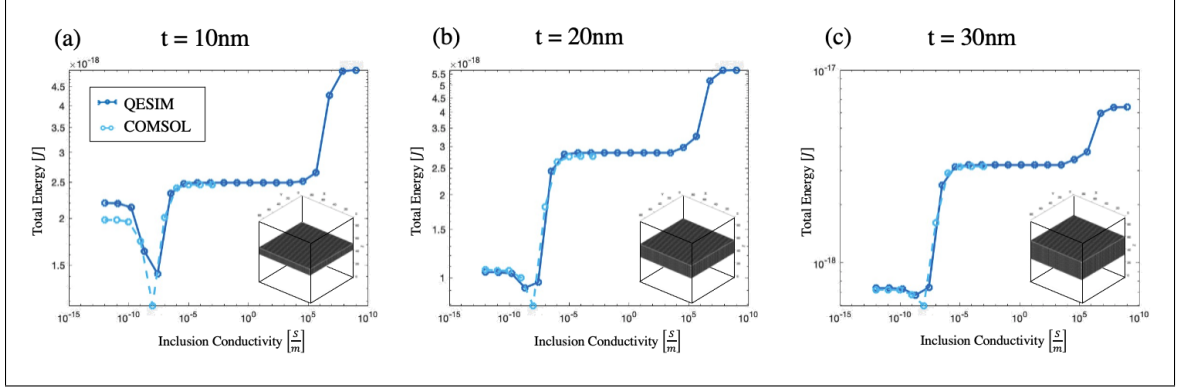


Figure 5.1: Validation of QESIM for conductive NPs in a lossy insulating host against analogous COMSOL model for nanolaminates with a single metallic layer of thickness equal to (a) 10 nm, (b) 20 nm, and (c) 30 nm.

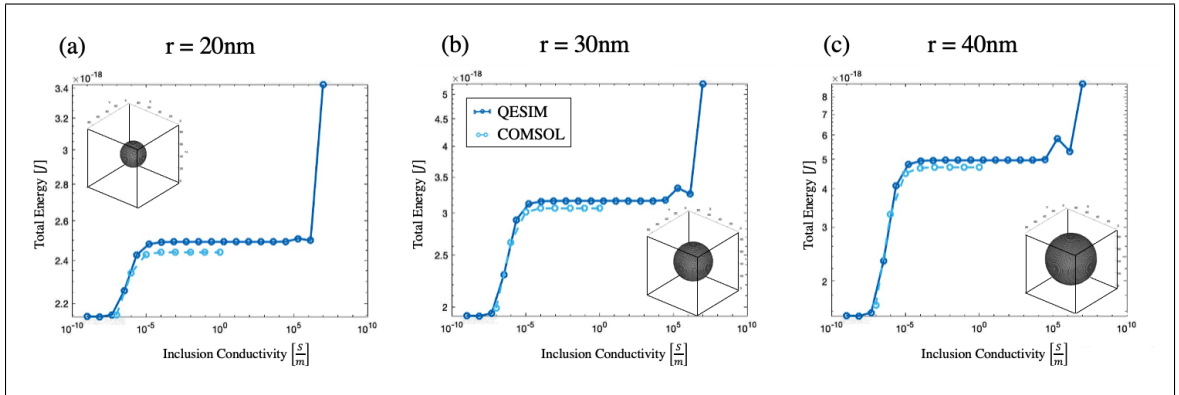


Figure 5.2: Validation of QESIM for conductive NPs in a lossy insulating host against analogous COMSOL model for NPs with radius equal to (a) 20 nm, (b) 30 nm, and (c) 40 nm.

simulates Maxwell-Wagner surface-polarization phenomena. It is also worth noting that for inclusion conductivity values between  $10^{-4} \text{ S/m}$  and  $10^5 \text{ S/m}$  the total energy of each composite remains approximately constant. This observation is consistent with findings in [58], which concludes that there exists an inherent saturation point in composite materials, above which the properties of the composite cannot be enhanced further by changing the properties of the filler. Although [58] focuses on the elastic modulus and thermal conductivity of the composites studied therein, Wiedemann–Franz’ law and the inherent relationship between elastic modulus and dielectric permittivity imply an extension of these findings into the realm of dielectric composites as well. Essentially, it can be stated that the effec-

tive permittivity will remain constant for filler conductivity values above a certain value at constant volume fraction. This also implies a more significant microstructural-dependence in the effective permittivity of MIC than was previously assumed.

In addition, the spike in total energy above an inclusion conductivity of  $10^5 S/m$  should be noted, as it represents a fundamental numerical limitation of the simulator employed in this work. After thorough exploration, it has been determined that this spike represents a specific type of numerical artifact which occurs when two 64-bit, double-precision, floating-point numbers that differ by more than 12 orders of magnitude are multiplied. This multiplication produces a vast overestimation due to the rounding-up that must occur for the smaller number so as to avoid a zero-result. This can be mitigated by allocating extra memory for certain floating-point operations, but this would more than double the computational time required for the simulation of each geometry. The more efficient solution in this instance involves reducing the conductivity of inclusions by several orders of magnitude to take advantage of the observed conductivity saturation effect that is noted between  $10^{-4} S/m$  and  $10^5 S/m$  in Figure 5.1 and Figure 5.2. Because the total energy within the simulated composite does not change with inclusion conductivity in the specified range, it follows that effective composite permittivity will remain invariant in that range as well. To support this assumption, the simulator has been successfully validated against measured data for both loss tangent and effective composite permittivity reported in two experimental works [19] and [20].

## 5.2 Model Validation Part 2: Experimental Measurements

Following the validation detailed in the previous section, the simulator was utilized to simulate real-world NP composite materials analogous to those described in experimental studies like [20] and [19]. In [20], copper NPs were introduced into a polyurethane host, and the dielectric properties of mixtures containing micro-scale inclusions were compared with that of mixtures containing nano-scale inclusions. The data set used for validation was

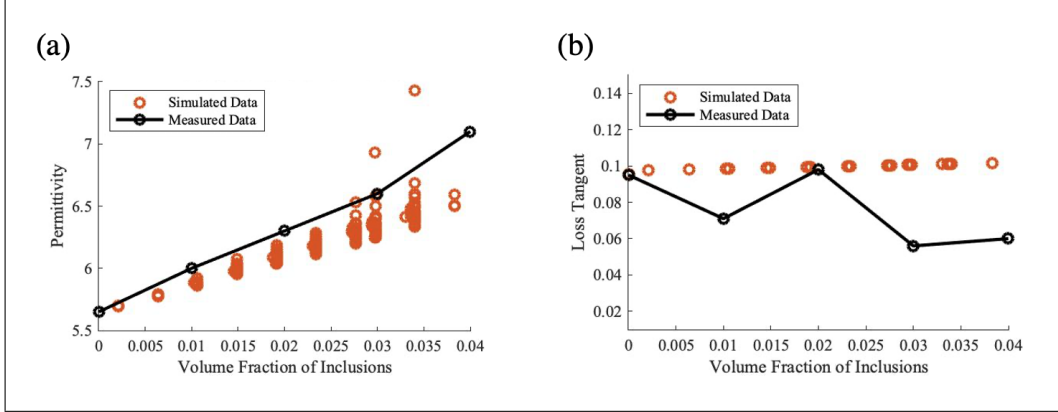


Figure 5.3: Comparison of measured data to analogous simulated data for (a) effective composite permittivity and (b) loss tangent consistent with experimental descriptions of Cu in a polyurethane host as provided in [20].

obtained from the mixtures containing micro-scale inclusions, as it is discussed in previous chapters that the dielectric properties of inclusions vary with scale. Initial validation focuses on the recreation of geometries with materials that exhibit known and minimally-variant bulk properties. It is also worth noting that metallic NPs in a dielectric insulating host can exhibit excessively high effective composite permittivities near the percolation threshold [59] [47]. As a practical consideration for MIC, it is also important to avoid high-volume-fractions of metallic inclusions since percolation can turn a capacitor into a resistor by forming a narrow conductive channel through the insulating dielectric.

To address this, the validation carried out in this section examines only the properties of low-volume-fraction composites. Figure 5.3 illustrates the correspondence of simulated approximations of composite dielectric properties with analogous measured data in [20] at low volume fractions. There are no fitting parameters in these simulations. The bulk material properties are extracted from the experimental papers, and the numerical artifacts were minimized by choosing an appropriate saturating value for the conductivity of the metallic inclusions.

In [19], copper NPs and aluminum NPs were each introduced into PVC and PMMA mixtures separately to produce four distinct composite mixtures on a range of low-volume fractions (< 5%). Figure 5.4 illustrates the correlation of simulated approximations of the

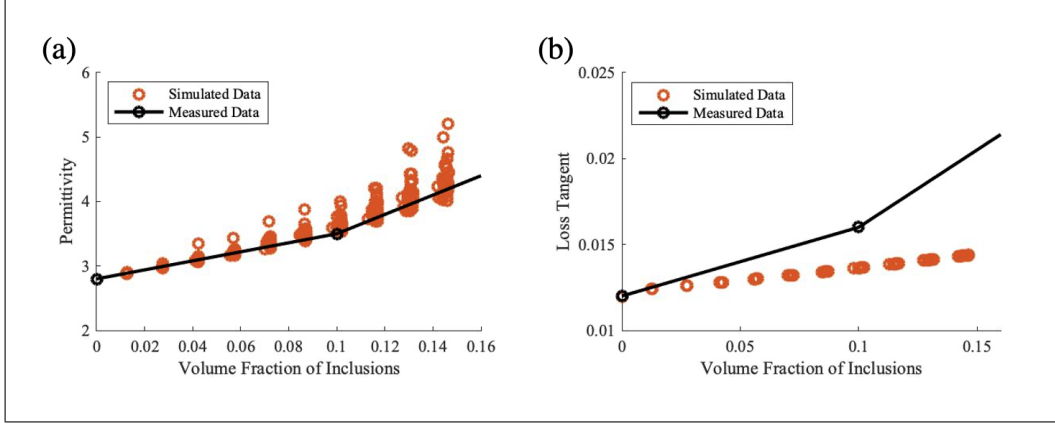


Figure 5.4: Comparison of measured data to analogous simulated data for (a) effective composite permittivity and (b) loss tangent consistent with experimental descriptions provided in [19] for Cu in a PVC host.

loss tangent and effective composite permittivity to measured data obtained from composites consisting of Cu NPs immersed in a PVC host.

Similarly, Figure 5.5 depicts the comparison of measured data to simulated data for Al filler in a PVC host, and while the correlation is clearly positive, a slight optimism is noted. Looking more closely at the volume fractions below 5% in both Figure 5.4 and Figure 5.5, the simulated data appears to match almost exactly. This once again reinforces the concept of conductivity saturation in MIC, as all simulation parameters are identical between the copper case in Figure 5.3 and the aluminum case in Figure 5.5 with the exception of the conductivity of the conductive NP material. As previously discussed, and illustrated in Figure 5.1 and Figure 5.2, changes in the conductivity of NP inclusions above a semiconducting range result in little to no change in effective composite permittivity. The conductivity used in the simulation of each of these corresponds to the actual conductivity of the respective metal adjusted by four orders of magnitude so as to avoid numerical error in multiplicative operations involving the complex permittivity of the inclusion and the host (i.e.  $\sigma_{cu} = 5.96 * 10^3$ ,  $\sigma_{al} = 3.77 * 10^3$ , and  $\sigma_{pvc} = 5.6 * 10^{-10}$ ).

Data in both [20] and [19] correlates to analogous approximations of the properties of simulated composites obtained using QESIM, but it is worth noting that there does appear

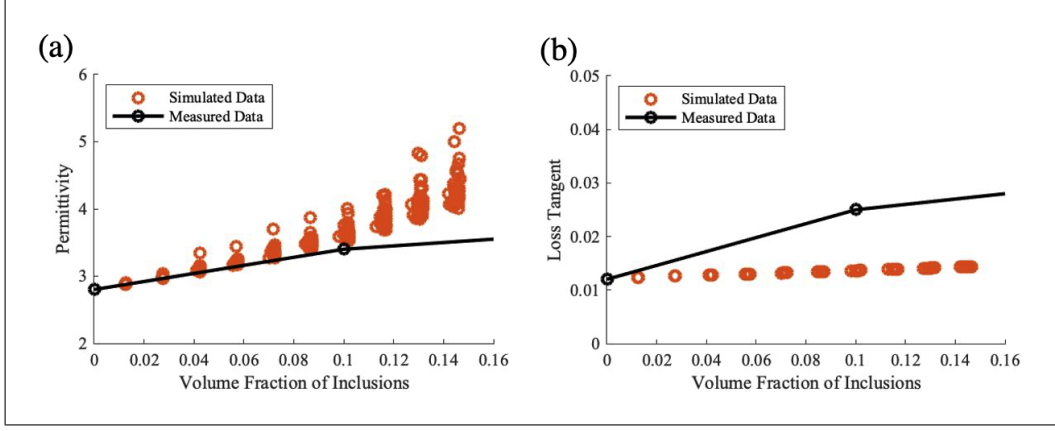


Figure 5.5: Comparison of measured data to analogous simulated data for (a) effective composite permittivity and (b) loss tangent consistent with experimental descriptions provided in [19] for Al filler immersed in a PVC host.

to be a large variability in the data presented in the greater body of literature on MIC. Unfortunately, no measured data was provided on the breakdown strength of these composites.

### 5.3 Investigation of Anomalous Properties in Au and Ag Metal-Insulator-Composites

During the process of validating the simulator to assure the accurate approximation of dielectric properties in MIC, two additional works were explored which detail the experimental measurements of permittivity and loss tangent from composites containing gold [22] and silver [21] NPs. Examining the permittivity data shown in Figure 5.6, it is clear that there exists a major discrepancy between the measured data and the data obtained from simulation. This immense increase in dielectric permittivity in the measured data far exceeds that which is made possible by conductivity-driven Maxwell-Wagner effects. As illustrated by Figure 5.1 and Figure 5.2, the Maxwell-Wagner polarization phenomenon that is approximated using COMSOL Multiphysics can also be successfully approximated using QESIM. Because QESIM has been validated in this way, it is clear that the exceptional effective permittivity that is reported in [22] and [21] cannot be attributed solely to Maxwell-Wagner polarization. This anomalous permittivity is especially interesting in [22], where composites with extremely low volume fractions of gold NPs (< 4%) exhibit

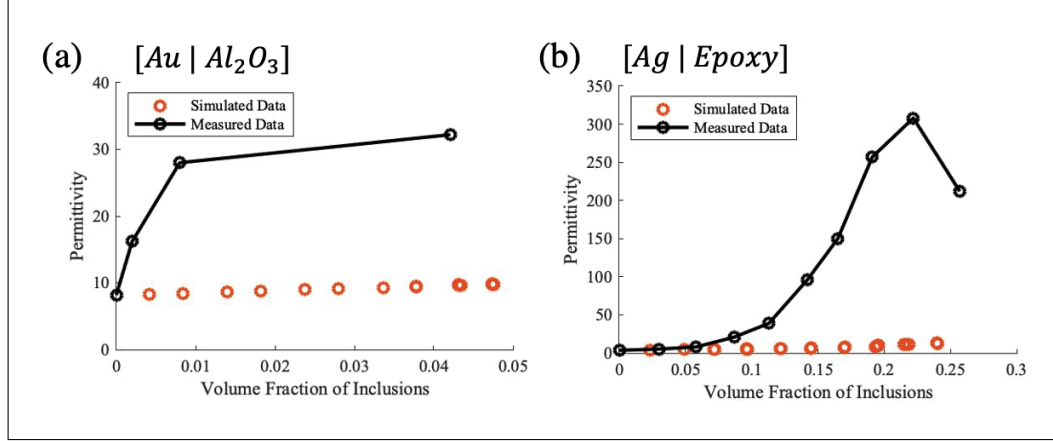


Figure 5.6: Comparison of measured effective composite permittivity from (a) [22] at 1 MHz, and (b) [21] at 1kHz to analogous simulated data.

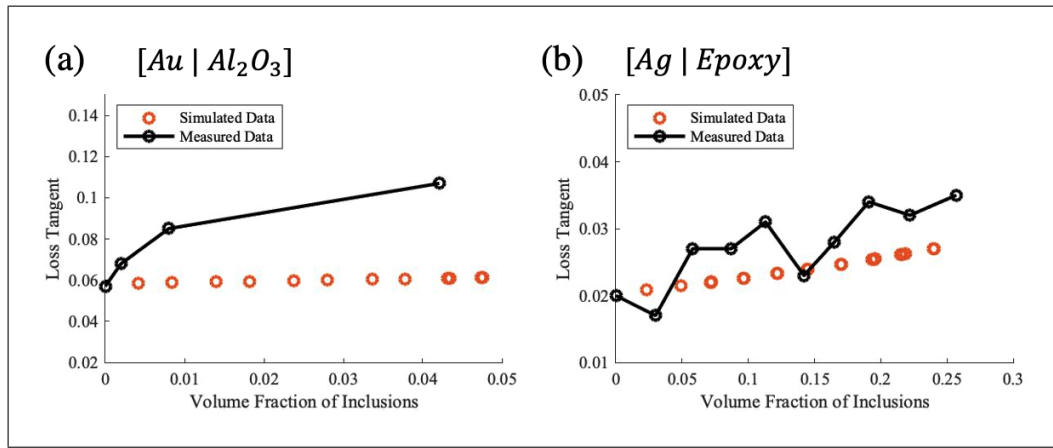


Figure 5.7: Comparison of measured effective loss tangent from (a) [22] at 1 MHz, and (b) [21] at 1kHz to analogous simulated data.

permittivities that roughly triple that of the host material. It is worth noting that despite the severe inaccuracy in the approximation of dielectric permittivity, the simulator remains consistent in its ability to approximate the mean of the loss tangent for all MIC studied in this chapter as illustrated in Figure 5.7 and in Figures 5.3(b), 5.4(b), and 5.5(b).

Upon examination of the validation of loss tangent against measured data, it is clear that the simulation is effective in approximating the expected trend as a function of volume fraction as can be seen in Figure 5.7(b). In Figure 5.7(a), however, this trend remains flat relative to the large increase in loss tangent over the small volume fraction range. Despite this, the simulator maintains its ability to approximate an apparent 'lower bound' on the

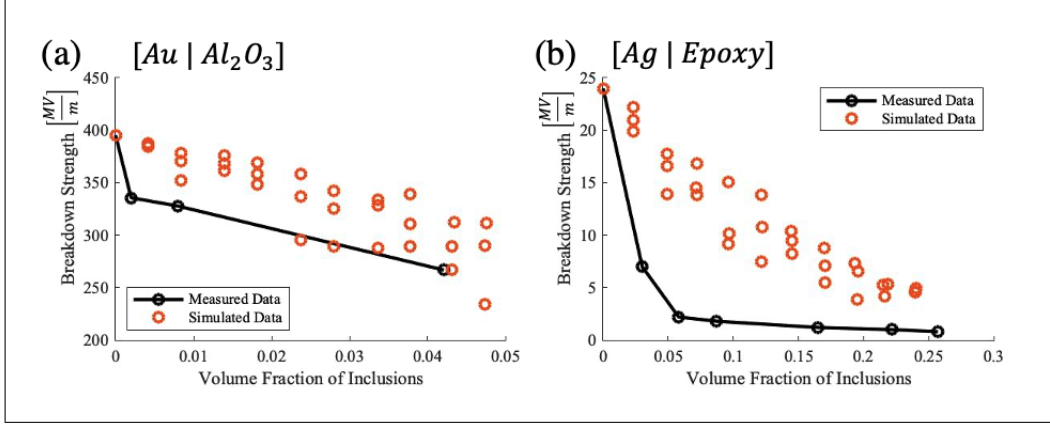


Figure 5.8: Comparison of measured effective breakdown strength from (a) [22] at 1 MHz, and (b) [21] at 1kHz to analogous simulated data.

loss tangent of such composites. This remains consistent with the goals of this work to explore the fundamental limits of energy storage properties in NP composite materials. Furthermore, the results obtained from simulation on dielectric breakdown strength show an optimistic result at low volume fractions when validated against data reported in [21], but at higher volume fractions this discrepancy is resolved. In addition, the breakdown model remains consistent when validated against data reported in [22] for Au/Al<sub>2</sub>O<sub>3</sub> MIC. This simulated data was obtained using the breakdown path model as outlined in Chapter 3, and the comparison of simulated and measured data shown in Figure 5.8(a) provides further validation for this model for MIC under certain conditions. In both cases, the simulated breakdown strength represents an upper bound, and the discrepancy between measured and simulated data can be attributed to a number of factors including the fact that QESIM does not account for imperfections in the composite like air-voids or disfigured inclusions. It is important to note that the theoretical upper bound approximated by this breakdown model will require further exploration through experimental work before definitive conclusions can be made regarding the optimality of certain composite architectures and recipes.

In the next chapter, these anomalous properties observed in MIC containing Au and Ag fillers are explored in depth to uncover possible explanations for the observation of high effective composite permittivity in such materials. Primarily, it is assumed that an interphase

is formed between the metallic NPs and the insulating host material that exhibits negative capacitance (NC) effects. Because the current understanding of NC materials is noted in the literature to be incomplete, the next chapter outlines a first-principles model for NC materials, and applies QESIM to simulate simplified geometries as well as randomly-dispersed NP composite geometries. These simulation experiments are designed to illustrate how such exotic material properties may lead to very high effective composite permittivity in certain MIC.

## 5.4 Summary & Conclusion

To explore a broader range of composite materials, the simulator has been modified to compute complex internal electric fields using complex dielectric permittivity for each constituent material. Accounting for the conductivity of constituent materials has enabled the simulation of Maxwell-Wagner polarization phenomena in MIC, and it has also allowed for the approximation of the loss characteristics of simulated composites. QESIM has been successfully validated against three MIC cases based on data reported in [20] and [19] illustrating the simulator's efficacy for the simulation of certain MIC. Conversely, QESIM has also shown that data reported in [22] and [21] cannot be modelled using classical EM models for the constituent materials. This suggests unusual dielectric behavior at the interphase between the conductive and insulating phases of those particular MIC. To address these unusual results, the exploration of negative capacitance (NC) effects has been proposed as the core focus of the next chapter. The intention of this subsequent exploration is to enable the simulation of a broader range of MIC material combinations.

## CHAPTER 6

### NEGATIVE CAPACITANCE AND INTERNAL VOLTAGE AMPLIFICATION

Over the last decade, increasing efforts have been carried out to explore negative capacitance (NC) in semiconductors. Because the large variations in effective permittivity (as noted in the previous chapter) can not be fully attributed to Maxwell-Wagner effects, further exploration is warranted. Recent research into dielectric-ferroelectric heterostructures has elucidated how the NC effect arises in multi-domain materials, and underscores the possibility of extremely high observed values of dielectric permittivity in specific material and geometric arrangements [23]. In several publications, this NC effect has been successfully leveraged to reduce geometric dimensions or improve the loss characteristics in ferroelectric FET (FEFET) [25] [24]. In addition, the body of literature on this topic indicates the potential for internal voltage amplification under DC applied potential due to the presence of hysteretic regions due to Maxwell-Wagner effects at the interphase between metallic and non-metallic domains [60] [61] [29]. While many works specifically note a limited understanding of the physical processes that lead to the observation of NC, several works attempt to describe the fundamental mechanism of action [28] [31] [26].

One possible explanation for the anomalous findings in [21] and [22] is the attribution of high effective permittivity to internal voltage amplification that results from DC-stable NC. In this chapter, a case is made for this attribution as numerous recent works are cited to clarify how NC effects may arise in specific types of heterostructures. This conceptual model is then used to design and carry out simulation experiments that seek to elucidate how these effects may lead to improvements in the energy storage characteristics of composite materials. In subsequent sections, a high level description of the simulation model is provided based on the current literature, and this is followed by the derivation of an analytical impedance model which is then used in conjunction with discrete simulations of simplest-

case laminate structures to understand the simulation parameters required to achieve internal voltage amplification within heterogeneous structures. These findings are then adapted from laminate-structures to spherical structures for the simulation of randomly-dispersed NP composite materials analogous to those studied in [21] and [22]. Finally, the results of these final simulations are used to further support the attribution of anomalous data discussed in the previous chapter to the presence of interfacial NC effects.

The core contribution of this chapter centers around the successful simulation of internal-voltage-amplification due to NC effects in randomly-arranged NP composites. This introduces a fundamental mechanism for permittivity maximization in certain types of composites, specifically for MIC. Based on the current literature and the findings detailed in this chapter, it is possible that this NC effect may be leveraged to engineer the next generation of energy storage materials. Ultimately, this work aims to guide future research that seeks to leverage the NC-induced internal-voltage-amplification for effective permittivity optimization.

## 6.1 Negative Capacitance (NC)

First and foremost, it is important to define what is meant by NC effects in materials. To aid in this explanation Figure 6.1 provides a series of simplified diagrams that clearly illustrate this concept in simple bi-phase laminate metal-insulator-metal (MIM) capacitors using sketches of the expected internal voltages. In a traditional single-phase MIM capacitor, the internal voltage is a straight line between the applied voltages at the anode and cathode as illustrated by Figure 6.1(a). The internal electric field ( $E$ ) is therefore equal to the negative slope of this voltage plot. If a different material is added like in Figure 6.1(b), (c), and (d), the electric fields within each material can be defined by relating the ratio of permittivities to the ratio of internal electric fields as given by Equation 6.1.

$$\frac{\varepsilon_1}{\varepsilon_2} = \frac{E_1}{E_2} \quad (6.1)$$

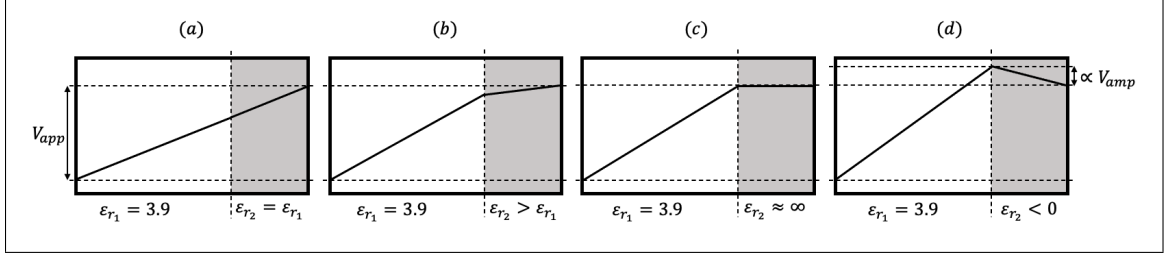


Figure 6.1: Simplified internal voltage diagrams for MIM capacitor consisting of one insulating layer (white) adjacent to a layer (gray) with (a) equal permittivity, (b) higher permittivity, (c) infinite permittivity (i.e. conducting), and (d) negative permittivity, where the proportionality to internal voltage amplification across the white insulating layer is noted.

Therefore, if the permittivity  $\epsilon_2$  is negative, the electric field is expected to act in the opposite direction and amplify the internal voltage as pictured in Figure 6.1(d).

NC effects are most commonly studied in systems containing ferroelectric materials, but several publications indicate that this effect is not necessarily coupled with ferroelectricity [32] [26] [62].

Rather, the source of such behavior may be explained more generally by a high density of localized charge-trapping states, as is characteristic of ferroelectric materials. That said, the impact of negative permittivity values in materials seems unusual, but it can in fact be illustrated at a high level with simple band diagrams of MIM capacitors as depicted in Figure 6.1.

It is worth noting that NC is known to occur only within heterostructures consisting of two distinct material domains that share direct contact at an interphase layer [23][26]. In [28], compelling case that DC stabilization of the NC effect is likely impossible due to its transient nature and reliance on inherently unstable ferroelectric domains. While the effect has been successfully leveraged in AC applications to achieve a reduction in power consumption and losses [24] [25], the idea of a DC-stable NC effect has long been considered impossible. In [61], however, it is stated that the NC effect can manifest in both transient and stable modes depending on the geometric arrangement of material domains. Specifically, it is stated that the direct contact of a ferroelectric domain with a simple positive-

permittivity dielectric can produce NC behavior in bi-layer laminate structures with a sufficiently thin ferroelectric layer. Moreover, [60] details the successful fabrication and testing of a heterojunction that exhibits NC-induced internal-voltage-amplification consisting of  $\text{La}_{0.8}\text{Sr}_{0.2}\text{MnO}_3$  and Nb-doped  $\text{SrTiO}_3$  subject to positive applied DC bias. In addition to this relatively early observation of a stabilized NC effect at DC applied potential, [60] also attributes the observed NC behavior to Maxwell-Wagner effects coupled with interfacial relaxation phenomena, and the subsequent formation of inductive effects. These inductive effects are likewise observed and discussed in [62], which discusses the source of inductive loops in lithium-ion energy storage devices, stating their origin is likely tied to the negative capacitance effect as it arises from the Maxwell-Wagner interfacial relaxation effects as opposed to electrolyte decomposition resulting from surface layer passivation, as was previously thought to be the case. Again, this points to not only the existence of the negative capacitance effect, but more importantly its link the interfacial chemistry that arises from the adjacency of metallic and non-metallic domains.

These works combine to paint a picture that illustrates the incidence of NC effects as arising from the formation of nano-scale material domains that contain high densities of trap states. It is clear that certain specific types of interphases can exhibit negative capacitance effects, and under certain conditions these effects can be leveraged to enhance the electric fields within certain types of composite materials. The fact that this is observed to be stable under DC applied potential indicated the potential for this effect to be leveraged in energy storage applications, warranting further research into the specific modes of operation for heterostructures with NC regions. This motivates the simulation experiments that follow, which aim to provide insight into how such systems can be understood from a semi-classical frame of reference.

## 6.2 Simulating Voltage Amplification in Laminates

To understand how these NC effects impact the dielectric properties of heterogeneous materials, it is first necessary to consider the simplest case in which negative capacitance has been observed. That is, the bi-layer heterostructure containing a single dielectric layer and a layer that exhibits negative capacitance (i.e. negative complex permittivity). The goal of this section is to examine how both the geometric and dielectric parameters of the material impact the effective permittivity of the entire device. To this end, an impedance-based analytical model is derived in this section to be used for the validation of subsequent QESIM simulations. The simulations in this chapter use QESIM to first model the aforementioned bi-phase laminate structures, and go on to simulate a large data set of randomly-arranged geometries for metallic NPs in an insulating host. Extrapolating the concept of NC laminate heterostructures to a 3-D confined spherical NP geometry, the viability of NC voltage amplification effects in randomly-structured composite materials.

### 6.2.1 Analytical Impedance Model

Before simulating the heterostructures discussed here, an analytical model is derived to describe the impedance and dielectric characteristics of the structures examined in this section. This analytical model is based on the circuit-level model that is depicted in Figure 6.2. In this model, the user-defined parameters include the relative complex permittivity and thickness of each ( $i^{th}$ ) material ( $\varepsilon_{r_i}^*$  and  $d_i$  respectively ). With these inputs, it is possible to obtain ample information about the behavior of the hypothetical materials and structures they represent. In particular, this work will examine the electric field with each constituent phase as well as the effective composite permittivity of the materials studied here. In addition, this analytical model is further leveraged to exploit an apparent asymptotic behavior that arises from a division-by-zero that can occur in theory when considering two parallel layers with perfectly-matched dielectric and geometric properties. This behavior has been

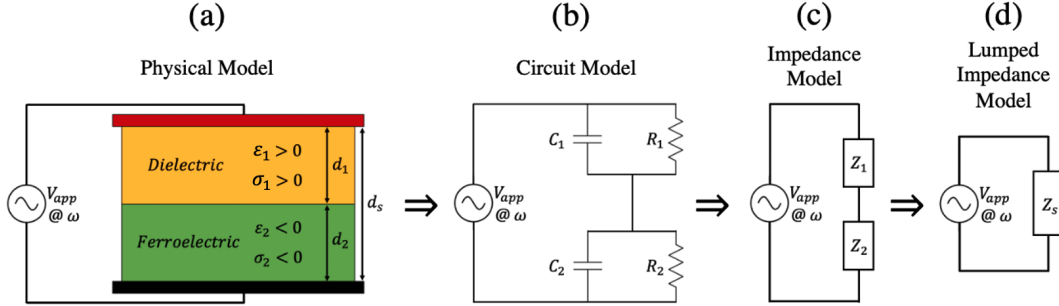


Figure 6.2: Circuit-level diagrams depicting of (a) physical model, (b) equivalent circuit model, (c) impedance model, and (d) lumped impedance model.

discussed as inherently related to the incidence of NC effects in [63] and [28], and has been attributed to positive feedback between the internal polarization mechanism between NC materials and the adjacent dielectric leading to catastrophic internal over-polarization. While those works focus on describing the incidence of NC effects and polarization catastrophe based on Feynman's pedagogical model for the origin of ferroelectricity, this work utilizes the impedance equations that arise from the circuit model given in Figure 6.2(b) to define specific geometric and dielectric material properties that can lead to polarization catastrophe, and therefore NC voltage amplification.

The derivation of this model begins with the use of known equations for the impedance of resistive components ( $R_i$ ) and capacitive components ( $C_i$ ) shown in Figure 6.2(b) to obtain equations that represent  $Z_1$  and  $Z_2$  as illustrated in Figure 6.2(c).

$$R_i = \frac{1}{\sigma_i} \frac{d_i}{A} \quad (6.2)$$

$$C_i = \epsilon_0 \epsilon_i \frac{A}{d_i} \quad (6.3)$$

Following widely-used conventions for representing the impedance of parallel components, Equation 6.4 is formed to represent the impedance of each layer, which is then used to

determine the distribution of electric fields within each layer of the heterostructure.

$$Z_i = \frac{1}{j\omega C_i + \frac{1}{R_i}} = \frac{1}{j\omega \varepsilon_0 \varepsilon_i \frac{A}{d_i} + \sigma_i \frac{A}{d_i}} = \left(\frac{1}{A}\right) \frac{d_i}{j\omega \varepsilon_0 \varepsilon_i + \sigma_i} \quad (6.4)$$

With this, the total impedance can simply be calculated as the sum of all series impedance values (i.e.  $Z_s = Z_1 + Z_2$ ). The ratio of individual impedance to total impedance for any given  $i^{th}$  layer is then used to determine the electric field distribution within each constituent phase by Equation 6.5, which relies on the principle of voltage division.

$$E_i = \frac{V_{app}}{d_i} \left( \frac{Z_i}{Z_s} \right) \quad (6.5)$$

Knowing the electric fields within each of the constituent phases then allows for the approximation of the total energy ( $\mathbf{E}_{tot}$ ) within the device as given by Equation 6.6.

$$\mathbf{E}_{tot} = \left(\frac{1}{2} A \varepsilon_0\right) (\varepsilon_1 d_1 (E_1 E_1^*) + \varepsilon_2 d_2 (E_2 E_2^*)) \quad (6.6)$$

As in previous chapters, the total energy is related to the effective composite permittivity by the assumption that the geometric capacitance of the device is that of an ideal parallel plate capacitor. Thus, Equation 6.7 leads to the formation of Equation 6.8.

$$C_{eff} = \frac{2\mathbf{E}_{tot}}{V_{app}^2} = \varepsilon_0 \varepsilon_{eff}^* \frac{A}{d_s} \quad (6.7)$$

$$\begin{aligned} \varepsilon_{eff}^* &= \frac{2d_s}{A\varepsilon_0 V_{app}^2} (\mathbf{E}_{tot}) \\ &= \frac{2d_s}{A\varepsilon_0 V_{app}^2} \left( \left(\frac{1}{2} A \varepsilon_0\right) (\varepsilon_1 d_1 (E_1 E_1^*) + \varepsilon_2 d_2 (E_2 E_2^*)) \right) \end{aligned} \quad (6.8)$$

Substitution and simplification of the expression given by Equation 6.8 ultimately results

in the formation of Equation 6.9.

$$\varepsilon_{eff} = \left( \frac{d_s}{(\alpha^2 + \omega^2 \varepsilon_0^2 \beta^2)^2} \right) \left( (\varepsilon_1 d_1)((\sigma_2 \alpha + \omega^2 \varepsilon_2 \varepsilon_0^2 \beta)^2 + \omega^2 \varepsilon_0^2 (\varepsilon_2 \alpha - \sigma_2 \beta)^2) + (\varepsilon_2 d_2)((\sigma_1 \alpha + \omega^2 \varepsilon_1 \varepsilon_0^2 \beta)^2 + \omega^2 \varepsilon_0^2 (\varepsilon_1 \alpha - \sigma_1 \beta)^2) \right) \quad (6.9)$$

$$\alpha = (d_1 \sigma_2 + d_2 \sigma_1)$$

$$\beta = (d_1 \varepsilon_2 + d_2 \varepsilon_1)$$

With this it is possible to determine the effective composite permittivity of the bi-layer structure. In the context of NC materials, it immediately becomes apparent that the denominator of Equation 6.9 could be equal to zero. This would result in a theoretically infinite effective composite permittivity, even within materials that exhibit insulating behavior. In this model, that is how polarization catastrophe is considered.

Finally, to determine the conditions required to induce polarization catastrophe as defined above, the denominator of Equation 6.9 is set to zero to obtain an expression that relates the ratio of material properties to the ratio of geometric properties. This final expression is given by Equation 6.10, and simplified to obtain two approximate design equations that define how polarization catastrophe can be achieved at high and low frequencies as given by Equation 6.11. For all steps in the simplification of this expression, see Equation A.56 in Appendix A3.

$$\begin{aligned} \frac{d_1}{d_2} &= -\frac{\sigma_1}{\sigma_2} \\ \frac{d_1}{d_2} &= -\frac{\varepsilon_1}{\varepsilon_2} \end{aligned} \quad (6.10)$$

$$\frac{d_1}{d_2} \approx \begin{cases} -\frac{\varepsilon_1}{\varepsilon_2} & \forall (\omega > 2\pi \times 10^6 [\frac{\text{rad}}{\text{s}}]) \\ -\frac{\sigma_1}{\sigma_2} \& -\frac{\varepsilon_1}{\varepsilon_2} & \forall (0 < \omega < 2\pi \times 10^6 [\frac{\text{rad}}{\text{s}}]) \\ -\frac{\sigma_1}{\sigma_2} & \forall (\omega \approx 0 [\frac{\text{rad}}{\text{s}}]) \end{cases} \quad (6.11)$$

Note that this model assumes all materials to be linear dielectrics because it aims to provide a generalized understanding of NC effects in a broader range of materials than just those that fall within the category of ferroelectrics. This generalization is primarily motivated by the fact that this work examines NC effects at the interphase between two materials, and such material domains cannot definitively be categorized as ferroelectric. Instead, these interphase domains are approximated as linear dielectrics that exhibit a negative complex permittivity. For the complete derivation including all equations given in this section as well as intermediate steps, see Appendix A3.

### 6.2.2 QESIM Laminate Model

The previous subsection provides guidance towards the simulation of polarization catastrophe in NC heterostructures. This model utilizes the parameter relationships that lead to polarization catastrophe, as derived for the analytical impedance model, to explore how the electric field distribution within laminate heterostructures can amplify effective composite permittivity as a consequence of induced polarization catastrophe. Illustrated in Figure 6.3, the simulator's ability to approximate the internal voltage characteristics of various heterostructures structures is proven to extend into the space of NC materials. In addition, Figure 6.3(d) illustrates the possibility for exceptional increases in effective composite permittivity due to the internal voltage amplification as discussed in previous sections. Because QESIM approximates these material phases as linear dielectrics, however, it is important to consider the stability of the system. Typically, a thinner NC region is required to maintain DC stability of the NC effect, but to emphasize the theoretical limits of this effect, a thicker NC layer was simulated. The simulations outlined here have been included to

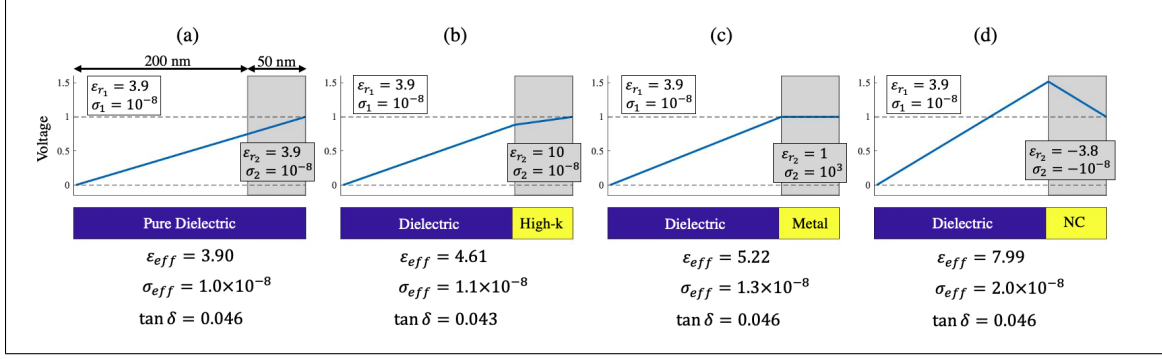


Figure 6.3: Plots of internal potential field within simulated MIM capacitors simulated at 1kHz, consisting of one 200nm dielectric insulating layer (white) adjacent to a 50nm layer (gray) exhibiting (a) equal permittivity, (b) higher permittivity, (c) conductive properties, and (d) negative capacitance.

illustrate the point that QESIM is capable of simulating the internal-voltage-amplification effects that originate from certain configurations of NC and dielectric layers in bi-phase laminate heterostructures.

### 6.2.3 Model Comparison

Comparing the effective permittivity values shown in Figure 6.3 to values obtained using the analytical solution given by Equation 6.9, the error has been calculated for each case. These values are given in Table 6.1 and Table 6.2, and the values calculated reinforce the validation of QESIM for the calculation of both effective permittivity and effective conductivity for common laminate structures including both insulators and conductors. Furthermore, the low error exhibited by case (d) illustrates the efficacy of QESIM in the approximation of effective permittivity for heterogeneous materials containing explicitly defined NC domains. It is worth noting, that case (d) exhibits the highest effective conductivity, even exceeding that of case (c) which includes a metallic layer. Despite this, each case exhibits loss tangent of  $\tan \delta \approx 0.045 \pm 0.002$ .

The cases detailed above focus on the simulation of a single geometric arrangement, but for NC heterostructures changes in the thickness of the NC domain can lead to drastic changes in effective permittivity when geometric and dielectric properties are nearly

Table 6.1: Comparison of results from effective real permittivity ( $\varepsilon'_{eff}$ ) approximation obtained using QESIM to equivalent data obtained using the analytical impedance model at 1kHz for bi-phase laminates as derived in this chapter.

Case	Simulated $\varepsilon'_{eff}$	Analytical $\varepsilon'_{eff}$	% Error
(a)	3.9000	3.9000	$1.1 \times 10^{-14}\%$
(b)	4.6101	4.6021	0.17404%
(c)	5.2176	5.2000	0.33784%
(d)	7.9868	7.9040	1.04790%

Table 6.2: Comparison of results from effective conductivity ( $\sigma_{eff}$ ) approximation obtained using QESIM to equivalent data obtained using the analytical impedance model at 1kHz for bi-phase laminates as derived in this chapter.

Case	Simulated $\sigma_{eff}$	Analytical $\sigma_{eff}$	% Error
(a)	$1.0000 \times 10^{-8}$	$1.0000 \times 10^{-8}$	$8.3 \times 10^{-14}\%$
(b)	$1.0981 \times 10^{-8}$	$1.0971 \times 10^{-8}$	0.09176%
(c)	$1.3378 \times 10^{-8}$	$1.3333 \times 10^{-8}$	0.33784%
(d)	$1.9989 \times 10^{-8}$	$2.0193 \times 10^{-8}$	1.01891%

matched as noted by the design equations given by Equation 6.11. The analytical solution also provides insight into the incidence of polarization catastrophe that matches data obtained via QESIM as is illustrated in Figure 6.4. This plot details the dataset obtained from a set of 100 geometries with constant total sample thickness and varying NC and dielectric material thickness. The thickness of the NC region is represented on the x-axis as a percentage of the total device thickness, and the asymptotic behavior that is expected in the real part of the effective permittivity can be seen in both the analytical solution as well as in the simulated data at the expected device thickness. The average error over the entire sweep of NC domain thicknesses shown in Figure 6.4(a) and (b) are calculated to be 4.43% for the low-frequency case (a) and 4.49% for the high-frequency case (b). Likewise, the average error of simulated data shown in Figure 6.4(c) and (d) are calculated to be 2.01% for the low-frequency case (c) and 2.01% for the high-frequency case (d). This error is calculated using the average of 100 points including all points near the polarization catastrophe, and so a slightly higher error is expected. This reinforces the efficacy of QESIM towards modeling NC-induced amplification of internal polarization in heterogeneous materials. While

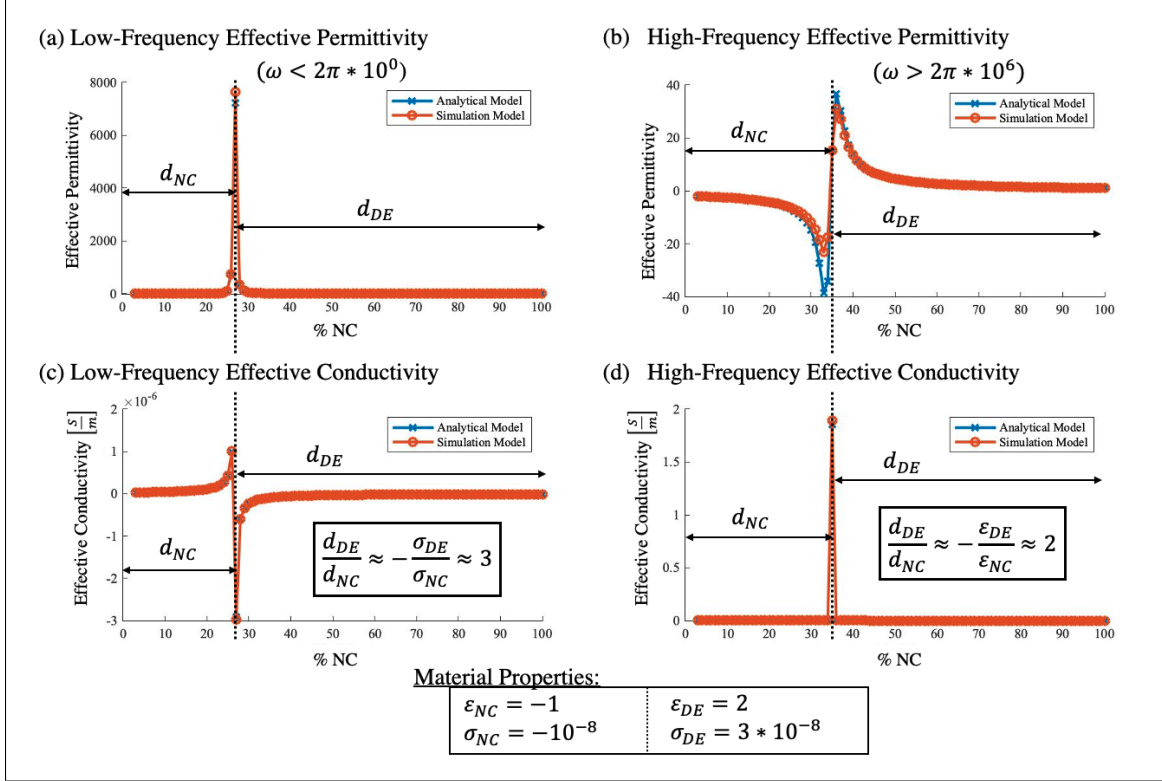


Figure 6.4: Plots depicting the dependence of effective permittivity on NC layer thickness for bi-phase NC heterostructure at (a) high-frequency and (b) low-frequency, and the dependence of effective conductivity on NC layer thickness at (c) high-frequency, and (d) low-frequency. Design equations are employed to further express the efficacy of the analytical model for the prediction of geometric and material property combinations that lead to polarization catastrophe.

the effective conductivity shows large spikes near the point of polarization catastrophe, the effective permittivity tends to offset this so that the overall loss tangent largely remains below 0.01 in both high and low frequency cases. This is expected based on observations of low-loss characteristics in real NC devices in [61].

### 6.3 Simulating Voltage Amplification in Stochastically-Arranged Composites

Based on the validation carried out in the previous section, this section details two simulation experiments which successfully recreate the anomalous permittivity that has been observed in real-world MIC in [22] and [21]. The anomalous data is hypothesized to be attributed to the formation of a NC interphase layer which provides internal voltage ampli-

fication in regions proximal to the NPs within the composites. This conceptual model is consistent with the data published in [64] and [65], which discuss the viability of NC interphase layer formation in regions adjacent to metallic domains that exhibit work functions comparable to that of Au and Ag. These simulations are designed to illustrate the possibilities of leveraging the internal-voltage-amplification effects that are associated with NC materials in the context of stochastically-arranged composite materials. While the results in this chapter show promise, it should be noted that this area of research is in its relative infancy, so more work is necessary to make definitive conclusions on the actual viability of such materials as effective energy storage media. Ultimately, this chapter aims to provide an explanation for the anomalous data noted in the previous chapter that elucidates the possibility of NC domain formation in MIC.

### 6.3.1 Considerations for Nanoparticles With NC Interphases

As this section focuses on the shift from a simple bi-phase laminate model to one that includes randomly-dispersed spherical inclusions, it is important to consider how the design equations derived in this chapter may be leveraged to simulate voltage-amplifying NC effects in disordered composite systems. The addition of an interphase shell layer with NC properties is intended to achieve sufficient internal voltage amplification to match the anomalous data reported in [22] and [21]. One important parameter, as noted in the design equations given by Equation 6.11, is the thickness of this shell layer ( $t_{shell}$ ). This shell thickness is determined from observations of the electric field distributions within previously simulated Au and Ag MIC cases as shown in Figure 6.5

The fundamental mechanism of voltage amplification in NC heterostructures is theorized to be rooted in a positive feedback mechanism involving the opposition of charges within two finite domains [28]. The simulations carried out in this section assume that when these charge densities are perfectly matched in opposition, the resulting internal voltage amplification then leads to polarization catastrophe. In laminate heterostructures, the

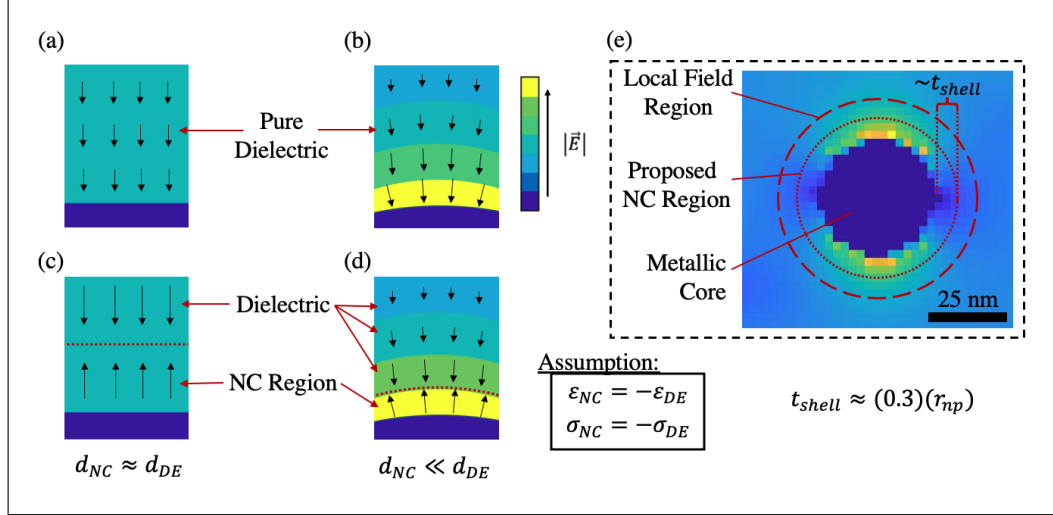


Figure 6.5: Illustration of internal electric field distribution within composites consisting of (a) positive dielectric adjacent to planar laminate metallic region, (b) positive dielectric adjacent to curved metallic region, (c) NC planar heterostructure adjacent to planar laminate metallic region, (d) NC curved heterostructure adjacent to curved metallic region, and a cross section of the simulated electric field from NP MIC showing (e) the relative width of high-electric-field regions adjacent to metallic spheres, and indicating the proposed shell thickness ( $t_{shell}$ ) as a function of the NP radius ( $r_{np}$ ).

electric field magnitude ( $|\vec{E}|$ ) is uniform within each layer, and so the approximate relationship of dielectric properties to layer thicknesses as given by Equation 6.11 is appropriate for those particular systems. This is shown in Figure 6.5(a) and (c). When considering a curved geometries, however,  $|\vec{E}|$  varies considerably within each domain as illustrated in Figure 6.5(b) and (d). The case of the curved surface shows the accumulation of high electric fields near the metallic surface, which is a result of Gauss' law. In Figure 6.5(c) and (d), the dotted line separates two regions in the laminate case and in the curved-geometry case that have equivalent total energy. In the laminate case pictured in (a) and (c), because the electric fields are uniform, this dashed line is expected to separate the region into two halves of equal volume. Conversely, the curved-geometry case in (b) and (d), this dashed line separates one small volume with high electric field (NC region) from a much larger volume with lower electric field (dielectric region). It is assumed that the voltage amplification effect can present itself with much thinner films in curved-geometries when compared to laminate structures, therefore justifying a small shell thickness despite the comparatively

Table 6.3: Constituent material simulation parameters used to recreate anomalous data reported in [22] and [21].

Case	Inclusion	Host	Shell	Nanoparticle
Au in Al <sub>2</sub> O <sub>3</sub>	$\varepsilon_i = 1$ $\sigma_i = 4.1 * 10^3 \left[ \frac{S}{m} \right]$	$\varepsilon_h = 8.2$ $\sigma_h = 2.6 * 10^{-5} \left[ \frac{S}{m} \right]$	$\varepsilon_s = -8.2(0.95)$ $\sigma_s = -2.6 * 10^{-5} \left[ \frac{S}{m} \right]$	$r_{np} = 3nm$ $t_{shell} = 1nm$
Ag in Epoxy	$\varepsilon_i = 1$ $\sigma_i = 6.3 * 10^3 \left[ \frac{S}{m} \right]$	$\varepsilon_h = 3.6$ $\sigma_h = 7.9 * 10^{-8} \left[ \frac{S}{m} \right]$	$\varepsilon_s = -3.6(0.995)$ $\sigma_s = -7.9 * 10^{-8} \left[ \frac{S}{m} \right]$	$r_{np} = 20nm$ $t_{shell} = 6nm$

large volume of dielectric host material. Based on this, the thickness of the NC region has been fixed to Equation 6.12 for the purpose of the simulations carried out in this section.

$$t_{shell} \approx (0.3)(r_{np}) \quad (6.12)$$

Where  $r_{np}$  represents the radius of the NP and  $t_{shell}$  represents the thickness of the NC shell as pictured in Figure 6.5. Ultimately, the concepts illustrated in Figure 6.5 justify the choice to relate the shell thickness to NP radius by Equation 6.12, and also supports the choice to employ relatively thin NC interphase shells.

### 6.3.2 Validation Against Anomalous MIC

At this point, a new model has been established for the simulation of metallic NPs with NC interphase shells. This model is employed to recreate the anomalous properties observed in Au/Al<sub>2</sub>O<sub>3</sub> and Ag/Epoxy MIC. To this end, two simulation experiments have been designed and carried out with parameters as detailed in Table 6.3.

For each case, over 300 randomly-generated geometries were simulated, and the effective dielectric properties were calculated based on the electric field approximation obtained from QESIM. The effective dielectric properties (i.e. permittivity, loss tangent, and breakdown strength) of the simulated composites were calculated using the equations and models detailed in chapters. The results detailed in this section illustrate the viability of NC interphase formation as a possible explanation for the anomalous results that have been observed in certain MIC.

To obtain a proper match to the measured data, the point of perfect matching for polarization catastrophe was assumed to be at the point where the permittivity and conductivity of the host matched that of NC shell (i.e.  $\varepsilon_s, \sigma_s = -\varepsilon_h, -\sigma_h$ ). Then, varying the permittivity of the shell in increments of 0.5%, the effective dielectric properties of the simulated composites were compared to those of the measured composites. For the case involving Au NPs, the best match for shell permittivity appeared 1% above the permittivity of the host. For this case involving Ag NPs, the best match appeared 0.5% below the point of polarization catastrophe. The reason for this offset is likely due to imperfect matching, and it is not clear how the best value for shell permittivity may be determined. The most important takeaway from this chapter, however, is independent of this slight offset. Rather, the very fact that values such as those published in [22] and [21] have been simulated using the methods discussed in this chapter warrant further exploration into the possible benefits of NC interphases in MIC containing high-work-function metals like Au and Ag.

### *Effective Real Permittivity*

Examining the simulated data juxtaposed against measured data from [22], it is clear that QESIM is capable of simulating composites such as these. The important point illustrated in Figure 6.10 is the fact that effective permittivity enhancements greater than 2x have been simulated for volume fractions under 4% using the model presented in this chapter. As noted in Chapter 5, this is not possible using classical models that do not consider negative capacitance effects.

Likewise, Figure 6.7 shows an exceptional correlation between measured data reported in [21] and that obtained using QESIM considering NC effects. Figure 6.7(a) and (b) illustrate the close match of the mean of simulated data to the reported measured data over the entire range of volume fractions studied, while Figure 6.7(c) and (d) illustrate the close correlation of effective permittivity data at volume fractions below 13%. Together, Figure 6.10 and Figure 6.7 show that the models presented in this chapter can be used

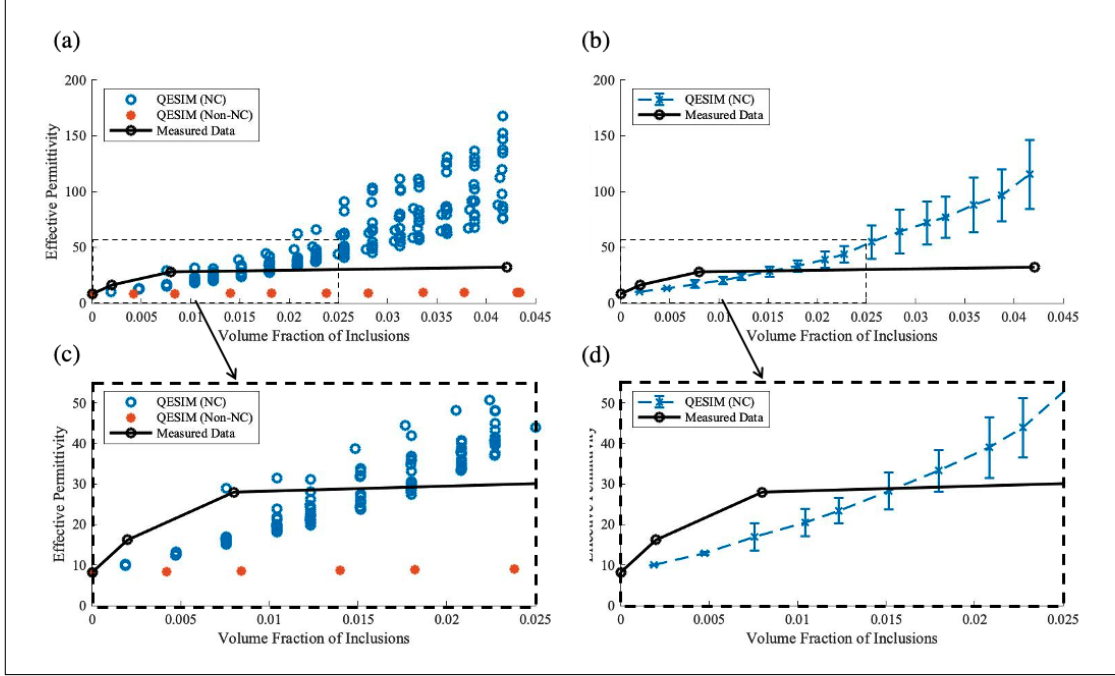


Figure 6.6: Comparison of simulated effective permittivity data on Au-Al<sub>2</sub>O<sub>3</sub> MIC obtained using QESIM to measured data reported in [22] showing (a) a complete scatterplot including all simulated cases, (b) the mean and standard deviation of simulated data at each volume fraction, (c) a partial scatterplot showing the low-volume-fraction cases, and (d) the mean and standard deviation of simulated data for low-volume-fractions.

to accurately predict the effective permittivity of real-world composites, including that of anomalous composites containing high-work-function metals like Au and Ag.

### *Loss Tangent*

In addition to the dielectric permittivity, the loss tangent was calculated using the simulated electric field approximations. As outlined in Chapter 5, the model used for the calculation of loss tangent is based on the total power. In Figure 6.8, it is clear that QESIM provides an optimistic estimate of loss tangent for these simulated MIC. Being that the data covers a small window of low volume fraction composites (< 4%), it follows that a low variability is expected. Despite this, QESIM accurately tracks the trend of increasing loss tangent with increasing volume fraction as expected, and it is worth noting that the loss tangent values of NC simulated composites exceed those of non-NC simulated composites by as much as

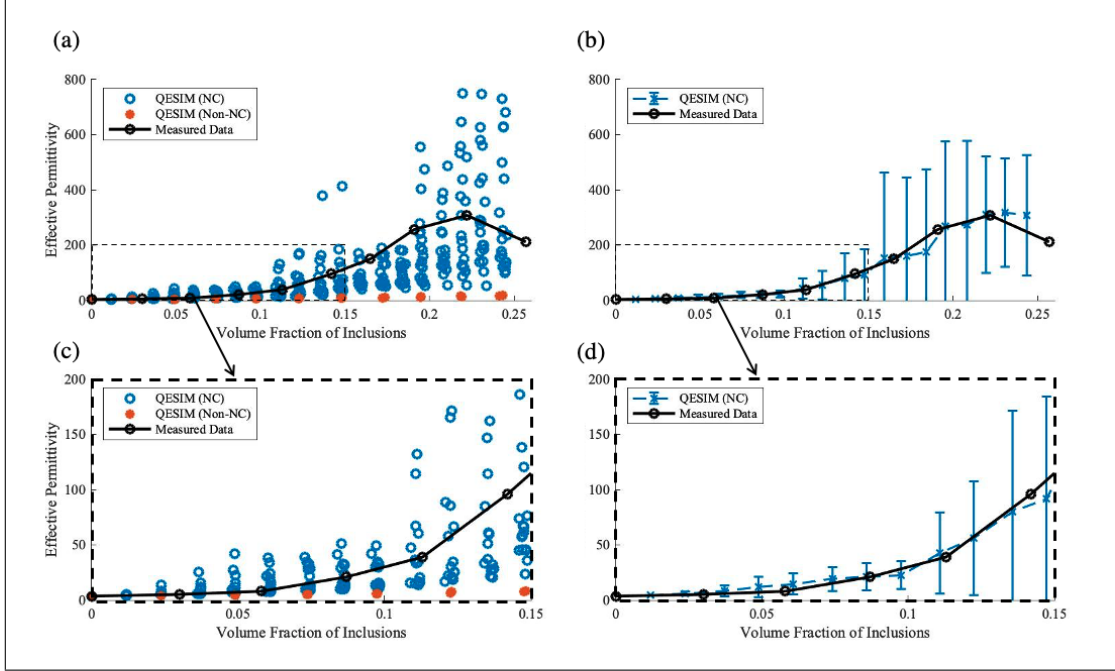


Figure 6.7: Comparison of simulated effective permittivity data on Ag-epoxy MIC obtained using QESIM to measured data reported in [21] showing (a) a complete scatterplot including all simulated cases, (b) the mean and standard deviation of simulated data at each volume fraction, (c) a partial scatterplot showing the low-volume-fraction cases, and (d) the mean and standard deviation of simulated data for low-volume-fractions.

20%

Similarly, in Figure 6.9, QESIM provides a slightly optimistic estimate when considering the mean of the simulated data, but the variations in loss tangent for these simulated composites encapsulate the measured data almost entirely. The high variability of the measured data can be observed in its jagged nature, and so the variability of the simulated data is expected, and further indicates the accuracy of the model used to obtain the simulated data in this chapter. Both of these figures illustrate the advantages of utilizing the NC interphase layer model for more accurate simulation of anomalous MIC for both real and imaginary components of complex permittivity.

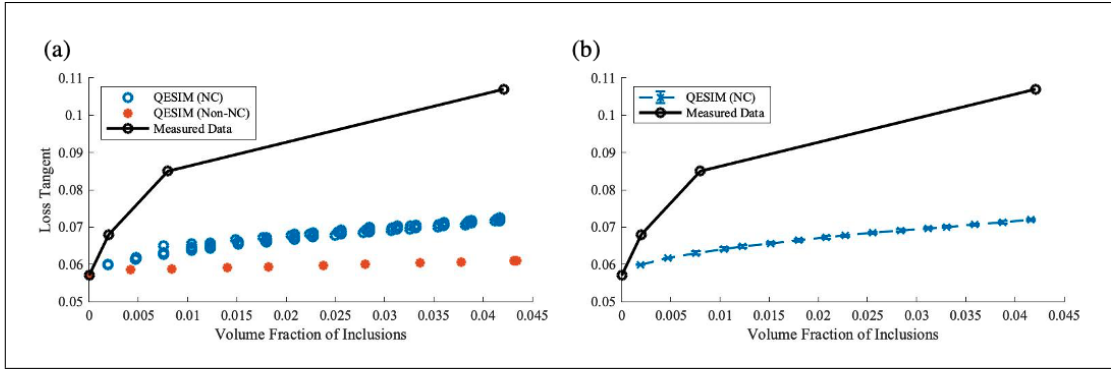


Figure 6.8: Comparison of simulated loss tangent data on Au-Al<sub>2</sub>O<sub>3</sub> MIC obtained using QESIM to measured data reported in [21] showing (a) a scatterplot of NC data (blue) and non-NC data (red) and (b) the mean and standard deviation of simulated data at each volume fraction.

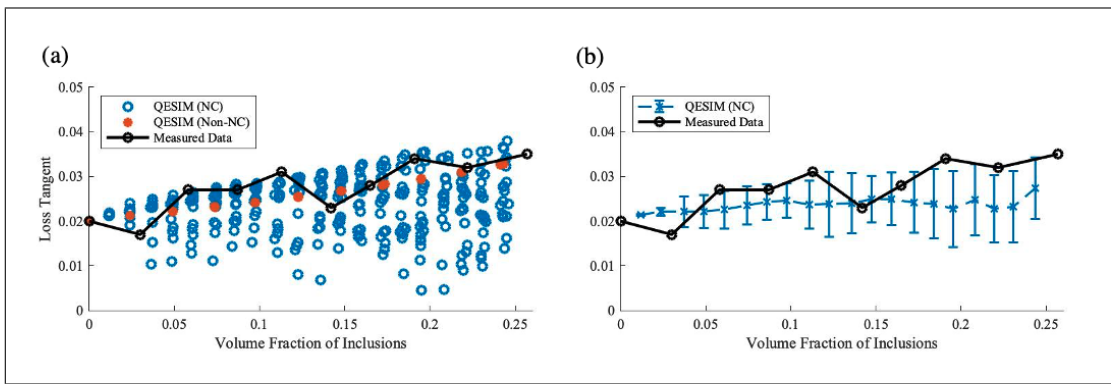


Figure 6.9: Comparison of simulated loss tangent data on Ag-epoxy MIC obtained using QESIM to measured data reported in [21] showing (a) a scatterplot of NC data (blue) and non-NC data (red) and (b) the mean and standard deviation of simulated data at each volume fraction.

### *Breakdown Field Strength*

Finally, to allow for the calculation of maximum theoretical energy density, the breakdown strength of simulated composites was approximated using the breakdown path model as detailed in Chapter 3. Validation against measured data obtained from the composites containing Au NPs shows that the simulator was effective for composites with low volume fractions (< 3%), but above that it appears that the simulated breakdown falls below what was measured in [22]. This may be related to what was observed in the mismatch between measured and simulated permittivity above 3%, as generally higher permittivity materials

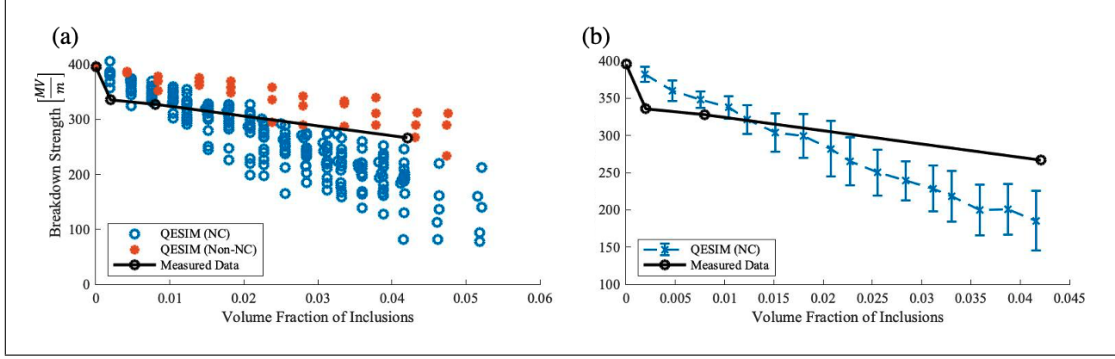


Figure 6.10: Comparison of simulated breakdown field strength data on Au-Al<sub>2</sub>O<sub>3</sub> MIC obtained using QESIM to measured data reported in [21] showing (a) a scatterplot of NC data (blue) and non-NC data (red) and (b) the mean and standard deviation of simulated data at each volume fraction.

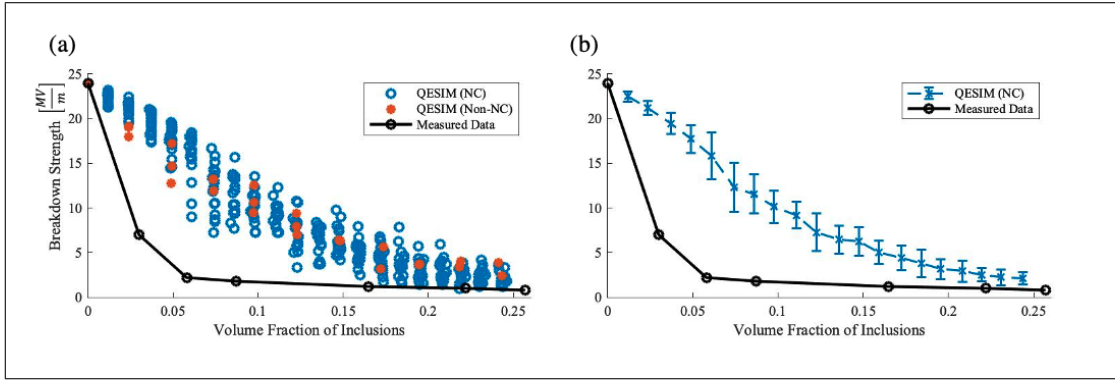


Figure 6.11: Comparison of simulated breakdown field strength data on Ag-epoxy MIC obtained using QESIM to measured data reported in [21] showing (a) a scatterplot of NC data (blue) and non-NC data (red) and (b) the mean and standard deviation of simulated data at each volume fraction.

are expected to experience lower breakdown strength [52].

Conversely, when examining the validation against data obtained from composites containing Ag NPs in Figure 6.13, it becomes apparent that the simulated breakdown strength provides a highly optimistic approximation at lower volume fractions. In [21], it is mentioned that the fabrication process used would introduce air voids was observed at both high and low volume fractions, with the air voids impacting dielectric permittivity at volume fractions above 20%. This may explain the sharp drop in breakdown strength at around 2% that is characteristic of this measured data.

With this validation data, it can be concluded that QESIM is capable of reproducing

trends and average values close to that which may be expected in measured data, but like all simulation tools QESIM has its limits. First, the breakdown model captures general trends, but sometimes fails to account for large drops in breakdown strength (likely due to unintended impurities). As noted in previous chapters, the models used to construct this simulator assume ideal materials with no air voids, and so it is expected that this simulator may overestimate the breakdown strength and dielectric permittivity, while underestimating the loss tangent of simulated composites. This lends itself to the exploration of fundamental limits of composite materials, and as such, QESIM can be used to identify composite geometries and material combinations geometries that may be advantageous for energy storage and other applications.

### *Maximum Energy Density*

Using the measured breakdown strength and effective composite permittivity reported in [21] and [22], the maximum theoretical energy density was calculated using Equation 6.13 with a practicality factor of  $\zeta = 0.5$  as used in previous chapters.

$$u_{max} = \frac{1}{2}\varepsilon_{eff}\varepsilon_0(\zeta E_{bd})^2 \quad (6.13)$$

It was found that the energy densities of MIC with Au filler calculated from the measured data in [22] show an increase in overall energy density when compared with that of the pure Al<sub>2</sub>O<sub>3</sub> host. The energy densities calculated from measured data on Ag filler in [21], however, fail to exceed that of the pure host material. Figure 6.12 includes both the NC and non-NC simulated data as well as the measured data from [22] to illustrate how the presence of NC interphase layers can enhance the overall energy density of certain MIC. In Figure 6.12(a) the red points (non-NC) indicate a steadily decreasing energy density with increasing volume fraction of inclusions that would be expected in non-NC materials. This is in stark contrast to the blue points representing the QESIM data simulated with NC in-

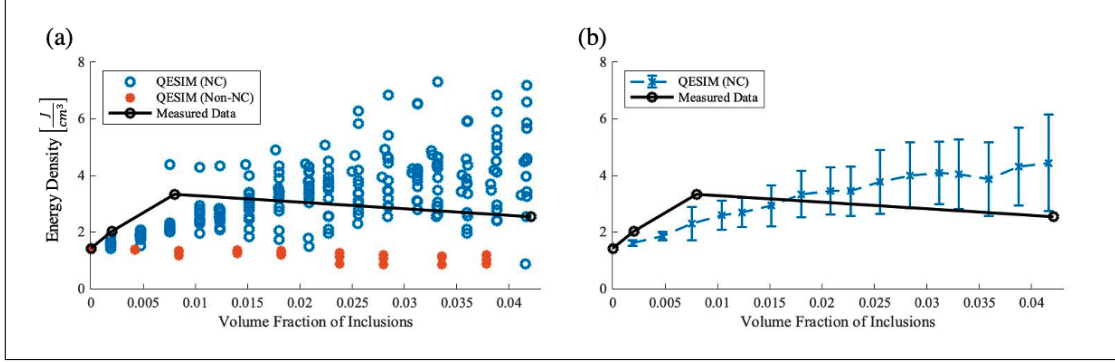


Figure 6.12: Comparison of simulated maximum energy density on Au-Al<sub>2</sub>O<sub>3</sub> MIC obtained using QESIM to measured data reported in [22] showing (a) a scatterplot of NC data (blue) and non-NC data (red) and (b) the mean and standard deviation of simulated data at each volume fraction.

terphases, which on average provide a closer match to the measured energy density in [22]. This measured data shows a maximum energy density of 3.4  $\left[\frac{J}{cm^3}\right]$ , which is an increase of nearly 130% compared to the pure host material. At a volume fraction just under 1%, this highlights a possible opportunity for energy density enhancement using MIC that exhibit NC properties as possible energy storage media. The simulated data provides a close match to measured data and shows that certain geometries can achieve energy densities even higher than this with the highest simulated energy density value at 7.3  $\left[\frac{J}{cm^3}\right]$ . That is an increase in energy density of as much as 385% for best-case simulated geometries compared to the pure host material. This should be considered as an optimistic upper bound because of the previously-noted overestimation of effective composite permittivity.

#### 6.4 Summary & Conclusions

In summary, a new model has been detailed and implemented for the accurate simulation of NC effects in both laminate heterostructures and for randomly-dispersed MIC containing spherical metallic filler. The analytical model derived in this chapter was compared to QESIM, and the error has been calculated to be below 5% for both high-frequency and low-frequency behavior of NC heterostructure systems. Furthermore, disordered composite systems were simulated containing metallic NPs with NC interphase shells. These sim-

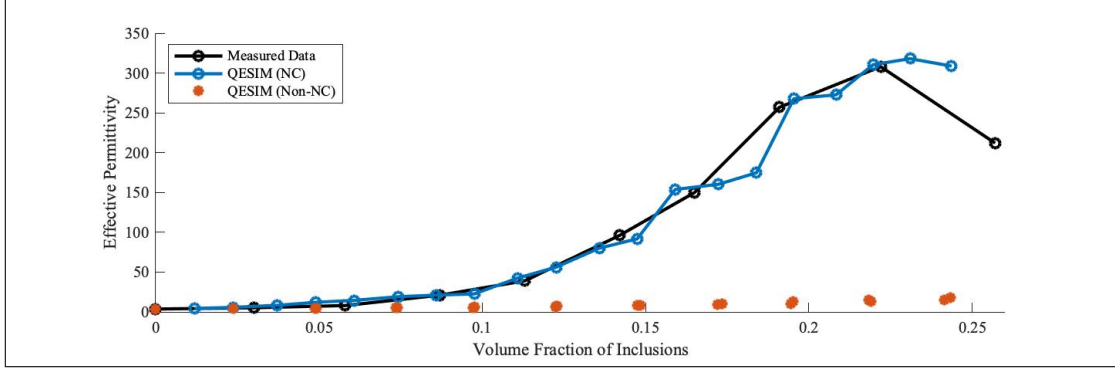


Figure 6.13: Average of simulated effective permittivity values obtained using QESIM with the NC interphase model (blue line), juxtaposed against non-NC QESIM data (red points) and measured data reported in [21] (black line).

ulations show a close match to the measured data reported in [22] and [21], indicating the possibility for NC domain formation in a broader range of composite systems than previously thought possible. It is concluded that the NC effect can be leveraged to induce internal voltage amplification even within disordered heterogeneous systems like NP composite materials, and in some cases the increase in dielectric permittivity can result in greater overall energy density despite the disadvantages that are commonly associated with MIC in energy storage applications. Furthermore, the close match of the simulated NC data to real-world measured data obtained from Ag/Epoxy MIC as observed in [21] could indicate the possibility of NC-type behavior in polymers. This is a significant observation as most works that explore NC effects observe such phenomena in highly-ordered crystalline solids like perovskites. The prospect of achieving NC internal-voltage-amplification in polymer-based composites could lead to next-generation composite materials for a multitude of applications. Polymer-based materials are known for their processability, making them preferable over materials like perovskites which often require fabrication via epitaxial growth. Polymer-based NC materials have exceptional potential for the enhancement of internal electric fields, which could be leveraged to enhance power scaling for a range of applications without increasing fabrication costs.

Finally, examining the energy density of Au-Al<sub>2</sub>O<sub>3</sub> MIC, both measured and simulated

data shows a significant potential for the enhancement of maximum energy density. In measured data reported in [22], MIC with a volume fraction of Au inclusions just under 1% show a maximum energy density of up to  $3.4 \left[ \frac{J}{cm^3} \right]$ , representing an increase in energy density of up to 130% compared to the pure host material with a maximum energy density of  $1.5 \left[ \frac{J}{cm^3} \right]$ . In addition, the best-case simulated geometry shows a possible energy density enhancement of up to 385% when compared to the pure host material.

It is worth noting that the conclusions presented in [22] attribute the anomalous measured permittivity values to an abundance of charge-trapping states at nanoparticle interphases. This, combined with reports of possible negative capacitance effects resulting from the formation of interphase regions that contain high concentrations of charge-trapping states, highlights negative capacitance as the most promising explanation for such anomalous permittivity values as seen in [22] and [21]. It is important to note, however, that additional research is warranted in this area to confirm these explanations through experimentation. In total, the goal of future experimental work aims to utilize the findings in this chapter towards the realization of NC-enhanced energy storage materials.

## CHAPTER 7

### **EXPLORATION OF ENGINEERED CORE-MULTISHELL NANOPARTICLES**

The greater body of literature on solid-state composite materials for energy storage applications indicates dielectric permittivity and breakdown strength as the two properties that contribute most significantly to the density of energy stored within any given material. While Chapters 5 and 6 of this document outline strategies for the amplification of dielectric permittivity in composites by the inclusion of highly polarizable nanoparticles (NPs), this enhancement is known to come at the expense of reduced breakdown strength [52]. To combat this, this chapter explores how the material structure and composition of NP filler can be engineered for the mitigation of dielectric breakdown. Interestingly, [4], [66], and [67] discuss the breakdown-strength-enhancing properties associated with core-shell filler. This aligns with the fact that larger electric fields tend to arise at the interphase between high-k and low-k materials, and points to an opportunity for the engineering of spherical filler architectures that could lead to higher breakdown strength without sacrificing effective composite permittivity. Additionally, one major challenge in the development of high energy density composites discussed in [4] is the reduction in breakdown strength that occurs because of the inclusion of high-k filler material. This, combined with research published in [67], highlights an opportunity for the enhancement of breakdown field strength through the inclusion of low-k, high-breakdown shells.

#### **7.1 Simulation of Hypothetical Core-Multishell Nanoparticle Architectures**

To capitalize on the opportunity mentioned above, QESIM is employed to simulate four sets of hypothetical core-multishell NPs. Each set consists of seven NP core-shell architectures (shown in Figure 7.1) for 6 different volume fractions between 2% and 10%, for a total of 30 data points, (six of which represent control cases that consist entirely of core material

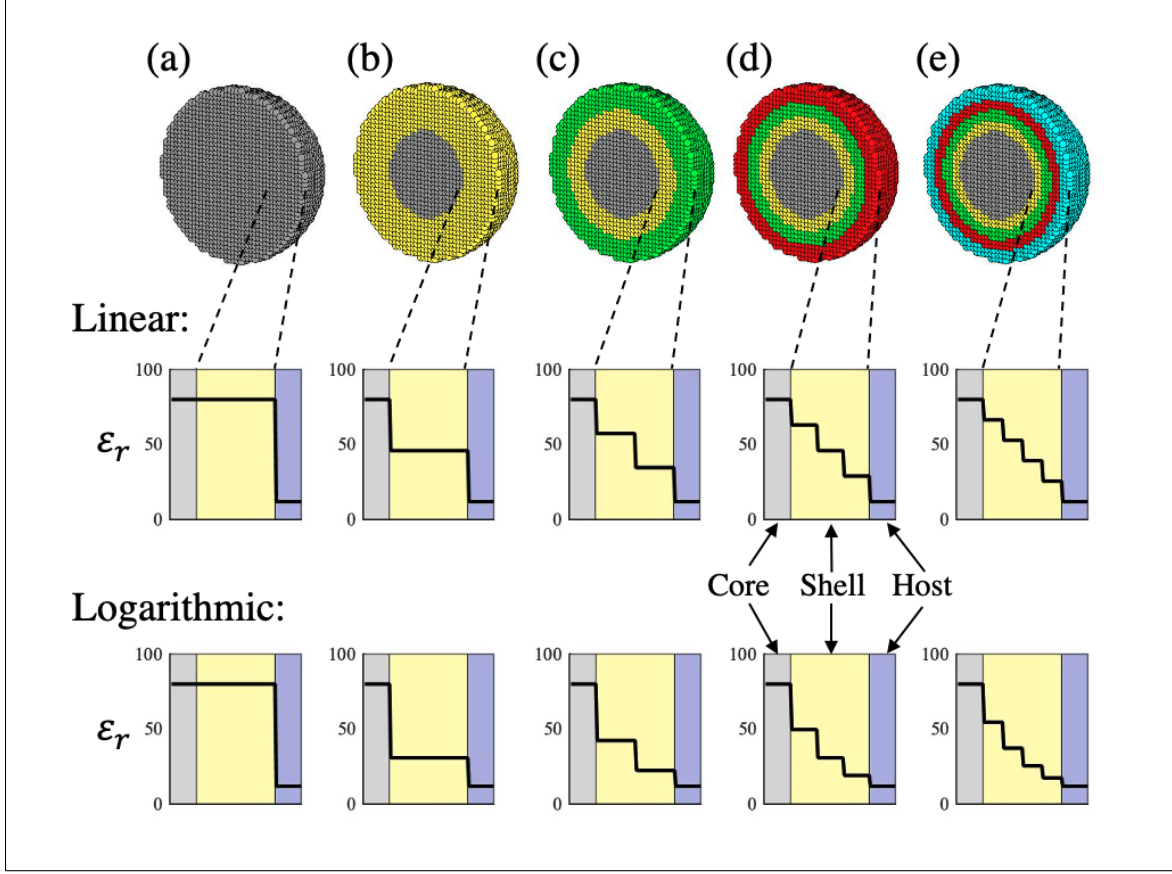


Figure 7.1: Illustration of simulated core-multishell architectures with linear and logarithmically-graded permittivity shells at a single volume fraction of 6% (for  $t_{shell} \approx 13nm$ ) for (a) no shells, (b) one shell, (c) two shells, (d) three shells, and (e) four shells.

immersed in the P(VDF-HFP) host). The control case with no shells shown in Figure 7.1 is accompanied by a second control case that is just pure host material.

Unlike in previous chapters, which emphasize the stochastic distribution of NPs in the simulated window, this chapter employs QESIM for a single NP centered in the simulated volume to obtain each datapoint. This is done to provide sufficient resolution for the voxel-representation of the intricate shell structures explored in this chapter. In addition to the core-shell structures, the permittivity of each shell is determined for two distinct categories. These categories are defined by the functions used to determine the permittivity in each shell, and include (1) NPs with linearly-graded shells, and (2) NPs with logarithmically-graded shells. In Figure 7.1, the linearly-graded shell architectures are shown in the upper

row of plots, while the logarithmically-graded shell architectures are shown in the lower row. Likewise, the breakdown strength of each material is determined based on the fundamental relationship between permittivity and breakdown strength that is discussed by [52]. Thus, the breakdown strength for each shell related to the permittivity of each shell as given by Equation 7.1.

$$E_{bd} = 22.8(\varepsilon_r)^{-0.64} \left[ \frac{MV}{cm} \right] \quad (7.1)$$

Finally, all of this is simulated for two distinct shell thicknesses ( $t_{shell}$ ), (1)  $t_{shell} \approx 6.5\text{nm}$ , and (2)  $t_{shell} \approx 13\text{nm}$ , with the latter shown in Figure 7.1. For each volume fraction, the total NP radius that includes both the core radius and shell thickness is fixed so that the volume fraction describes the percentage of the simulated window that is occupied by all voxels that represent non-host materials. For example, all cases with the largest volume fraction of 10% include a single NP with a diameter of 57.2nm in a simulated volume that is  $100\text{nm} \times 100\text{nm} \times 100\text{nm}$ . The resulting data set includes 120 individual geometries divided into four cases defined by the intersection of the two shell thickness and the two permittivity grading functions. It is hypothesized that of the four cases studied here, NPs with 13nm shell thickness and logarithmically-graded permittivity will lead to optimal energy storage characteristics, as it provides more gradual changes in permittivity nearest to the high electric field region in the host material adjacent of the NP.

## 7.2 Results

Simulating the engineered NP geometries described above, the internal electric fields were obtained and processed to approximate the effective permittivity, breakdown field strength, and maximum theoretical energy density using the methods described in Chapters 2, 3, and 4, respectively. Examining cross-sections of the internal electric field magnitudes shown in Figure 7.2, it is clear that the logarithmically-graded shell architecture is most effective in mitigating the buildup of high electric fields within the host material when compared

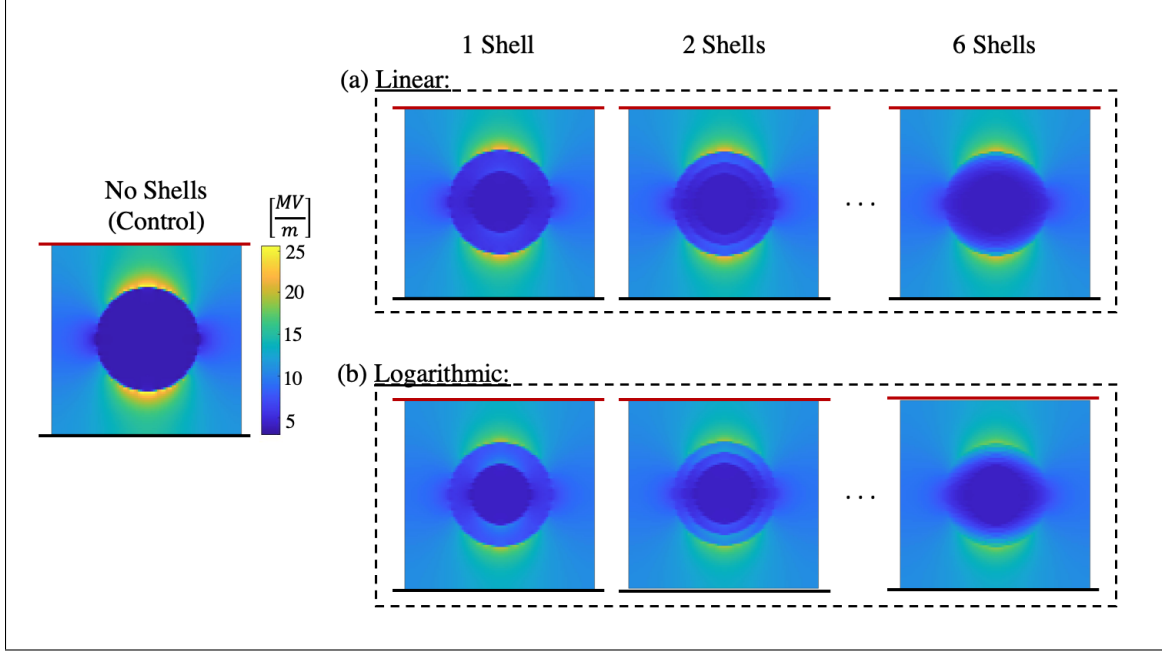


Figure 7.2: Cross-sections of internal electric field magnitudes (scaled to the colorbar shown) within simulated NP architectures depicting the re-distribution of electric fields into the NP shell structure for (a) linearly-graded and (b) logarithmically-graded shell permittivities.

to the linearly-graded shells. To illustrate the effects of higher shell count, the 6-shell logarithmically-graded case shown in Figure 7.2 exhibits a maximum electric field magnitude reduction of as much as 30% compared to the control case no shells. This illustrates the clear advantages of logarithmically-graded shell permittivity values when compared to linearly-graded shell permittivities.

### 7.2.1 Effective Permittivity

For the NP architectures simulated in this chapter, a reduction in effective permittivity is expected when compared to the control case. This reduction in effective permittivity is expected to be sufficiently small as compared to the square increase in breakdown strength so as to increase the maximum theoretical energy density of the core-multishell filler. When comparing the results in Figure 7.3 on shell thickness, it is clear that thicker shells lead to a slightly greater reduction in dielectric permittivity as expected. This is because a greater

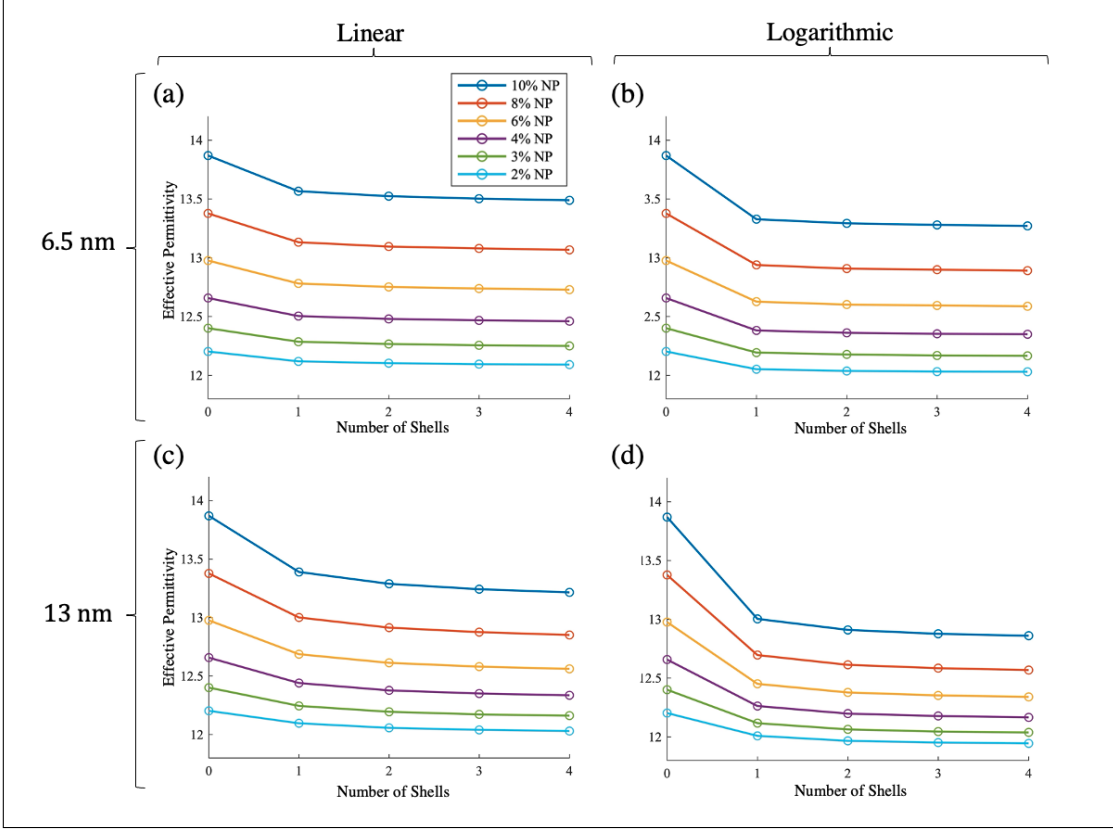


Figure 7.3: Effective composite permittivity of simulated core-multishell NP architectures with (a) linearly-graded shells with a total thickness of 6.5nm, (b) logarithmically-graded shells with a total thickness of 6.5nm, (c) linearly-graded shells with a total thickness of 13nm, and (d) logarithmically-graded shells with a total thickness of 13nm.

volume of high-k core material is displaced by the inclusion of a larger shell. Likewise, when comparing the results on permittivity grading, the logarithmically-graded permittivity case shows that the maximum reduction in effective permittivity is just under 8%.

### 7.2.2 Breakdown Field Strength

Using the breakdown path algorithm outlined in Chapter 3, the dielectric breakdown field strength was determined for each of the simulated core-multishell NP architectures. As expected, the use of multiple shells with graded permittivity is effective in enhancing the breakdown strength of the simulated geometries. As shown in Figure 7.4 the 30% reduction in maximum electric field magnitude translates to an increase in breakdown field strength

of just over 36% for composites with 4 shells, logarithmically-graded permittivity, and a volume fraction of 4%. The effective breakdown strength of this composite is over 17% greater than the breakdown strength of the pure host material. When comparing the results shown in Figure 7.4, the optimal case is identified as case (d) with a shell thickness of 13nm and logarithmically-graded permittivity. As depicted in Figure 7.2, this is due to the dispersion of electric fields at the interphase between filler and host, where thicker shells allow for greater dispersion. In addition, logarithmically-graded shell permittivity values ensure a smaller difference in permittivity between the outermost shell and the host material. As compared to the data presented in Chapter 4, the breakdown strength of the composites examined here is slightly higher because the breakdown strength of the host material was calculated using Equation 7.1, which provides an overestimate of the breakdown field strength of P(VDF-HFP). Acknowledging this slight optimism in the breakdown strength of the host material, the effective breakdown field strength values shown in the control cases in Figure 7.4 and in Figure 7.5 accurately match the properties reported in Chapter 4.

### 7.2.3 Maximum Theoretical Energy Density

Using the effective breakdown strength and composite permittivity of each sample shown in Figure 7.3 and Figure 7.4, the maximum theoretical energy density of each NP architecture is calculated using Equation 3.1 with the factor of practicality  $\zeta = 0.5$ . Again, it is important to note that the simulated energy densities reported in the zero-shell control cases in Figure 7.5 accurately match those reported in Chapter 4, making the control cases a valid baseline for comparison. Comparing the data for each of the four cases in Figure 7.5, the advantage of both thicker shells and logarithmic permittivity grading becomes clear. Specifically, Figure 7.5(d) shows an increase in energy density of 67.4% when compared to the 4% NP no-shell control case. This is an increase of 105% when compared to the 8% NP control case, and an increase of over 28.5% when compared to the pure host material.

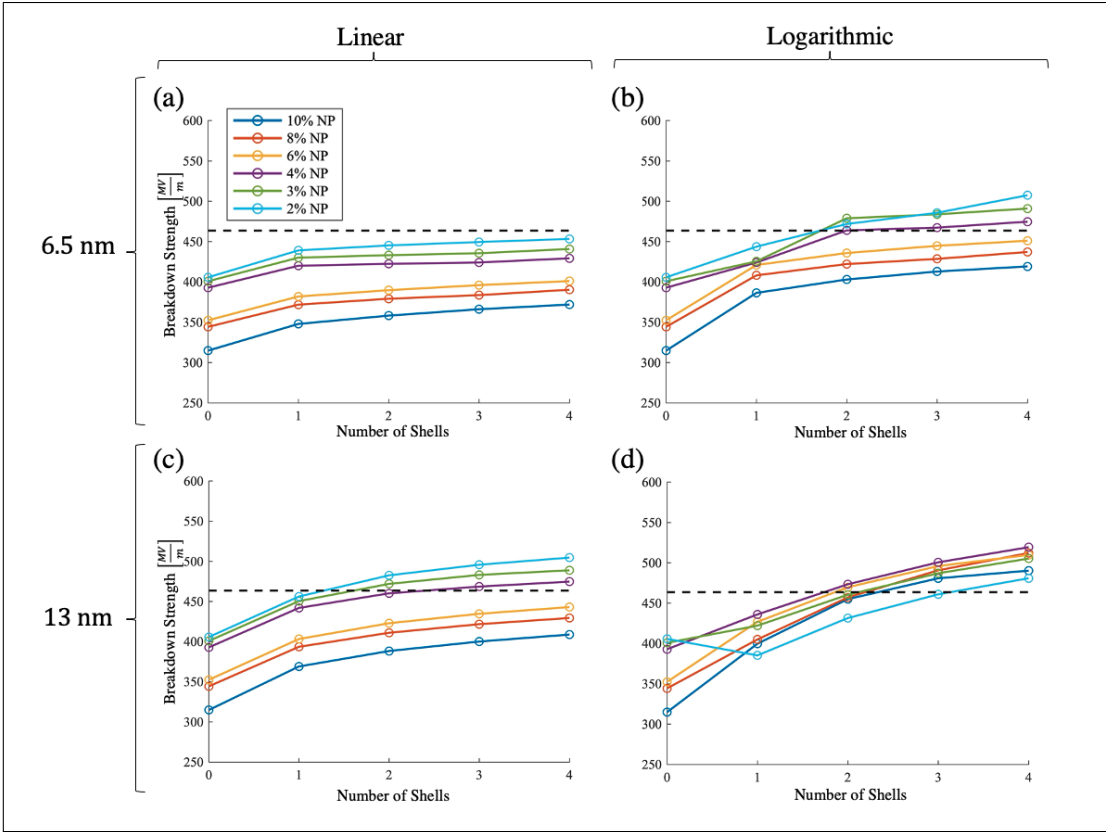


Figure 7.4: Effective dielectric breakdown field strength of simulated core-multishell NP architectures with (a) linearly-graded shells with a total thickness of 6.5nm, (b) logarithmically-graded shells with a total thickness of 6.5nm, (c) linearly-graded shells with a total thickness of 13nm, and (d) logarithmically-graded shells with a total thickness of 13nm.

It is worth noting that even with as few as two shells, at this thickness for logarithmically-graded shell permittivities, the energy density of almost every simulated structure exceeds the energy density of the pure host material and additional shells further enhance this energy density. That said, Figure 7.5 clearly illustrates the advantage of the 13 nm thick logarithmically-graded 4-shell NP architectures (at a volume fraction of 4% and 8%) over all other cases considered in this chapter.

### 7.3 Comparison to Hypothetical 2-Phase NP Composites

In Chapter 4, several hypothetical ceramic inclusion materials were studied in addition to  $\text{BaTiO}_3$ . To understand how core-multishell architectures impact the energy density of

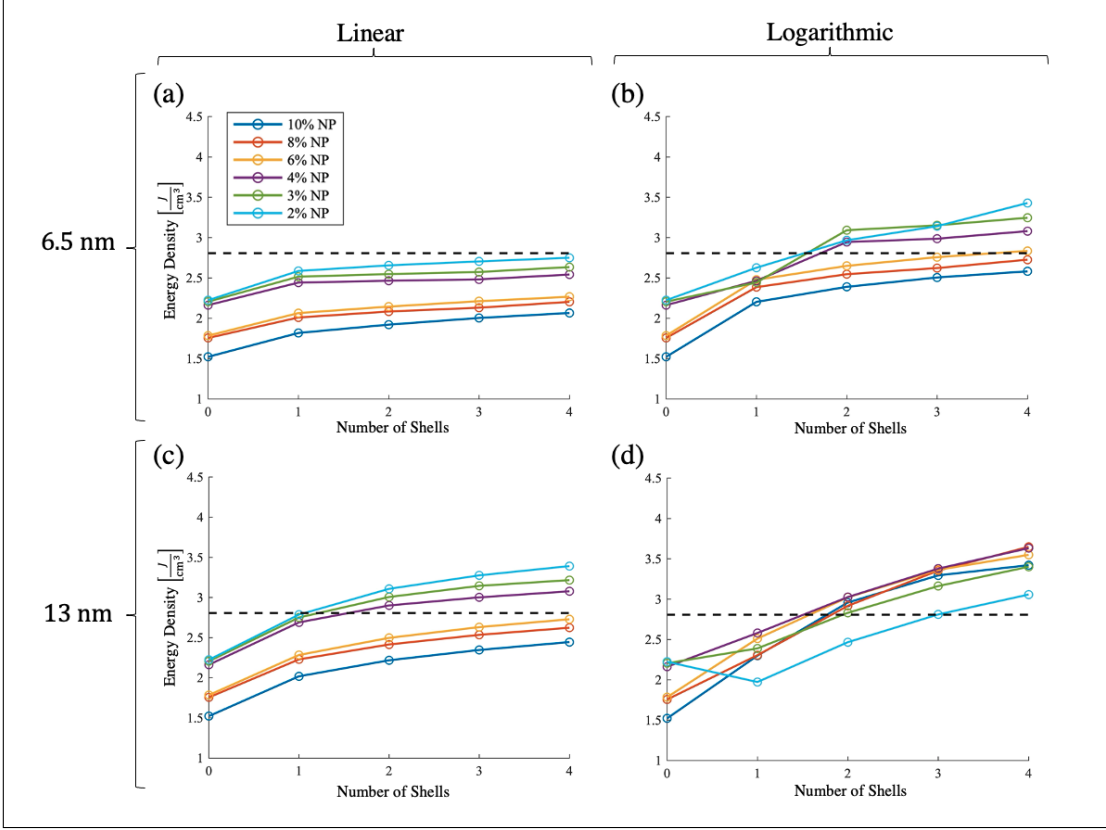


Figure 7.5: Maximum theoretical energy density of simulated core-multishell NP architectures with (a) linearly-graded shells with a total thickness of 6.5nm, (b) logarithmically-graded shells with a total thickness of 6.5nm, (c) linearly-graded shells with a total thickness of 6.5nm, and (d) logarithmically-graded shells with a total thickness of 6.5nm.

a broader range of composite materials, two additional cases were simulated with cores consisting of (1)  $\text{SrTiO}_3$  and (2)  $\text{SiO}_2$  with permittivities of 161.0 and 3.90, respectively. These materials were chosen to examine the impact of core permittivity on the overall energy density of core-multishell NP composites. In previous chapters,  $\text{SiO}_2$  NP inclusions have shown a clear advantage in terms of energy density due to the possible breakdown-enhancement that arises from low-k, high-breakdown-strength NP inclusions.

In Figure 7.6, the energy densities of core-multishell NP composites with  $\text{SiO}_2$ ,  $\text{BaTiO}_3$ , and  $\text{SrTiO}_3$  cores are shown. The total shell thickness  $t_{shell} = 13\text{nm}$  was constructed with logarithmically-graded shell permittivities. Figure 7.6(a) shows the highest energy density which marks an increase of over 47% compared to the pure host material. This also shows

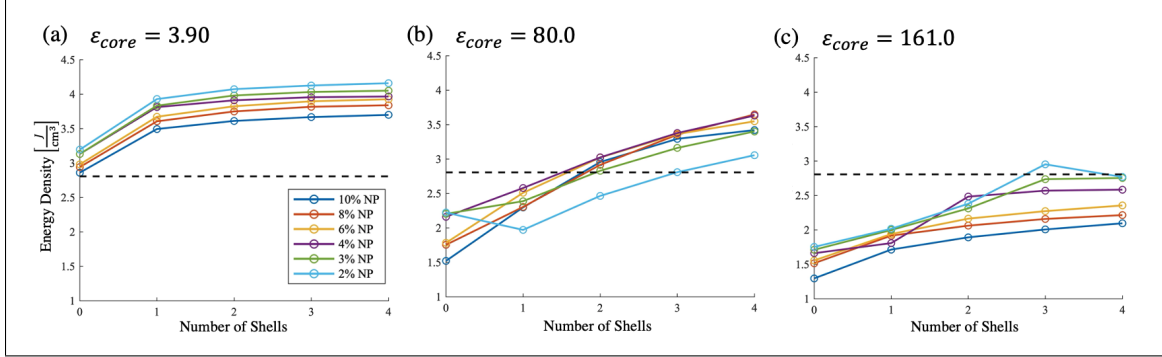


Figure 7.6: Maximum theoretical energy density of core-multishell composites with logarithmically-graded shell permittivities and shell thickness  $t_{shell} = 13\text{nm}$ .

a clear opportunity for experimentation as the energy density is increased by as much as 42% with the addition of a single shell with permittivity of 6.7, which is equal to that of  $\text{Si}_3\text{N}_4$  as reported in [52].

Interestingly, the high-k core case shown in Figure 7.6(c) shows a reduction in overall energy density when compared to low-k core cases, with a mere 7% energy density enhancement for 2% NP with 3 logarithmically-graded shells. This further supports the findings of previous chapters which indicate the possibility for energy density optimization through the use of low-k, high-breakdown-strength materials. The additional enhancement of energy density for low-k NP with engineered shell architectures can be explored by experimental fabrication of core-multishell NP with a  $\text{SiO}_2$  core and just a single shell consisting of  $\text{Si}_3\text{N}_4$ .

## 7.4 Summary & Conclusions

With the breakdown field strength of materials as a fundamental limiting factor of energy density within solid state energy storage materials, this chapter details a core-multishell approach for the mitigation of dielectric breakdown in NP composites. Using QESIM, data was generated on over 150 unique core-multi-shell architectures to identify possible energy density optimizations by the engineering of breakdown-enhancing NP filler (Figure 7.1). These simulated NP architectures are shown to effectively dissipate the high electric fields

Table 7.1: Permittivity of constituent materials for best-case core-multishell NP architecture with a BaTiO<sub>3</sub> core and a P(VDF-HFP) host with possible analogous real materials and their measured permittivities as reported in [52].

Vol% NP	Core	Shell 1	Shell 2	Shell 3	Shell 4	Host
4%, 8%	80.0	54.6	37.2	25.4	17.3	11.8
Real Materials:	<b>BaTiO<sub>3</sub></b>	TiO <sub>2</sub>	Pr <sub>2</sub> O <sub>3</sub>	La <sub>2</sub> O <sub>3</sub>	Ta <sub>2</sub> O <sub>5</sub>	<b>P(VDF-HFP)</b>
Measured $\varepsilon_r$ :	80.0	60.0	31.0	26.8	19.0	11.80

at the interphase between host and filler, thus reducing the maximum internal electric field by as much as 30% as illustrated in Figure 7.2. This translates to an increase in breakdown strength of just over 31% when compared to the zero-shell control case, and a 13% increase in breakdown strength when compared to the pure host material. The best-case for core-multishell NPs with BaTiO<sub>3</sub> cores exhibited an energy density that is 28.5% greater than the energy density of the pure host material, and this was achieved by the 13 nm 6-shell filler with logarithmically-graded permittivity at volume fractions of 4% and 8%. Likewise, this represents an increase in energy density of as much as 67.4% when compared to the 4% NP control case, and 105% when compared to the 8% NP control case. Furthermore, the best-case for core-multishell NPs with SiO<sub>2</sub> cores showed an energy density enhancement of over 47% compared to the pure host material while the higher permittivity SrTiO<sub>3</sub> cores showed a much smaller enhancement in energy density of just 7% compared to the pure host. The permittivities of the constituent materials for this case are given in Table 7.1 along with a corresponding set of materials that have been noted to exhibit permittivities approximately equal to those used in each shell [52]. In addition, the permittivities of the constituent materials for the SiO<sub>2</sub> core case are given in Table 7.2.

Based on Figure 7.6, it can be concluded that low-k cores are favorable over high-k cores. The results in Figure 7.6(c) indicate an opportunity for the experimental fabrication of core-shell composites featuring engineered NP consisting of a SiO<sub>2</sub> core and a single Si<sub>3</sub>N<sub>4</sub> shell, immersed in a P(VDF-HFP) host matrix. It is likely that further increases in the number of shells will provide additional enhancements to the breakdown strength,

Table 7.2: Permittivity of constituent materials for best-case core-multishell NP architecture with a  $\text{SiO}_2$  core and a P(VDF-HFP) host with possible analogous real materials and their measured permittivities as reported in [52].

Vol% NP	Core	Shell 1	Shell 2	Shell 3	Shell 4	Host
2%	3.90	4.87	6.07	7.58	9.46	11.8
Real Materials:	<b>SiO<sub>2</sub></b>	Si <sub>3</sub> N <sub>4</sub>	Si <sub>3</sub> N <sub>4</sub>	Si <sub>3</sub> N <sub>4</sub>	Al <sub>2</sub> O <sub>3</sub>	<b>P(VDF-HFP)</b>
Measured $\varepsilon_r$ :	3.90	6.30	6.70	7.10	8.50	11.8

but this appears to increase with diminishing returns. This work echos the suggestions of [46], and calls for further research into core-multishell NP architectures. Specifically, the study of gradient-permittivity core-shell NPs underpins an exigent opportunity for the enhancement of energy density in next-generation solid-state NP composite materials.

## CHAPTER 8

### CONCLUSIONS & FUTURE WORK

In total, this work has successfully leveraged QESIM to provide insight into the dielectric behavior and energy storage properties associated with a broad range of disordered NP composite material systems. Through the development and validation of QESIM, a number of notable observations have been documented which aim to guide the development of next-generation energy storage materials and capacitive dielectrics. The core components of the simulator employed in this work are documented in Chapters 2 and 3, and additional modifications and validations are carried out in subsequent chapters. Algorithms and analytical equations have been successfully implemented, derived, and validated to accurately approximate the core parameters of optimal energy storage materials (i.e. effective permittivity, breakdown field strength, and loss tangent). Using this array of tools, several strategies for parameter optimization in disordered NP composites have been identified based on a combination of simulated data and previously published measured data.

#### **8.1 Optimal Properties of Composites**

Towards the optimization of energy density in capacitive dielectric composite materials, Chapter 4 details a simulation experiment which aims to identify optimal parameter combinations based on realistic materials documented in [52]. The inverse relationship between dielectric permittivity and breakdown field strength is emphasized and quantified empirically in [52], leading to the simulation of four realistic 2-phase composite material combinations. The results of these hypothetical material simulations identify an important characteristic of NP composites, that is, the optimality of high-breakdown, low-permittivity filler over low-breakdown, high-permittivity filler material. This finding is unique in the literature where many works focus on enhancing dielectric permittivity despite the fact that it

only has a linear relationship to energy density as in Equation 8.1. The greater opportunity is to enhance breakdown field strength because of the squared relationship in Equation 8.1. (while breakdown strength exhibits a squared-relationship to energy density).

$$u_{max} = \frac{1}{2}\varepsilon_0\varepsilon_r E_{bd}^2 \quad (8.1)$$

Equation 8.1 identifies the core parameters that contribute to energy density in capacitive dielectrics as permittivity and breakdown field strength. Specifically, simulations carried out in Chapter 4 illustrate the idea that the inclusion of low-permittivity filler materials can in fact lead to higher energy density than high-k filler. The results of these simulations indicate the upper bound of energy density enhancement to be nearly an order of magnitude greater than the pure host material for low-k filler. This enhancement in maximum theoretical energy density is double that of the high-k filler material case. While this represents an optimistic upper bound on energy density associated with such composites, it highlights the superiority of low-k, high-breakdown dielectric fillers like  $\text{SiO}_2$  when compared to high-k, low-breakdown fillers like  $\text{SrTiO}_3$ .

## 8.2 Exploration of Metal-Insulator Composites

To expand the functionality of this simulator, a particular class of composites known as metal-insulator-composites (MIC) have been explored. These materials consist of a conductive metal filler immersed in an insulating dielectric host, and tend to exhibit highly-variable dielectric properties that depend heavily on the constituent materials. QESIM has been validated against MIC that include Cu or Al filler immersed in a non-ferroelectric PVC host material; however, the simulation of Au filler immersed in an  $\text{Al}_2\text{O}_3$  host and Ag filler immersed in an epoxy host show anomalous results. Interestingly, these composites containing metallic filler with a high work-function (e.g. Au and Ag) can achieve dielectric permittivity values that vastly exceed what can be achieved by QESIM using classical EM

models outlined prior to Chapter 6. To explore this discrepancy between the measured data reported in [22] and [21], Chapter 6 explores the concept of negative capacitance (NC) in-depth to provide a possible physical explanation for the extraordinarily high enhancement in dielectric permittivity found in the published experiments. The close correlation of the measured data reported in [21] and the QESIM data obtained using the NC model not only possibly explains the high effective permittivity, but it also highlights the potential for NC behavior to exist within epoxy and possibly other polymers as well.

### **8.3 Simulation of Engineered Core-Multishell Nanoparticles**

The dielectric breakdown of materials is a critical parameter for the enhancement of maximum theoretical energy density. When examining the distribution of internal electric fields within composites, a tendency for electric fields to build up in the low-k host material near high-k inclusions has been observed. This behavior is a major contributing factor to reductions in breakdown strength that have been documented in composites containing high-k dielectric or metallic inclusions. To address this, Chapter 7 employs QESIM for the simulation of engineered core-shell NPs with functionally-graded-permittivity shells. In particular, NPs with up to 4 different shells were simulated with permittivities ascending linearly and logarithmically from core to host. Of the four simulated cases, it was determined that a higher number of shells exhibiting logarithmically-graded permittivity achieved the greatest enhancement in energy density that led to a maximum increase in energy density of 28.5% when compared with the pure host material and as much as of 105% when compared with the zero-shell control case. The additional simulation of high-k and low-k core-multishell NP architectures has also provided further support for the claims in Chapter 4 of possible energy density enhancement using low-k NP inclusions as opposed to high-k NP inclusions.

It has been concluded that significant efforts should be made in the area of core-multishell NPs to enhance the breakdown strength and energy density of solid-state NP

composites beyond their current limits. While the fabrication of core-multishell filler with more than two shells may pose a notable challenge, this computational work has outlined the considerable advantages of such NP architectures. In addition, one particular core-shell architecture with a single  $\text{Si}_3\text{N}_4$  shell and a low-k  $\text{SiO}_2$  core has been noted to enhance energy density by more than 43% when compared to the pure P(VDF-HFP) host material in simulation.

#### 8.4 Future Work

To further explore possible optimizations to the energy storage characteristics of composites, several avenues have been considered for the future contributions leveraging QESIM. Along the lines of what has been discussed in previous chapters, one natural extension of this work is the continued development of QESIM and the optimization of simulation accuracy. This would consist of three distinct efforts. First, the employment of an adaptive grid would allow for the simulation of far more complex systems consisting of very large and very small features that could utilize the current computational resources of Georgia Tech's PACE HPC environment. Second, the development of a second-order, 27-point Laplace formulation would allow for enhanced accuracy when approximating the internal electric fields within a given region. Naturally, this would increase the computational load of simulations and would reduce the maximum system resolution; however, the use of the previously mentioned adaptive grid in conjunction with this higher-order approximation could be the basis for a powerful new simulation tool. Third, the implementation of additional physics-based algorithms to be used in the simulation of metal-insulator composites could shed light on how the work function ( $\Psi$ ) of metals impacts the built-in negative potential that arises in NC materials. As discussed in Chapter 6, the current understanding of NC effects in materials is in its relative infancy, and requires significant research efforts to uncover all that NC materials have to offer.

This work also motivates possible new experimental NP composite materials to be fab-

ricated and tested. First, the possibilities of polymer-based NC composites require additional study, and experimental laminate studies on the interphase between Ag and epoxy may clarify the possible NC behavior that was observed in [21] and discussed in Chapter 6. This experimental study could provide great insight into NC-induced internal voltage amplification. Second, the study of core-multishell NP with gradient permittivity presented in Chapter 7 showed significant enhancements in breakdown strength and energy density that were observed in simulation. To this end, the potential fabrication processes for core-multishell or core-gradient-shell NPs would extend the work in the previous chapter. Acknowledging the immense difficulty of core-multishell NP fabrication, additional approaches could be considered that utilize natural doping profiles that arise from thermal diffusion processes to approximate the logarithmic-graded conductivity shell architectures that exhibited the greatest increases in energy density. To this end, an additional simulation experiment must be carried out to quantify the impact of core-multishell NP with logarithmically-graded shell conductivities to determine whether or not such doping profiles would lead to enhancements in overall energy density as it does in the case of graded shell permittivity NP. Ultimately, this future work would extend the study of engineered core-multishell NP both computationally and experimentally and guide the design of next generation capacitive energy storage materials and devices.

# **Appendices**

## APPENDIX A

### DERIVATIONS

#### A.1 Derivation of 7-Point Laplace Electric Field Approximation

Before describing the mathematical derivation of the electric field approximation used in this simulator, it is important to clearly define the structure of the simulation space. This simulator relies on a uniform-cubic finite difference grid as illustrated in Figure A.1. Each cubic voxel (or cell) is equal in dimensions to all other voxels in the volume. This allows for some simplifications in the derivation that follows in this appendix, while also allowing facilitating the implementation of physics-based phenomenological algorithms like the dielectric breakdown path model discussed in Chapter 3.

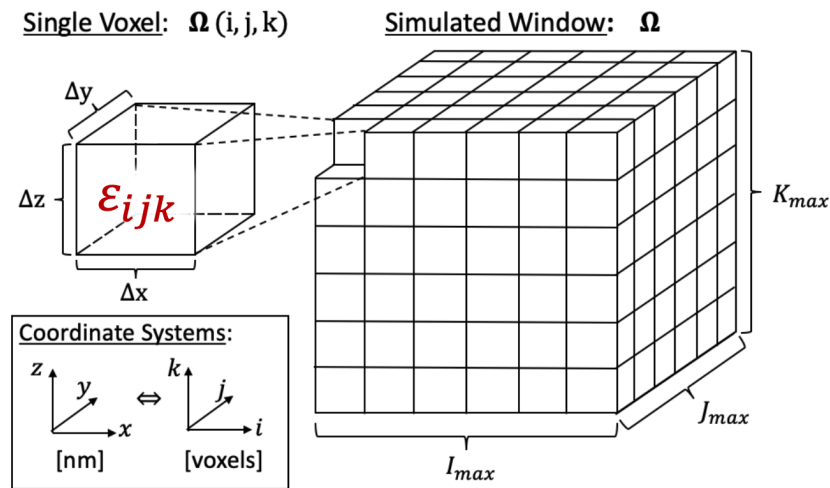


Figure A.1: Illustration of finite difference grid used to represent 3-D simulated window.

The basis for the electric field approximation that is derived in this appendix is the Laplace relationship given by Equation A.1.

$$\nabla \cdot \epsilon \nabla V = 0 \quad (\text{A.1})$$

From this equation, the electric fields can be approximated within a discrete volume as illustrated in Figure A.1 by extrapolating into three dimensions and using discrete integral approximations to obtain an expression that relates the properties and states of all voxels in the system with that of all other voxels in the system. Essentially, this expression must be converted into a system of equations that contains  $N$  equations and  $N$  unknowns where  $N$  is equal to the total number of voxels in the simulation window. To obtain the system of equations that describes the internal potentials for the given volume, it is first necessary to extrapolate this expression to 3-dimensions as given by Equation A.2.

$$\frac{\partial}{\partial x} \left[ \varepsilon_{ijk} \frac{\partial V_{ijk}}{\partial x} \right] + \frac{\partial}{\partial y} \left[ \varepsilon_{ijk} \frac{\partial V_{ijk}}{\partial y} \right] + \frac{\partial}{\partial z} \left[ \varepsilon_{ijk} \frac{\partial V_{ijk}}{\partial z} \right] = 0 \quad (\text{A.2})$$

Next, to handle the outermost integral, both sides of the expression are integrated in three dimensions as in Equation A.3.

$$\int_{x_{i-\frac{1}{2}}}^{x_{i+\frac{1}{2}}} \int_{y_{j-\frac{1}{2}}}^{y_{j+\frac{1}{2}}} \int_{z_{k-\frac{1}{2}}}^{z_{k+\frac{1}{2}}} \left[ \frac{\partial}{\partial x} \left[ \varepsilon_{ijk} \frac{\partial V_{ijk}}{\partial x} \right] + \frac{\partial}{\partial y} \left[ \varepsilon_{ijk} \frac{\partial V_{ijk}}{\partial y} \right] + \frac{\partial}{\partial z} \left[ \varepsilon_{ijk} \frac{\partial V_{ijk}}{\partial z} \right] \right] dz dy dx = 0 \quad (\text{A.3})$$

To simplify this, each term within the integral isolated by the additive property, and the resulting expression is given by Equation A.4

$$0 = \int_{x_{i-\frac{1}{2}}}^{x_{i+\frac{1}{2}}} \int_{y_{j-\frac{1}{2}}}^{y_{j+\frac{1}{2}}} \int_{z_{k-\frac{1}{2}}}^{z_{k+\frac{1}{2}}} \left[ \frac{\partial}{\partial x} \left[ \varepsilon_{ijk} \frac{\partial V_{ijk}}{\partial x} \right] \right] dz dy dx + \\ \int_{x_{i-\frac{1}{2}}}^{x_{i+\frac{1}{2}}} \int_{y_{j-\frac{1}{2}}}^{y_{j+\frac{1}{2}}} \int_{z_{k-\frac{1}{2}}}^{z_{k+\frac{1}{2}}} \left[ \frac{\partial}{\partial y} \left[ \varepsilon_{ijk} \frac{\partial V_{ijk}}{\partial y} \right] \right] dz dy dx + \\ \int_{x_{i-\frac{1}{2}}}^{x_{i+\frac{1}{2}}} \int_{y_{j-\frac{1}{2}}}^{y_{j+\frac{1}{2}}} \int_{z_{k-\frac{1}{2}}}^{z_{k+\frac{1}{2}}} \left[ \frac{\partial}{\partial z} \left[ \varepsilon_{ijk} \frac{\partial V_{ijk}}{\partial z} \right] \right] dz dy dx \quad (\text{A.4})$$

Each of the three terms in Equation A.4 can then be simplified by evaluating one integral

on its specified range and taking the partial derivative as in Equation A.5.

$$\begin{aligned}
& \int_{x_{i-\frac{1}{2}}}^{x_{i+\frac{1}{2}}} \int_{y_{j-\frac{1}{2}}}^{y_{j+\frac{1}{2}}} \int_{z_{k-\frac{1}{2}}}^{z_{k+\frac{1}{2}}} \left[ \frac{\partial}{\partial x} [f(x, y, z)] \right] dz dy dx \\
&= \int_{y_{j-\frac{1}{2}}}^{y_{j+\frac{1}{2}}} \int_{z_{k-\frac{1}{2}}}^{z_{k+\frac{1}{2}}} \left[ \left[ f(x_{i+\frac{1}{2}}, y, z) \right] - \left[ f(x_{i-\frac{1}{2}}, y, z) \right] \right] dz dy
\end{aligned} \tag{A.5}$$

Applying this to all three terms, the resulting expression is given by Equation A.6

$$\begin{aligned}
0 &= \int_{y_{j-\frac{1}{2}}}^{y_{j+\frac{1}{2}}} \int_{z_{k-\frac{1}{2}}}^{z_{k+\frac{1}{2}}} \left[ \left[ \varepsilon_{i+\frac{1}{2}jk} \frac{\partial V_{i+\frac{1}{2}jk}}{\partial x} \right] - \left[ \varepsilon_{i-\frac{1}{2}jk} \frac{\partial V_{i-\frac{1}{2}jk}}{\partial x} \right] \right] dz dy + \\
&\quad \int_{x_{i-\frac{1}{2}}}^{x_{i+\frac{1}{2}}} \int_{z_{k-\frac{1}{2}}}^{z_{k+\frac{1}{2}}} \left[ \left[ \varepsilon_{ij+\frac{1}{2}k} \frac{\partial V_{ij+\frac{1}{2}k}}{\partial y} \right] - \left[ \varepsilon_{ij-\frac{1}{2}k} \frac{\partial V_{ij-\frac{1}{2}k}}{\partial y} \right] \right] dz dx + \\
&\quad \int_{x_{i-\frac{1}{2}}}^{x_{i+\frac{1}{2}}} \int_{y_{j-\frac{1}{2}}}^{y_{j+\frac{1}{2}}} \left[ \left[ \varepsilon_{ijk+\frac{1}{2}} \frac{\partial V_{ijk+\frac{1}{2}}}{\partial z} \right] - \left[ \varepsilon_{ijk-\frac{1}{2}} \frac{\partial V_{ijk-\frac{1}{2}}}{\partial z} \right] \right] dy dx
\end{aligned} \tag{A.6}$$

To provide a discrete estimate of the voltage derivative in each term, a central difference approximation is used as in Equation A.7, and the resulting expression is Equation A.8.

$$\frac{\partial V_{i+\frac{1}{2}}}{\partial x} = \frac{V_{i+1} - V_i}{\Delta x} \tag{A.7}$$

$$\begin{aligned}
0 &= \int_{y_{j-\frac{1}{2}}}^{y_{j+\frac{1}{2}}} \int_{z_{k-\frac{1}{2}}}^{z_{k+\frac{1}{2}}} \left[ \left[ \varepsilon_{i+\frac{1}{2}jk} \frac{V_{i+1jk} - V_{ijk}}{\Delta x} \right] - \left[ \varepsilon_{i-\frac{1}{2}jk} \frac{V_{ijk} - V_{i-1jk}}{\Delta x} \right] \right] dz dy + \\
&\quad \int_{x_{i-\frac{1}{2}}}^{x_{i+\frac{1}{2}}} \int_{z_{k-\frac{1}{2}}}^{z_{k+\frac{1}{2}}} \left[ \left[ \varepsilon_{ij+\frac{1}{2}k} \frac{V_{ij+1k} - V_{ijk}}{\Delta y} \right] - \left[ \varepsilon_{ij-\frac{1}{2}k} \frac{V_{ijk} - V_{ij-1k}}{\Delta y} \right] \right] dz dx + \\
&\quad \int_{x_{i-\frac{1}{2}}}^{x_{i+\frac{1}{2}}} \int_{y_{j-\frac{1}{2}}}^{y_{j+\frac{1}{2}}} \left[ \left[ \varepsilon_{ijk+\frac{1}{2}} \frac{V_{ijk+1} - V_{ijk}}{\Delta z} \right] - \left[ \varepsilon_{ijk-\frac{1}{2}} \frac{V_{ijk} - V_{ijk-1}}{\Delta z} \right] \right] dy dx
\end{aligned} \tag{A.8}$$

Again, by the additive property these six terms are split into a total of 12 terms consisting of four terms to represent the contribution from voxels along each of the three dimensional

axes ( $\hat{x}$ ,  $\hat{y}$ ,  $\hat{z}$ ). The resulting expression is given by Equation A.9

$$\begin{aligned}
0 = & \left( \frac{1}{\Delta x} \right) \int_{y_{j-\frac{1}{2}}}^{y_{j+\frac{1}{2}}} \int_{z_{k-\frac{1}{2}}}^{z_{k+\frac{1}{2}}} [\varepsilon_{i+\frac{1}{2}jk} V_{i+1jk}] dz dy - \\
& \left( \frac{1}{\Delta x} \right) \int_{y_{j-\frac{1}{2}}}^{y_{j+\frac{1}{2}}} \int_{z_{k-\frac{1}{2}}}^{z_{k+\frac{1}{2}}} [\varepsilon_{i+\frac{1}{2}jk} V_{ijk}] dz dy - \\
& \left( \frac{1}{\Delta x} \right) \int_{y_{j-\frac{1}{2}}}^{y_{j+\frac{1}{2}}} \int_{z_{k-\frac{1}{2}}}^{z_{k+\frac{1}{2}}} [\varepsilon_{i-\frac{1}{2}jk} V_{ijk}] dz dy + \\
& \left( \frac{1}{\Delta x} \right) \int_{y_{j-\frac{1}{2}}}^{y_{j+\frac{1}{2}}} \int_{z_{k-\frac{1}{2}}}^{z_{k+\frac{1}{2}}} [\varepsilon_{i-\frac{1}{2}jk} V_{i-1jk}] dz dy + \\
& \left( \frac{1}{\Delta y} \right) \int_{x_{i-\frac{1}{2}}}^{x_{i+\frac{1}{2}}} \int_{z_{k-\frac{1}{2}}}^{z_{k+\frac{1}{2}}} [\varepsilon_{ij+\frac{1}{2}k} V_{ij+1k}] dz dx - \\
& \left( \frac{1}{\Delta y} \right) \int_{x_{i-\frac{1}{2}}}^{x_{i+\frac{1}{2}}} \int_{z_{k-\frac{1}{2}}}^{z_{k+\frac{1}{2}}} [\varepsilon_{ij+\frac{1}{2}k} V_{ijk}] dz dx - \\
& \left( \frac{1}{\Delta y} \right) \int_{x_{i-\frac{1}{2}}}^{x_{i+\frac{1}{2}}} \int_{z_{k-\frac{1}{2}}}^{z_{k+\frac{1}{2}}} [\varepsilon_{ij-\frac{1}{2}k} V_{ijk}] dz dx + \\
& \left( \frac{1}{\Delta y} \right) \int_{x_{i-\frac{1}{2}}}^{x_{i+\frac{1}{2}}} \int_{z_{k-\frac{1}{2}}}^{z_{k+\frac{1}{2}}} [\varepsilon_{ij-\frac{1}{2}k} V_{ij-1k}] dz dx + \\
& \left( \frac{1}{\Delta z} \right) \int_{x_{i-\frac{1}{2}}}^{x_{i+\frac{1}{2}}} \int_{y_{j-\frac{1}{2}}}^{y_{j+\frac{1}{2}}} [\varepsilon_{ijk+\frac{1}{2}} V_{ijk+1}] dy dx - \\
& \left( \frac{1}{\Delta z} \right) \int_{x_{i-\frac{1}{2}}}^{x_{i+\frac{1}{2}}} \int_{y_{j-\frac{1}{2}}}^{y_{j+\frac{1}{2}}} [\varepsilon_{ijk+\frac{1}{2}} V_{ijk}] dy dx - \\
& \left( \frac{1}{\Delta z} \right) \int_{x_{i-\frac{1}{2}}}^{x_{i+\frac{1}{2}}} \int_{y_{j-\frac{1}{2}}}^{y_{j+\frac{1}{2}}} [\varepsilon_{ijk-\frac{1}{2}} V_{ijk}] dy dx + \\
& \left( \frac{1}{\Delta z} \right) \int_{x_{i-\frac{1}{2}}}^{x_{i+\frac{1}{2}}} \int_{y_{j-\frac{1}{2}}}^{y_{j+\frac{1}{2}}} [\varepsilon_{ijk-\frac{1}{2}} V_{ijk-1}] dy dx
\end{aligned} \tag{A.9}$$

The current version of this simulator utilizes a 7-point approximation, and so the 7 unique voltage indices that are listed in Equation A.9 are extracted from the integrals as the discrete integral approximations from this point forward will act only on the dielectric permittivity

values in adjacent voxels. Pulling out the voltages, Equation A.10 is obtained.

$$\begin{aligned}
0 = & V_{i+1jk} \left( \frac{1}{\Delta x} \right) \int_{y_{j-\frac{1}{2}}}^{y_{j+\frac{1}{2}}} \int_{z_{k-\frac{1}{2}}}^{z_{k+\frac{1}{2}}} [\varepsilon_{i+\frac{1}{2}jk}] dz dy - \\
& V_{ijk} \left( \frac{1}{\Delta x} \right) \int_{y_{j-\frac{1}{2}}}^{y_{j+\frac{1}{2}}} \int_{z_{k-\frac{1}{2}}}^{z_{k+\frac{1}{2}}} [\varepsilon_{i+\frac{1}{2}jk}] dz dy - \\
& V_{ijk} \left( \frac{1}{\Delta x} \right) \int_{y_{j-\frac{1}{2}}}^{y_{j+\frac{1}{2}}} \int_{z_{k-\frac{1}{2}}}^{z_{k+\frac{1}{2}}} [\varepsilon_{i-\frac{1}{2}jk}] dz dy + \\
& V_{i-1jk} \left( \frac{1}{\Delta x} \right) \int_{y_{j-\frac{1}{2}}}^{y_{j+\frac{1}{2}}} \int_{z_{k-\frac{1}{2}}}^{z_{k+\frac{1}{2}}} [\varepsilon_{i-\frac{1}{2}jk}] dz dy + \\
& V_{ij+1k} \left( \frac{1}{\Delta y} \right) \int_{x_{i-\frac{1}{2}}}^{x_{i+\frac{1}{2}}} \int_{z_{k-\frac{1}{2}}}^{z_{k+\frac{1}{2}}} [\varepsilon_{ij+\frac{1}{2}k}] dz dx - \\
& V_{ijk} \left( \frac{1}{\Delta y} \right) \int_{x_{i-\frac{1}{2}}}^{x_{i+\frac{1}{2}}} \int_{z_{k-\frac{1}{2}}}^{z_{k+\frac{1}{2}}} [\varepsilon_{ij+\frac{1}{2}k}] dz dx - \\
& V_{ijk} \left( \frac{1}{\Delta y} \right) \int_{x_{i-\frac{1}{2}}}^{x_{i+\frac{1}{2}}} \int_{z_{k-\frac{1}{2}}}^{z_{k+\frac{1}{2}}} [\varepsilon_{ij-\frac{1}{2}k}] dz dx + \\
& V_{ij-1k} \left( \frac{1}{\Delta y} \right) \int_{x_{i-\frac{1}{2}}}^{x_{i+\frac{1}{2}}} \int_{z_{k-\frac{1}{2}}}^{z_{k+\frac{1}{2}}} [\varepsilon_{ij-\frac{1}{2}k}] dz dx + \\
& V_{ijk+1} \left( \frac{1}{\Delta z} \right) \int_{x_{i-\frac{1}{2}}}^{x_{i+\frac{1}{2}}} \int_{y_{j-\frac{1}{2}}}^{y_{j+\frac{1}{2}}} [\varepsilon_{ijk+\frac{1}{2}}] dy dx - \\
& V_{ijk} \left( \frac{1}{\Delta z} \right) \int_{x_{i-\frac{1}{2}}}^{x_{i+\frac{1}{2}}} \int_{y_{j-\frac{1}{2}}}^{y_{j+\frac{1}{2}}} [\varepsilon_{ijk+\frac{1}{2}}] dy dx - \\
& V_{ijk} \left( \frac{1}{\Delta z} \right) \int_{x_{i-\frac{1}{2}}}^{x_{i+\frac{1}{2}}} \int_{y_{j-\frac{1}{2}}}^{y_{j+\frac{1}{2}}} [\varepsilon_{ijk-\frac{1}{2}}] dy dx + \\
& V_{ijk-1} \left( \frac{1}{\Delta z} \right) \int_{x_{i-\frac{1}{2}}}^{x_{i+\frac{1}{2}}} \int_{y_{j-\frac{1}{2}}}^{y_{j+\frac{1}{2}}} [\varepsilon_{ijk-\frac{1}{2}}] dy dx
\end{aligned} \tag{A.10}$$

### A.1.1 Integral Approximation by Trapezoidal Quadrature

At this stage, it is clear that the voltage terms located at the centerpoint  $(i, j, k)$  may be combined, but for clarity this step will be handled after the discrete integration for each of the 12 terms. First, to provide further insight into how this translates to the simulated finite difference grid, Figure A.2 illustrates the relationship between the cells that represent

individual material regions (a) and the points that represent the indexed voltage potentials (b). Note that in Figure A.2(a), the subscripts denoting permittivity blocks follow a 3-bit binary scheme to express the specific voxel relative to the centerpoint. This notation will be used in subsequent steps as the integrals are expanded using the quadrature rule defined in Equation A.11.

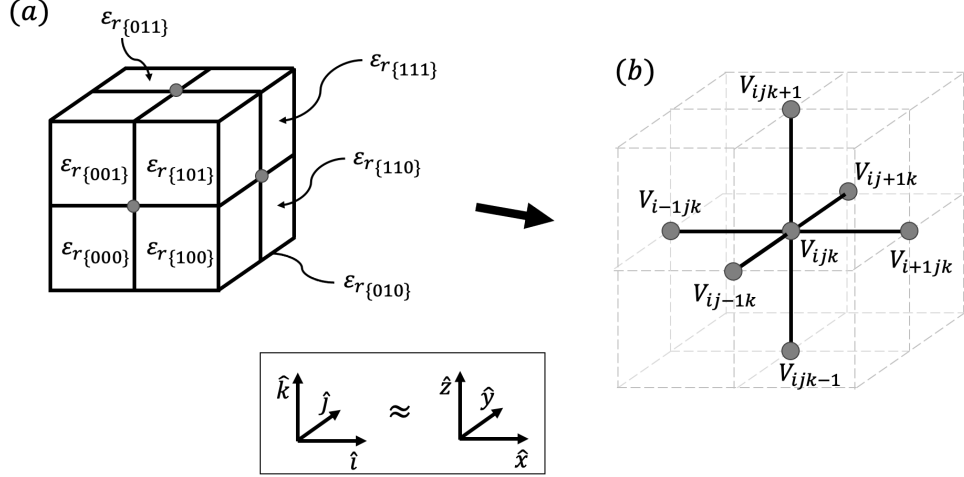


Figure A.2: illustration of localized spatial considerations for quadrature using uniform cubic finite difference grid showing (a) the dielectric permittivity cell grid and (b) the 7 indexed points that make up the localized scalar potential field.

---

**Important Note:** The discrete voxel represented by  $\varepsilon_{000}$  exists at the index of the central voxel at index  $(ijk)$ . This implies an offset of exactly  $\frac{1}{2}\Delta$  in each direction  $(i+\frac{1}{2}, j+\frac{1}{2}, k+\frac{1}{2})$  between the center of  $\varepsilon_{000}$  and the corresponding voltage point  $(V_{ijk})$ . Mathematically this must be considered, but it does not impact the outcome as this shift is uniform through  $\Omega$ .

---

To approximate the integrals for each of these terms, a trapezoidal quadrature rule is employed as given by the example shown in Equation A.11, which integrates the material properties (i.e. dielectric permittivity) in the  $\hat{y}$  and  $\hat{z}$  directions to the x-axis.

$$\int_{y_{j-\frac{1}{2}}}^{y_{j+\frac{1}{2}}} \int_{z_{k-\frac{1}{2}}}^{z_{k+\frac{1}{2}}} [\varepsilon_{i+\frac{1}{2}jk}] dz dy = \left( \frac{\Delta z \Delta y}{4} \right) (\varepsilon_{r[100]} + \varepsilon_{r[110]} + \varepsilon_{r[110]} + \varepsilon_{r[111]}) \quad (\text{A.11})$$

Carrying out this method of discrete integration on each of the terms listed in Equation A.10,

the result is given by Equation A.12.

$$\begin{aligned}
0 = & V_{i+1jk} \left( \frac{\Delta z \Delta y}{4 \Delta x} \right) \left( \varepsilon_{r[100]} + \varepsilon_{r[110]} + \varepsilon_{r[101]} + \varepsilon_{r[111]} \right) \\
& V_{ijk} \left( \frac{\Delta z \Delta y}{4 \Delta x} \right) \left( \varepsilon_{r[100]} + \varepsilon_{r[110]} + \varepsilon_{r[101]} + \varepsilon_{r[111]} \right) - \\
& V_{ijk} \left( \frac{\Delta z \Delta y}{4 \Delta x} \right) \left( \varepsilon_{r[000]} + \varepsilon_{r[010]} + \varepsilon_{r[001]} + \varepsilon_{r[011]} \right) + \\
& V_{i-1jk} \left( \frac{\Delta z \Delta y}{4 \Delta x} \right) \left( \varepsilon_{r[000]} + \varepsilon_{r[010]} + \varepsilon_{r[001]} + \varepsilon_{r[011]} \right) + \\
& V_{ij+1k} \left( \frac{\Delta z \Delta x}{4 \Delta y} \right) \left( \varepsilon_{r[010]} + \varepsilon_{r[110]} + \varepsilon_{r[011]} + \varepsilon_{r[111]} \right) - \\
& V_{ijk} \left( \frac{\Delta z \Delta x}{4 \Delta y} \right) \left( \varepsilon_{r[010]} + \varepsilon_{r[110]} + \varepsilon_{r[011]} + \varepsilon_{r[111]} \right) - \\
& V_{ijk} \left( \frac{\Delta z \Delta x}{4 \Delta y} \right) \left( \varepsilon_{r[000]} + \varepsilon_{r[100]} + \varepsilon_{r[001]} + \varepsilon_{r[101]} \right) + \\
& V_{ij-1k} \left( \frac{\Delta z \Delta x}{4 \Delta y} \right) \left( \varepsilon_{r[000]} + \varepsilon_{r[100]} + \varepsilon_{r[001]} + \varepsilon_{r[101]} \right) + \\
& V_{ijk+1} \left( \frac{\Delta y \Delta x}{4 \Delta z} \right) \left( \varepsilon_{r[001]} + \varepsilon_{r[011]} + \varepsilon_{r[101]} + \varepsilon_{r[111]} \right) - \\
& V_{ijk} \left( \frac{\Delta y \Delta x}{4 \Delta z} \right) \left( \varepsilon_{r[001]} + \varepsilon_{r[011]} + \varepsilon_{r[101]} + \varepsilon_{r[111]} \right) - \\
& V_{ijk} \left( \frac{\Delta y \Delta x}{4 \Delta z} \right) \left( \varepsilon_{r[000]} + \varepsilon_{r[010]} + \varepsilon_{r[100]} + \varepsilon_{r[110]} \right) + \\
& V_{ijk-1} \left( \frac{\Delta y \Delta x}{4 \Delta z} \right) \left( \varepsilon_{r[000]} + \varepsilon_{r[010]} + \varepsilon_{r[100]} + \varepsilon_{r[110]} \right)
\end{aligned} \tag{A.12}$$

After combining like terms, the expression takes the form of Equation A.13.

$$\begin{aligned}
0 = & V_{i+1jk} \left( \frac{\Delta z \Delta y}{4 \Delta x} \right) (\varepsilon_{r[100]} + \varepsilon_{r[110]} + \varepsilon_{r[101]} + \varepsilon_{r[111]}) + \\
& V_{i-1jk} \left( \frac{\Delta z \Delta y}{4 \Delta x} \right) (\varepsilon_{r[000]} + \varepsilon_{r[010]} + \varepsilon_{r[001]} + \varepsilon_{r[011]}) + \\
& V_{ij+1k} \left( \frac{\Delta z \Delta x}{4 \Delta y} \right) (\varepsilon_{r[010]} + \varepsilon_{r[110]} + \varepsilon_{r[011]} + \varepsilon_{r[111]}) + \\
& V_{ij-1k} \left( \frac{\Delta z \Delta x}{4 \Delta y} \right) (\varepsilon_{r[000]} + \varepsilon_{r[100]} + \varepsilon_{r[001]} + \varepsilon_{r[101]}) + \\
& V_{ijk+1} \left( \frac{\Delta y \Delta x}{4 \Delta z} \right) (\varepsilon_{r[001]} + \varepsilon_{r[011]} + \varepsilon_{r[101]} + \varepsilon_{r[111]}) + \\
& V_{ijk-1} \left( \frac{\Delta y \Delta x}{4 \Delta z} \right) (\varepsilon_{r[000]} + \varepsilon_{r[010]} + \varepsilon_{r[100]} + \varepsilon_{r[110]}) - \\
& V_{ijk} \left( \left( \frac{\Delta z \Delta y}{4 \Delta x} \right) (\varepsilon_{r[100]} + \varepsilon_{r[110]} + \varepsilon_{r[101]} + \varepsilon_{r[111]}) + \right. \\
& \quad \left( \frac{\Delta z \Delta y}{4 \Delta x} \right) (\varepsilon_{r[000]} + \varepsilon_{r[001]} + \varepsilon_{r[010]} + \varepsilon_{r[011]}) + \\
& \quad \left( \frac{\Delta z \Delta x}{4 \Delta y} \right) (\varepsilon_{r[010]} + \varepsilon_{r[110]} + \varepsilon_{r[011]} + \varepsilon_{r[111]}) + \\
& \quad \left( \frac{\Delta z \Delta x}{4 \Delta y} \right) (\varepsilon_{r[000]} + \varepsilon_{r[100]} + \varepsilon_{r[001]} + \varepsilon_{r[101]}) + \\
& \quad \left( \frac{\Delta y \Delta x}{4 \Delta z} \right) (\varepsilon_{r[001]} + \varepsilon_{r[011]} + \varepsilon_{r[101]} + \varepsilon_{r[111]}) + \\
& \quad \left. \left( \frac{\Delta y \Delta x}{4 \Delta z} \right) (\varepsilon_{r[000]} + \varepsilon_{r[010]} + \varepsilon_{r[100]} + \varepsilon_{r[110]}) \right) \tag{A.13}
\end{aligned}$$

Which simplifies to Equation A.14, and defines all non-zero contributions to the scalar

potential at a given point  $(ijk)$  in the simulated space.

$$\begin{aligned}
0 = & V_{i+1jk} \left( \frac{\Delta z \Delta y}{4 \Delta x} \right) \left( \varepsilon_{r_{[100]}} + \varepsilon_{r_{[101]}} + \varepsilon_{r_{[110]}} + \varepsilon_{r_{[111]}} \right) + \\
& V_{i-1jk} \left( \frac{\Delta z \Delta y}{4 \Delta x} \right) \left( \varepsilon_{r_{[000]}} + \varepsilon_{r_{[010]}} + \varepsilon_{r_{[001]}} + \varepsilon_{r_{[011]}} \right) + \\
& V_{ij+1k} \left( \frac{\Delta z \Delta x}{4 \Delta y} \right) \left( \varepsilon_{r_{[010]}} + \varepsilon_{r_{[110]}} + \varepsilon_{r_{[011]}} + \varepsilon_{r_{[111]}} \right) + \\
& V_{ij-1k} \left( \frac{\Delta z \Delta x}{4 \Delta y} \right) \left( \varepsilon_{r_{[000]}} + \varepsilon_{r_{[100]}} + \varepsilon_{r_{[001]}} + \varepsilon_{r_{[101]}} \right) + \\
& V_{ijk+1} \left( \frac{\Delta y \Delta x}{4 \Delta z} \right) \left( \varepsilon_{r_{[001]}} + \varepsilon_{r_{[011]}} + \varepsilon_{r_{[101]}} + \varepsilon_{r_{[111]}} \right) + \\
& V_{ijk-1} \left( \frac{\Delta y \Delta x}{4 \Delta z} \right) \left( \varepsilon_{r_{[000]}} + \varepsilon_{r_{[010]}} + \varepsilon_{r_{[100]}} + \varepsilon_{r_{[110]}} \right) + \\
& V_{ijk} \left( - \left( \frac{\Delta z \Delta y}{4 \Delta x} + \frac{\Delta z \Delta x}{4 \Delta y} + \frac{\Delta y \Delta x}{4 \Delta z} \right) \times \right. \\
& \left. \left( \varepsilon_{r_{[000]}} + \varepsilon_{r_{[010]}} + \varepsilon_{r_{[001]}} + \varepsilon_{r_{[011]}} + \varepsilon_{r_{[100]}} + \varepsilon_{r_{[110]}} + \varepsilon_{r_{[101]}} + \varepsilon_{r_{[111]}} \right) \right)
\end{aligned} \tag{A.14}$$

To use this formalism for the approximation of scalar potential at each point within the simulated space, the expression given by Equation A.14 is expanded to a vectorized form given by Equation A.15 which consists of vectors and matrices that represent all  $N$  cells in the simulated space.

$$\mathbf{A}v = b \quad \Rightarrow \quad v = \mathbf{A}^{-1}b \tag{A.15}$$

The expression given in Equation A.15 describes the vectorized form of the solution derived here, where  $v$  is a  $1 \times N$  vector representing the scalar potential at each point within the simulated space,  $b$  is a  $1 \times N$  boundary vector representing the applied scalar potential at the Dirichlet boundaries, and  $\mathbf{A}$  represents an  $N \times N$  sparse transformation matrix that contains exactly seven non-zero components in each row as defined by the coefficients in Equation A.14. To represent each voxel in the simulated space in a 1-D vector, each voxel is assigned a single-dimensional index, for which the 3-D indexing scheme  $(ijk)$  is flattened to a singular value so that the index  $(ijk)$  is represented by a single integer  $I$  that is

constrained by  $0 < I \leq N$ . The nonzero element along the central diagonal of the transformation matrix  $\mathbf{A}$  at row  $I$  is represented as  $\mathbf{A}_{ijk}^I$ . For simplicity, the subscript remains in 3-D indexing notation, but in practice a simple conversion must be used to obtain the column index for off-diagonal non-zero elements (similarly represented as  $\mathbf{A}_{i\pm 1jk}^I$ ,  $\mathbf{A}_{ij\pm 1k}^I$ , and  $\mathbf{A}_{ijk\pm 1}^I$ ). For any given row that corresponds to a voxel within the bulk of the simulated space (i.e. not in contact with an electrode boundary), the nonzero elements in each row of the  $\mathbf{A}$  matrix are given by Equation A.16.

$$\begin{aligned}
\mathbf{A}_{ijk}^I &= - \left( \frac{\Delta z \Delta y}{4 \Delta x} + \frac{\Delta z \Delta x}{4 \Delta y} + \frac{\Delta y \Delta x}{4 \Delta z} \right) \times \\
&\quad \left( \varepsilon_{r[000]} + \varepsilon_{r[010]} + \varepsilon_{r[001]} + \varepsilon_{r[011]} + \varepsilon_{r[100]} + \varepsilon_{r[110]} + \varepsilon_{r[101]} + \varepsilon_{r[111]} \right) \\
\mathbf{A}_{i+1jk}^I &= \left( \frac{\Delta z \Delta y}{4 \Delta x} \right) \left( \varepsilon_{r[100]} + \varepsilon_{r[101]} + \varepsilon_{r[110]} + \varepsilon_{r[111]} \right) \\
\mathbf{A}_{i-1jk}^I &= \left( \frac{\Delta z \Delta y}{4 \Delta x} \right) \left( \varepsilon_{r[000]} + \varepsilon_{r[010]} + \varepsilon_{r[001]} + \varepsilon_{r[011]} \right) \\
\mathbf{A}_{ij+1k}^I &= \left( \frac{\Delta z \Delta x}{4 \Delta y} \right) \left( \varepsilon_{r[010]} + \varepsilon_{r[110]} + \varepsilon_{r[011]} + \varepsilon_{r[111]} \right) \\
\mathbf{A}_{ij-1k}^I &= \left( \frac{\Delta z \Delta x}{4 \Delta y} \right) \left( \varepsilon_{r[000]} + \varepsilon_{r[100]} + \varepsilon_{r[001]} + \varepsilon_{r[101]} \right) \\
\mathbf{A}_{ijk+1}^I &= \left( \frac{\Delta y \Delta x}{4 \Delta z} \right) \left( \varepsilon_{r[001]} + \varepsilon_{r[011]} + \varepsilon_{r[101]} + \varepsilon_{r[111]} \right) \\
\mathbf{A}_{ijk-1}^I &= \left( \frac{\Delta y \Delta x}{4 \Delta z} \right) \left( \varepsilon_{r[000]} + \varepsilon_{r[010]} + \varepsilon_{r[100]} + \varepsilon_{r[110]} \right)
\end{aligned} \tag{A.16}$$

Finally, the Dirichlet electrode boundary conditions at the upper and lower bounds in the  $\hat{z}$  direction are defined such that only a single nonzero element exists in those corresponding rows of the  $\mathbf{A}$  matrix as given by Equation A.17.

$$\mathbf{A}_{ijk}^I = 1 \tag{A.17}$$

Combined with the boundary vector  $b$ , the boundary-adjacent voxels are defined in the  $\mathbf{A}$  matrix to enforce  $v_I = b_I$  at the electrodes, thus ensuring that the voltage approximated by Equation A.15 is equal to the voltage applied at the Dirichlet electrode boundaries.

## A.2 Derivation of Discrete Loss Tangent Approximation

The calculation of loss tangent in this model is given by Equation A.18.

$$\tan(\delta) = \frac{\varepsilon''}{\varepsilon'} \quad (\text{A.18})$$

Where  $\varepsilon'$  and  $\varepsilon''$  are the real and imaginary parts of the complex permittivity respectively.  $\omega$  is the frequency and  $\sigma_{eff}$  is the effective conductivity of the given composite. The complex permittivity is described by Equation A.19.

$$\begin{aligned} \varepsilon_{eff}^* &= \varepsilon' - j\varepsilon'' \\ &= \varepsilon_r - j \left( \frac{\sigma_{eff}}{\omega \varepsilon_0} \right) \end{aligned} \quad (\text{A.19})$$

$$\tan(\delta) = \frac{\sigma_{eff}}{\omega \varepsilon_0 \varepsilon_r} \quad (\text{A.20})$$

Where the  $\tan(\delta)$  depends directly on  $\sigma_{eff}$ . Thus, in order to calculate the loss tangent, it is first necessary to compute  $\sigma_{eff}$ . The effective conductivity describes the conductivity of the entire simulated device. In this model, the simulated volume is uniformly cubic and voxelated, and so the conductivity of a voxel cell at index  $(i, j, k)$  is included as  $\sigma_{ijk}$ . QESIM takes both  $\sigma_{ijk}$  and  $\varepsilon_{ijk}$  at all points within the simulated volume as inputs and approximates complex 3-D electric field at each point in the volume. With this, it is possible to determine  $\sigma_{eff}$  for the simulated volume using Ohm's Law. This is done by calculating the total power ( $P_{tot}$ ) dissipated in the device from the power dissipated in each voxel ( $P_{ijk}$ ), then using this total power to determine the effective conductivity of the entire simulated window. This effective conductivity is then used to compute the loss tangent of the simulated device. First,  $P_{ijk}$  for a voxel of dimensions  $\Delta x, \Delta y$ , and  $\Delta z$  is given by Equation A.26

$$P_{ijk} = \Re\{V_{ijk} I_{ijk}^*\} \quad (\text{A.21})$$

Where  $V_{ijk}$  and  $I_{ijk}^*$  represent the RMS values for voltage and current at index  $(i, j, k)$ , respectively. These two quantities are given by Equation A.27 and Equation A.28.

$$I_{ijk}^* = \left| \vec{E}_{ijk} \right|^* (\sigma_{ijk}) \Delta x \Delta y \quad (\text{A.22})$$

$$V_{ijk} = \left| \vec{E}_{ijk} \right| \Delta z \quad (\text{A.23})$$

And  $P_{tot}$  is therefore given by the sum of  $P_{ijk}$  dissipated within each voxel in the simulated space ( $\Omega$ ) as given by Equation A.24.

$$\begin{aligned} P_{tot} &= \sum_{\forall i,j,k}^{\in \Omega} P_{ijk} \\ &= \sum_{\forall i,j,k}^{\in \Omega} \Re\{V_{ijk} I_{ijk}^*\} \end{aligned} \quad (\text{A.24})$$

Thus, it is clear that the total power dissipated in the entire simulated volume is given by Equation A.25.

$$\begin{aligned} P_{tot} &= \sum_{\forall i,j,k}^{\in \Omega} \left[ \left| \vec{E}_{ijk} \right|^* \left| \vec{E}_{ijk} \right| (\sigma_{ijk}) \right] \Delta x \Delta y \Delta z \\ &= \sum_{\forall i,j,k}^{\in \Omega} \left[ \left| \vec{E}_{ijk} \right|^2 (\sigma_{ijk}) \right] \Delta x \Delta y \Delta z \end{aligned} \quad (\text{A.25})$$

Similarly,  $P_{tot}$  can be calculated using the applied electric field ( $E_{app}$ ), the effective conductivity ( $\sigma_{eff}$ ), and the dimensions of the entire simulated space ( $X, Y, Z$ ) by expanding Equation A.26.

$$P_{tot} = \Re\{V_{app} I_{app}^*\} \quad (\text{A.26})$$

Where  $V_{app}$  and  $I_{app}^*$  represent the applied voltage and current, respectively. These two quantities are given by Equation A.27 and Equation A.28.

$$I_{app}^* = \left| \vec{E}_{app} \right|^* (\sigma_{eff}) XY \quad (\text{A.27})$$

$$V_{app} = \left| \vec{E}_{app} \right| Z \quad (\text{A.28})$$

The total power is therefore also given by Equation A.29.

$$P_{tot} = \left| \vec{E}_{app} \right|^2 (\sigma_{eff}) XYZ \quad (\text{A.29})$$

Where  $X$ ,  $Y$ , and  $Z$  are related to  $\Delta x$ ,  $\Delta y$ , and  $\Delta z$  by Equation A.30.

$$\begin{aligned} X &= I_{max} \Delta x \\ Y &= J_{max} \Delta y \\ Z &= K_{max} \Delta z \end{aligned} \quad (\text{A.30})$$

And  $I_{max}$ ,  $J_{max}$ , and  $K_{max}$  are dimensions of the simulated window in units of voxels. Setting Equation A.29 equal to Equation A.25 yields Equation A.31, which explicitly describes the discrete approximation of  $\sigma_{eff}$ .

$$\begin{aligned} \left| \vec{E}_{app} \right|^2 (\sigma_{eff}) XYZ &= \sum_{\forall i,j,k}^{\infty} \left[ \left| \vec{E}_{ijk} \right|^2 (\sigma_{ijk}) \right] \Delta x \Delta y \Delta z \\ \sigma_{eff} &= \left( \frac{\sum_{\forall i,j,k}^{\infty} \left[ \left| \vec{E}_{ijk} \right|^2 (\sigma_{ijk}) \right]}{\left| \vec{E}_{app} \right|^2 I_{max} J_{max} K_{max}} \right) \end{aligned} \quad (\text{A.31})$$

Finally, combining Equation A.31 with Equation A.20, the loss tangent is given by Equation A.32.

$$\tan(\delta) = \frac{\sum_{\forall i,j,k}^{\in \Omega} \left[ \left| \vec{E}_{ijk} \right|^2 (\sigma_{ijk}) \right]}{\left| \vec{E}_{app} \right|^2 I_{max} J_{max} K_{max} (\omega \varepsilon_0 \varepsilon_r)} \quad (\text{A.32})$$

It is important to note that using this approach, large error can arise due to computational underflow and overflow in the multiplication of the electric field's squared magnitude and the conductivity as in Equation A.32. Attempts to mitigate this error have been met with significant increases in computation time when simulating composites that contain both conductive and insulating materials (e.g.  $\sigma \approx 10^{-8}$  and  $\sigma \approx 10^7$ ). The effects of overflow and underflow lead to small error in the complex electric field which is amplified in the calculation of effective conductivity. To avoid this, the loss tangent is computed using only the voxels that describe host material regions, and it is assumed that the conducting voxels in the simulated are ideal conductors (i.e. their internal electric fields are assumed to be zero).

### A.3 Derivation of Analytical Impedance Model for 2-Phase Laminates

The analytical model discussed in this work is based on the impedance characteristics of the model pictured in Figure A.3. A set of equations is derived which utilizes the physical properties (conductivity  $\sigma_i$  and permittivity  $\varepsilon_i$ ) of two constituent materials to calculate the lumped impedance ( $Z_s = Z_1 + Z_2$ ) and to ultimately determine the voltage across each layer ( $V_1, V_2$ ). This will allow for the approximation of effective permittivity and total loss characteristics. Additionally, to facilitate the formation of design equations, the thickness of each constituent material is represented by the variables  $d_1$  and  $d_2$ , where  $d_s$  is the total device thickness as pictured in Figure A.3(a). The thickness is varied to shed light on the possible voltage amplification effect that can occur when an NC layer exhibits a specific ratio of complex permittivity and relative thickness compared to the adjacent dielectric layer. It is also worth noting that this analytical model is generalized to represent laminate structures with  $N$  layers where the subscript  $i$  corresponds to the  $i^{th}$  layer in the laminate structure.

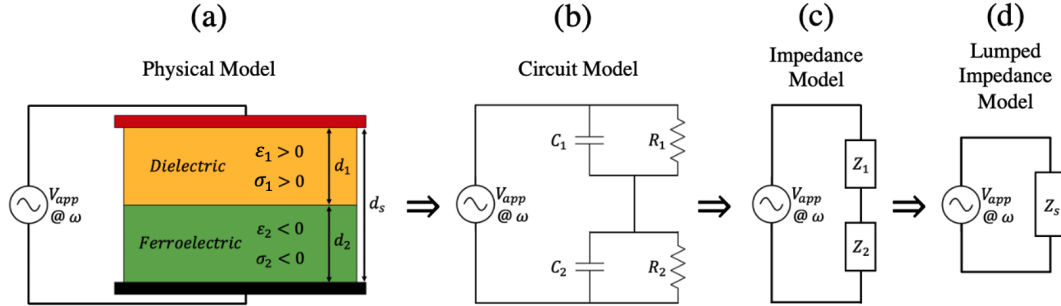


Figure A.3: Circuit-level diagrams depicting of (a) physical model, (b) equivalent circuit model, (c) impedance model, and (d) lumped impedance model.

### A.3.1 Generalized Equivalent Impedance

First, the resistance and capacitance must be defined in terms of known material properties. As such, Equations Equation A.33 and Equation A.34 are obtained from Ohms Law.

$$R_i = \frac{1}{\sigma_i} \frac{d_i}{A} \quad (\text{A.33})$$

$$C_i = \varepsilon_0 \varepsilon_i \frac{A}{d_i} \quad (\text{A.34})$$

Where  $A$  is the area of the parallel plates. Next, the impedance of each parallel RC layer is defined in terms of the resistance and capacitance and this is expanded in terms of only known material parameters as in Equation Equation A.35.

$$Z_i = \frac{1}{j\omega C_i + \frac{1}{R_i}} = \frac{1}{j\omega \varepsilon_0 \varepsilon_i \frac{A}{d_i} + \sigma_i \frac{A}{d_i}} = \left( \frac{1}{A} \right) \frac{d_i}{j\omega \varepsilon_0 \varepsilon_i + \sigma_i} \quad (\text{A.35})$$

Since the permittivity and conductivity of the simulated materials are represented as a single complex permittivity value given by  $\varepsilon_i^* = \varepsilon_i - j\frac{\sigma_i}{\varepsilon_0 \omega}$ , Equation A.35 can be re-written as Equation A.36.

$$Z_i = \left( \frac{-j}{A \varepsilon_0 \omega} \right) \frac{d_i}{\varepsilon_i - j\frac{\sigma_i}{\varepsilon_0 \omega}} = \left( \frac{-j}{A \varepsilon_0 \omega} \right) \left( \frac{d_i}{\varepsilon_i^*} \right) \quad (\text{A.36})$$

Carrying out this derivation with the complex permittivity represented as  $\varepsilon_i^*$  may obscure some of the fundamental physical phenomena expressed in this analytical model. As such, the former expression is used to represent  $Z_i$ . And so, Equation A.37 is used to represent the total complex impedance of the system.

$$Z_s = \sum_{i=1}^N Z_i = \left( \frac{1}{A} \right) \sum_{i=1}^N \left[ \frac{d_i}{j\omega \varepsilon_0 \varepsilon_i + \sigma_i} \right] \quad (\text{A.37})$$

### A.3.2 Effective Composite Permittivity Calculation

With the impedance at each layer and the total lumped impedance, it is now possible to determine the voltage across each layer using Equation A.38, which is based on a simple voltage divider.

$$V_i = V_{app} \left( \frac{Z_i^*}{Z_s^*} \right) \quad (\text{A.38})$$

Knowing this voltage as well as the thickness ( $d_i$ ), it is possible to approximate the internal electric field within each layer using Equation A.39.

$$E_i = \frac{V_i}{d_i} \quad (\text{A.39})$$

Equation A.40 is obtained by combining Equation A.38 and Equation A.39.

$$E_i = \frac{V_{app}}{d_i} \left( \frac{Z_i}{Z_s} \right) \quad (\text{A.40})$$

Plugging in the individual and lumped impedance ( $Z_i$  and  $Z_s$  respectively), Equation A.41 is obtained. Note that the factor ( $\frac{1}{A}$ ) is cancelled as it is identical for both  $Z_i$  and  $Z_s$ .

$$E_1 = \frac{V_{app}}{d_1} \left( \frac{\frac{d_1}{j\omega\varepsilon_0\varepsilon_1+\sigma_1}}{\frac{d_1}{j\omega\varepsilon_0\varepsilon_1+\sigma_1} + \frac{d_2}{j\omega\varepsilon_0\varepsilon_2+\sigma_2}} \right) \quad (\text{A.41})$$

$$E_2 = \frac{V_{app}}{d_2} \left( \frac{\frac{d_2}{j\omega\varepsilon_0\varepsilon_2+\sigma_2}}{\frac{d_1}{j\omega\varepsilon_0\varepsilon_1+\sigma_1} + \frac{d_2}{j\omega\varepsilon_0\varepsilon_2+\sigma_2}} \right) \quad (\text{A.42})$$

From these equations, the total energy ( $\mathbf{E}_{tot}$ ) can be approximated by the summation given in Equation A.43.

$$\mathbf{E}_{tot} = \frac{1}{2} A \varepsilon_0 \sum_{i=1}^N (\varepsilon_i d_i (E_i E_i^*)) \quad (\text{A.43})$$

Where  $|\varepsilon_i^*|$  is the magnitude of the complex permittivity for the  $i^{th}$  material layer. Expanding this out using the two-phase case outlined here, the result takes the form of Equa-

tion A.44.

$$\mathbf{E}_{tot} = \left( \frac{1}{2} A \varepsilon_0 \right) (\varepsilon_1 d_1 (E_1 E_1^*) + \varepsilon_2 d_2 (E_2 E_2^*)) \quad (\text{A.44})$$

With this, it is necessary to obtain the square magnitude of the electric field ( $E_i E_i^*$ ), and to do this, the real and imaginary parts of  $E_i$  must be separable. To this end, the following steps are carried out. First, a common denominator must be obtained in the denominator of the expression using a multiplication by one as in Equation A.45.

$$\begin{aligned} E_1 &= \frac{V_{app}}{d_1} \left( \frac{\frac{d_1}{j\omega\varepsilon_0\varepsilon_1+\sigma_1}}{\frac{d_1}{j\omega\varepsilon_0\varepsilon_1+\sigma_1} + \frac{d_2}{j\omega\varepsilon_0\varepsilon_2+\sigma_2}} \right) \left( \frac{(\sigma_1 + j\omega\varepsilon_0\varepsilon_1)(\sigma_2 + j\omega\varepsilon_0\varepsilon_2)}{(\sigma_1 + j\omega\varepsilon_0\varepsilon_1)(\sigma_2 + j\omega\varepsilon_0\varepsilon_2)} \right) \\ &= \frac{V_{app}}{d_1} \left( \frac{d_1(\sigma_2 + j\omega\varepsilon_0\varepsilon_2)}{d_1(\sigma_2 + j\omega\varepsilon_0\varepsilon_2) + d_2(\sigma_1 + j\omega\varepsilon_0\varepsilon_1)} \right) \end{aligned} \quad (\text{A.45})$$

Then, by rearranging the expression, it is then possible to normalize the denominator and bring all imaginary terms to the numerator as in Equation A.46.

$$\begin{aligned} E_1 &= \frac{V_{app}}{d_1} \left( \frac{d_1\sigma_2 + j\omega\varepsilon_0 d_1\varepsilon_2}{(d_1\sigma_2 + d_2\sigma_1) + j\omega\varepsilon_0(d_1\varepsilon_2 + d_2\varepsilon_1)} \right) \\ &= \frac{V_{app}}{d_1} \left( \frac{d_1\sigma_2 + j\omega\varepsilon_0 d_1\varepsilon_2}{(d_1\sigma_2 + d_2\sigma_1) + j\omega\varepsilon_0(d_1\varepsilon_2 + d_2\varepsilon_1)} \right) \left( \frac{(d_1\sigma_2 + d_2\sigma_1) - j\omega\varepsilon_0(d_1\varepsilon_2 + d_2\varepsilon_1)}{(d_1\sigma_2 + d_2\sigma_1) - j\omega\varepsilon_0(d_1\varepsilon_2 + d_2\varepsilon_1)} \right) \end{aligned} \quad (\text{A.46})$$

Applying the substitution given by Equation A.3.2 then results in Equation A.48

$$\begin{aligned} \alpha &= (d_1\sigma_2 + d_2\sigma_1) \\ \beta &= (d_1\varepsilon_2 + d_2\varepsilon_1) \end{aligned} \quad (\text{A.47})$$

$$E_1 = \frac{V_{app}}{d_1} (d_1) \left( \frac{(\sigma_2\alpha + \omega^2\varepsilon_0^2\beta) + j\omega\varepsilon_0(\varepsilon_2\alpha - \sigma_2\beta)}{\alpha^2 + \omega^2\varepsilon_0^2\beta^2} \right) \quad (\text{A.48})$$

In this form, the expression is easily separable into real and imaginary parts. To fully expand Equation A.44, the square magnitude of  $E_1$  and  $E_2$  must be determined. This is achieved by multiplying the Equation A.44 by its complex conjugate as in Equation A.49

and Equation A.50

$$\begin{aligned} E_1 E_1^* &= (V_{app})^2 \left( \frac{(\sigma_2 \alpha + \omega^2 \varepsilon_2 \varepsilon_0^2 \beta) + j\omega \varepsilon_0 (\varepsilon_2 \alpha - \sigma_2 \beta)}{\alpha^2 + \omega^2 \varepsilon_0^2 \beta^2} \right) \\ &\quad \times \left( \frac{(\sigma_2 \alpha + \omega^2 \varepsilon_2 \varepsilon_0^2 \beta) - j\omega \varepsilon_0 (\varepsilon_2 \alpha - \sigma_2 \beta)}{\alpha^2 + \omega^2 \varepsilon_0^2 \beta^2} \right) \\ &= (V_{app})^2 \left( \frac{(\sigma_2 \alpha + \omega^2 \varepsilon_2 \varepsilon_0^2 \beta)^2 + \omega^2 \varepsilon_0^2 (\varepsilon_2 \alpha - \sigma_2 \beta)^2}{(\alpha^2 + \omega^2 \varepsilon_0^2 \beta^2)^2} \right) \end{aligned} \quad (\text{A.49})$$

$$E_2 E_2^* = (V_{app})^2 \left( \frac{(\sigma_1 \alpha + \omega^2 \varepsilon_1 \varepsilon_0^2 \beta)^2 + \omega^2 \varepsilon_0^2 (\varepsilon_1 \alpha - \sigma_1 \beta)^2}{(\alpha^2 + \omega^2 \varepsilon_0^2 \beta^2)^2} \right) \quad (\text{A.50})$$

By plugging in Equation A.49 and Equation A.50 into Equation A.44, the total energy is expanded to Equation A.51.

$$\begin{aligned} \mathbf{E}_{tot} &= \left( \frac{1}{2} A \varepsilon_0 \right) (\varepsilon_1 d_1 (E_1 E_1^*) + \varepsilon_2 d_2 (E_2 E_2^*)) \\ &= \left( \frac{1}{2} A \varepsilon_0 \right) \left( \frac{\varepsilon_1 d_1 (V_{app})^2 ((\sigma_2 \alpha + \omega^2 \varepsilon_2 \varepsilon_0^2 \beta)^2 + \omega^2 \varepsilon_0^2 (\varepsilon_2 \alpha - \sigma_2 \beta)^2)}{(\alpha^2 + \omega^2 \varepsilon_0^2 \beta^2)^2} \right) \\ &\quad + \left( \frac{\varepsilon_2 d_2 (V_{app})^2 ((\sigma_1 \alpha + \omega^2 \varepsilon_1 \varepsilon_0^2 \beta)^2 + \omega^2 \varepsilon_0^2 (\varepsilon_1 \alpha - \sigma_1 \beta)^2)}{(\alpha^2 + \omega^2 \varepsilon_0^2 \beta^2)^2} \right) \\ &= \left( \frac{A \varepsilon_0 V_{app}^2}{2(\alpha^2 + \omega^2 \varepsilon_0^2 \beta^2)^2} \right) \left( (\varepsilon_1 d_1)((\sigma_2 \alpha + \omega^2 \varepsilon_2 \varepsilon_0^2 \beta)^2 + \omega^2 \varepsilon_0^2 (\varepsilon_2 \alpha - \sigma_2 \beta)^2) \right. \\ &\quad \left. + (\varepsilon_2 d_2)((\sigma_1 \alpha + \omega^2 \varepsilon_1 \varepsilon_0^2 \beta)^2 + \omega^2 \varepsilon_0^2 (\varepsilon_1 \alpha - \sigma_1 \beta)^2) \right) \end{aligned} \quad (\text{A.51})$$

Using the capacitance relationship for the whole two-phase laminate structure as given by Equation Equation A.52, it is possible to determine the effective composite permittivity assuming an ideal parallel plate capacitor structure knowing only the total energy and the known material parameters discussed previously.

$$C_{eff} = \frac{2\mathbf{E}_{tot}}{V_{app}^2} = \varepsilon_0 \varepsilon_{eff} \frac{A}{d_s} \quad (\text{A.52})$$

The resulting equation describing the effective permittivity of the device in terms of the total energy is given by Equation Equation A.53.

$$\varepsilon_{eff} = (\mathbf{E}_{tot}) \frac{2d_s}{A\varepsilon_0 V_{app}^2} \quad (A.53)$$

Now, by substituting Equation A.51 into Equation A.53, Equation A.54 explicitly describes the effective permittivity ( $\varepsilon_{eff}$ ) in terms of the geometric and material properties of the constituent material layers.

$$\begin{aligned} \varepsilon_{eff} = & \left( \frac{2d_s}{A\varepsilon_0 V_{app}^2} \right) \left( \frac{A\varepsilon_0 V_{app}^2}{2(\alpha^2 + \omega^2 \varepsilon_0^2 \beta^2)^2} \right) \\ & \times \left( (\varepsilon_1 d_1)((\sigma_2 \alpha + \omega^2 \varepsilon_2 \varepsilon_0^2 \beta)^2 + \omega^2 (\varepsilon_2 \varepsilon_0 \alpha - \sigma_2 \varepsilon_0 \beta)^2) \right. \\ & \left. + (\varepsilon_2 d_2)((\sigma_1 \alpha + \omega^2 \varepsilon_1 \varepsilon_0^2 \beta)^2 + \omega^2 \varepsilon_0^2 (\varepsilon_1 \alpha - \sigma_1 \beta)^2) \right) \end{aligned} \quad (A.54)$$

Finally, simplifying this expression yields Equation A.55

$$\begin{aligned} \varepsilon_{eff} = & \left( \frac{d_s}{(\alpha^2 + \omega^2 \varepsilon_0^2 \beta^2)^2} \right) \left( (\varepsilon_1 d_1)((\sigma_2 \alpha + \omega^2 \varepsilon_2 \varepsilon_0^2 \beta)^2 + \omega^2 \varepsilon_0^2 (\varepsilon_2 \alpha - \sigma_2 \beta)^2) \right. \\ & \left. + (\varepsilon_2 d_2)((\sigma_1 \alpha + \omega^2 \varepsilon_1 \varepsilon_0^2 \beta)^2 + \omega^2 \varepsilon_0^2 (\varepsilon_1 \alpha - \sigma_1 \beta)^2) \right) \end{aligned} \quad (A.55)$$

$$\alpha = (d_1 \sigma_2 + d_2 \sigma_1)$$

$$\beta = (d_1 \varepsilon_2 + d_2 \varepsilon_1)$$

### A.3.3 Formulation of Design Equations

Examining Equation A.55, it becomes clear that some asymptotic behavior must occur at the point where the denominator is equal to zero, as described by Equation A.56. This expression is then subdivided into two specific conditions that must be met to satisfy the conditions required for polarization catastrophe as given by Equation A.57.

$$\begin{aligned} 0 &= \alpha^2 + \omega^2 \varepsilon_0^2 \beta^2 \\ &= (d_1 \sigma_2 + d_2 \sigma_1)^2 + \omega^2 \varepsilon_0^2 (d_1 \varepsilon_2 + d_2 \varepsilon_1)^2 \end{aligned} \quad (\text{A.56})$$

$$\begin{aligned} \alpha = 0 \quad \Rightarrow \quad (d_1 \sigma_2 + d_2 \sigma_1) &= 0 \quad \Rightarrow \quad \frac{d_1}{d_2} = -\frac{\sigma_1}{\sigma_2} \\ \beta = 0 \quad \Rightarrow \quad (d_1 \varepsilon_2 + d_2 \varepsilon_1) &= 0 \quad \Rightarrow \quad \frac{d_1}{d_2} = -\frac{\varepsilon_1}{\varepsilon_2} \end{aligned} \quad (\text{A.57})$$

This asymptotic behavior is related to negative capacitance, and is known as polarization catastrophe due to the positive feedback that leads to internal polarization at such a magnitude that it can be destructive. For the general case, both expressions given in Equation A.57 must be true as a precondition for catastrophic polarization, but examining Equation A.56, a frequency dependence can be seen. Considering the case where  $\omega = 0$  the DC behavior can be described by Equation A.58.

$$\frac{d_1}{d_2} = -\frac{\sigma_1}{\sigma_2} \quad (\text{A.58})$$

And likewise, considering the case where  $\omega$  is very large, the high-frequency AC behavior can be described by Equation A.59

$$\frac{d_1}{d_2} = -\frac{\varepsilon_1}{\varepsilon_2} \quad (\text{A.59})$$

Therefore, for Equation A.59 to remain true,  $\omega$  must be large enough such that the frequency,  $\omega$ , on the RHS of Equation A.56 is least two orders of magnitude greater than the conductivity components. Therefore, assuming that the constituent phases are insulating (i.e.  $\sigma < 10^{-7}$ ), the frequency  $\omega$  must be at least  $2\pi \times 10^6 \left[ \frac{\text{rad}}{\text{s}} \right]$ . For intermediate cases where  $\omega$  is nonzero, but less than  $10^6$ , the first expression given by Equation A.56 dictates that both  $\alpha$  and  $\beta$  must be equal to zero as in Equation A.57. With this, Equation A.60 provides a piece-wise function that states the required relationship between geometric and material properties to maximize internal voltage amplification due to negative capacitance effects.

$$\frac{d_1}{d_2} \approx \begin{cases} -\frac{\varepsilon_1}{\varepsilon_2} & \forall (\omega > 2\pi \times 10^6 \left[ \frac{\text{rad}}{\text{s}} \right]) \\ -\frac{\sigma_1}{\sigma_2} \ \& \ -\frac{\varepsilon_1}{\varepsilon_2} & \forall (0 < \omega < 2\pi \times 10^6 \left[ \frac{\text{rad}}{\text{s}} \right]) \\ -\frac{\sigma_1}{\sigma_2} & \forall (\omega \approx 0 \left[ \frac{\text{rad}}{\text{s}} \right]) \end{cases} \quad (\text{A.60})$$

## REFERENCES

- [1] B. K. Kim, S. Sy, A. Yu, and J. Zhang, “Electrochemical supercapacitors for energy storage and conversion,” *Handbook of Clean Energy Systems*, pp. 1–25, Jul. 2015.
- [2] M. Peddigari, G. T. Hwang, H. Palneedi, and J. Ryu, “Linear and nonlinear dielectric ceramics for high-power energy storage capacitor applications,” *Journal of the Korean Ceramic Society*, vol. 56, pp. 1–23, 1 2019.
- [3] V. K. T. Prateek and R. K. Gupta, “Recent progress on ferroelectric polymer-based nanocomposites for high energy density capacitors: Synthesis, dielectric properties, and future aspects,” *Chemical Reviews*, vol. 116, pp. 4260–4317, Apr. 2016.
- [4] M. Guo, J. Jiang, Z. Shen, Y. Lin, C.-W. Nan, and Y. Shen, “High-energy-density ferroelectric polymer nanocomposites for capacitive energy storage: Enhanced breakdown strength and improved discharge efficiency,” *Materials Today*, vol. 29, pp. 49–67, 2019.
- [5] H. Luo *et al.*, “Interface design for high energy density polymer nanocomposites,” *Chemical Society Reviews*, vol. 48, no. 16, pp. 4424–4465, 2019.
- [6] X. Hao, “A review on the dielectric materials for high energy-storage application,” *Journal of Advanced Dielectrics*, vol. 03, no. 01, p. 1 330 001, 2013.
- [7] X. Zhang *et al.*, “Giant energy density and improved discharge efficiency of solution-processed polymer nanocomposites for dielectric energy storage,” *Advanced Materials*, vol. 28, no. 10, pp. 2055–2061, Jan. 2016.
- [8] Q. Chen, Y. Shen, S. Zhang, and Q. Zhang, “Polymer-based dielectrics with high energy storage density,” *Annual Review of Materials Research*, vol. 45, no. 1, pp. 433–458, Jul. 2015.
- [9] D. Kang, G. Wang, Y. Huang, P. Jiang, and X. Huang, “Decorating TiO<sub>2</sub> nanowires with BaTiO<sub>3</sub> nanoparticles: A new approach leading to substantially enhanced energy storage capability of high-k polymer nanocomposites,” *ACS Applied Materials & Interfaces*, vol. 10, no. 4, pp. 4077–4085, 2018.
- [10] K. Yu, Y. Niu, Y. Zhou, Y. Bai, and H. Wang, “Nanocomposites of surface-modified BaTiO<sub>3</sub> nanoparticles filled ferroelectric polymer with enhanced energy density,” *Journal of the American Ceramic Society*, vol. 96, pp. 2519–2524, 8 May 2013.
- [11] C. A. Grabowski *et al.*, “Performance of dielectric nanocomposites: Matrix-free, hairy nanoparticle assemblies and amorphous polymer–nanoparticle blends,” *ACS Applied Materials & Interfaces*, vol. 6, no. 23, pp. 21 500–21 509, Nov. 2014.

- [12] Y. Jin, N. Xia, and R. A. Gerhardt, “Enhanced dielectric properties of polymer matrix composites with BaTiO<sub>3</sub> and MWCNT hybrid fillers using simple phase separation,” *Nano Energy*, vol. 30, pp. 407–416, 2016.
- [13] P. Barber *et al.*, “Polymer composite and nanocomposite dielectric materials for pulse power energy storage,” *Materials*, vol. 2, no. 4, pp. 1697–1733, Oct. 2009.
- [14] M. Ejaz *et al.*, “Core-shell structured poly(glycidyl methacrylate)/BaTiO<sub>3</sub> nanocomposites prepared by surface-initiated atom transfer radical polymerization: A novel material for high energy density dielectric storage,” *Journal of Polymer Science Part A: Polymer Chemistry*, vol. 53, no. 6, pp. 719–728, Dec. 2014.
- [15] L. Xie, X. Huang, Y. Huang, K. Yang, and P. Jiang, “Core@double-shell structured BaTiO<sub>3</sub>/sub-polymer nanocomposites with high dielectric constant and low dielectric loss for energy storage application,” *The Journal of Physical Chemistry C*, vol. 117, no. 44, pp. 22 525–22 537, Oct. 2013.
- [16] P. Kim *et al.*, “High energy density nanocomposites based on surface-modified BaTiO<sub>3</sub> and a ferroelectric polymer,” *ACS Nano*, vol. 3, no. 9, pp. 2581–2592, 2009.
- [17] J. Li, J. Claude, L. E. Norena-Franco, S. I. Seok, and Q. Wang, “Electrical energy storage in ferroelectric polymer nanocomposites containing surface-functionalized batio3nanoparticles,” *Chemistry of Materials*, vol. 20, no. 20, pp. 6304–6306, Oct. 2008.
- [18] Q. Li, K. Han, M. R. Gadinski, G. Zhang, and Q. Wang, “High energy and power density capacitors from solution- processed ternary ferroelectric polymer nanocomposites,” *Advanced Materials*, vol. 26, pp. 6244–6249, 2014.
- [19] A. Qureshi, A. Mergen, M. S. Eroğlu, N. L. Singh, and A. Güllüoğlu, “Dielectric properties of polymer composites filled with different metals,” *Journal of Macromolecular Science, Part A*, vol. 45, no. 6, pp. 462–469, Apr. 2008.
- [20] C. Putson *et al.*, “Effects of copper filler sizes on the dielectric properties and the energy harvesting capability of nonpercolated polyurethane composites,” *Journal of Applied Physics*, vol. 109, no. 2, p. 024 104, Jan. 2011.
- [21] L. Qi, B. I. Lee, S. Chen, W. D. Samuels, and G. J. Exarhos, “High-dielectric-constant silver-epoxy composites as embedded dielectrics,” *Advanced Materials*, vol. 17, no. 14, pp. 1777–1781, Jul. 2005.
- [22] J. Xie, M. Yao, W. Gao, Z. Su, and X. Yao, “Significantly enhanced dielectric constant and energy density in au/al<sub>2</sub>o<sub>3</sub> nanocomposite thin films,” *Journal of Alloys and Compounds*, vol. 772, pp. 324–331, Jan. 2019.

- [23] J. Íñiguez, P. Zubko, I. Luk'yanchuk, and A. Cano, "Ferroelectric negative capacitance," *Nature Reviews Materials*, vol. 4, no. 4, pp. 243–256, Mar. 2019.
- [24] A. I. Khan, A. Keshavarzi, and S. Datta, "The future of ferroelectric field-effect transistor technology," *Nature Electronics*, vol. 3, no. 10, pp. 588–597, Oct. 2020.
- [25] M. Hoffmann, S. Slesazeck, T. Mikolajick, and C. S. Hwang, "Chapter 10.5 - negative capacitance in hfo<sub>2</sub>- and zro<sub>2</sub>-based ferroelectrics," in *Ferroelectricity in Doped Hafnium Oxide: Materials, Properties and Devices*, ser. Woodhead Publishing Series in Electronic and Optical Materials, U. Schroeder, C. S. Hwang, and H. Funakubo, Eds., Woodhead Publishing, 2019, pp. 473–493, ISBN: 978-0-08-102430-0.
- [26] M. Hoffmann, S. Slesazeck, and T. Mikolajick, "Progress and future prospects of negative capacitance electronics: A materials perspective," *APL Materials*, vol. 9, no. 2, p. 020 902, 2021. eprint: <https://doi.org/10.1063/5.0032954>.
- [27] Y. Feng *et al.*, "Interfacial negative capacitance in planar perovskite solar cells: An interpretation based on band theory," *Materials Research Bulletin*, vol. 107, pp. 74–79, 2018.
- [28] M. Hoffmann, P. V. Ravindran, and A. I. Khan, "Why do ferroelectrics exhibit negative capacitance?" *Materials*, vol. 12, no. 22, p. 3743, Nov. 2019.
- [29] Z. Wang *et al.*, "Direct observation of stable negative capacitance in SrTiO sub3/sub @BaTiO sub3/sub heterostructure," *Advanced Electronic Materials*, vol. 6, no. 2, p. 1 901 005, Dec. 2019.
- [30] Y. A. Romanov, J. Y. Romanova, and L. G. Mourokh, "Semiconductor superlattice in a biharmonic field: Absolute negative conductivity and static electric-field generation," *Journal of Applied Physics*, vol. 99, no. 1, p. 013 707, Jan. 2006.
- [31] A. I. Khan, U. Radhakrishna, S. Salahuddin, and D. Antoniadis, "Work function engineering for performance improvement in leaky negative capacitance FETs," *IEEE Electron Device Letters*, vol. 38, no. 9, pp. 1335–1338, Sep. 2017.
- [32] C. T.-K. Lew *et al.*, "Investigation of charge carrier trapping in h-terminated diamond devices," *Applied Physics Letters*, vol. 117, no. 14, p. 143 507, Oct. 2020.
- [33] G. He *et al.*, "Solid solution nitride/carbon nanotube hybrids enhance electrocatalysis of oxygen in zinc-air batteries," *Energy Storage Materials*, vol. 15, pp. 380–387, Nov. 2018.
- [34] J. Wang, F. Guan, L. Cui, J. Pan, Q. Wang, and L. Zhu, "Achieving high electric energy storage in a polymer nanocomposite at low filling ratios using a highly po-

- larizable phthalocyanine interphase,” *Journal of Polymer Science Part B: Polymer Physics*, vol. 52, no. 24, pp. 1669–1680, 2014.
- [35] H. Uratani and K. Yamashita, “Charge carrier trapping at surface defects of perovskite solar cell absorbers: A first-principles study,” *The Journal of Physical Chemistry Letters*, vol. 8, no. 4, pp. 742–746, Feb. 2017.
- [36] A. Andersen and J. Dennison, “Mixed weibull distribution model of dc dielectric breakdowns with dual defect modes,” in *2015 IEEE Conference on Electrical Insulation and Dielectric Phenomena (CEIDP)*, 2015, pp. 570–573.
- [37] T. C. Choi, *Effective Medium Theory: Principles and Applications*, Second Edition. Oxford University Press, 2016.
- [38] L. An, S. Boggs, and J. Calame, “Energy storage in polymer films with high dielectric constant fillers - [feature article],” *IEEE Electrical Insulation Magazine*, vol. 24, no. 3, pp. 5–10, May 2008.
- [39] J. P. Calame, “Finite difference simulations of permittivity and electric field statistics in ceramic-polymer composites for capacitor applications,” *Journal of Applied Physics*, vol. 99, no. 8, p. 084 101, Apr. 2006.
- [40] H. Luo *et al.*, “Ultra-high discharged energy density capacitor using high aspect ratio  $\text{Na}_{0.5}\text{Bi}_{0.5}\text{TiO}_3$  nanofibers,” *Journal of Materials Chemistry A*, vol. 5, no. 15, pp. 7091–7102, 2017.
- [41] Z. Wang, J. Keith Nelson, H. Hillborg, S. Zhao, and L. S. Schadler, “Dielectric constant and breakdown strength of polymer composites with high aspect ratio fillers studied by finite element models,” *Composites Science and Technology*, vol. 76, pp. 29–36, 2013.
- [42] E. Y. Wu and R. .-. Vollertsen, “On the weibull shape factor of intrinsic breakdown of dielectric films and its accurate experimental determination. part i: Theory, methodology, experimental techniques,” *IEEE Transactions on Electron Devices*, vol. 49, no. 12, pp. 2131–2140, 2002.
- [43] J. M. Rodríguez-Serna, R. Albarracín-Sánchez, and I. Carrillo, “An improved physical-stochastic model for simulating electrical tree propagation in solid polymeric dielectrics,” *Polymers*, vol. 12, no. 8, p. 1768, Aug. 2020.
- [44] D. Jang and S. Park, “Evaluation of electrical tree degradation in cross-linked polyethylene cable using weibull process of propagation time,” *Energies*, vol. 10, no. 11, p. 1789, Nov. 2017.

- [45] D. Pitsa, G. Vardakis, M. Danikas, and M. Kozako, “Electrical treeing propagation in nanocomposites and the role of nanofillers: Simulation with the aid of cellular automata,” *Journal of Electrical Engineering*, vol. 61, no. 2, pp. 125–128, Mar. 2010.
- [46] X. Huang and P. Jiang, “Core-shell structured high- $\kappa$ /ipolymer nanocomposites for energy storage and dielectric applications,” *Advanced Materials*, vol. 27, no. 3, pp. 546–554, Sep. 2014.
- [47] M. J. Rice and J. Bernasconi, *Gor'kov-eliashberg effect in one-dimensional metals?* Jul. 1972.
- [48] J. A. Davis, D. Brown, and W. Henderson, “Impact of microstructure on dielectric nanocomposites with high- $\kappa$  interfacial layers,” *IEEE Transactions on Nanotechnology*, vol. 14, pp. 717–725, 4 Jul. 2015.
- [49] B. Costello and J.A. Davis, “Quasi-electrostatic simulation of energy density limits and variability in nanoparticle composite materials,” *TechConnect Briefs*, pp. 151–154, Jun. 2019.
- [50] B. Costello and J. A. Davis, “Breakdown field strength variations and energy density limits of nanoparticle composite materials,” *IEEE Transactions on Nanotechnology*, vol. 19, pp. 811–819, 2020.
- [51] J. P. Calame, “Finite difference simulations of permittivity and electric field statistics in ceramic-polymer composites for capacitor applications,” *Journal of Applied Physics*, vol. 99, no. 8, p. 084 101, 2006.
- [52] J. McPherson, J. Kim, A. Shanware, H. Mogul, and J. Rodriguez, “Proposed universal relationship between dielectric breakdown and dielectric constant,” in *Digest, International Electron Devices Meeting*, 2002.
- [53] Z. Feng, Y. Hao, M. Bi, Q. Dai, and K. Bi, “Highly dispersive  $\text{Ba}_{0.6}\text{Sr}_{0.4}\text{TiO}_3$  nanoparticles modified P(VDF-HFP)/PMMA composite films with improved energy storage density and efficiency,” *IET Nanodielectrics*, vol. 1, pp. 60–66, 1 Apr. 2018.
- [54] I. Balberg, D. Azulay, D. Toker, and O. Millo, “Percolation and tunneling in composite materials,” *International Journal of Modern Physics*, vol. 18, pp. 2091–2121, 15 2004.
- [55] T. Prodromakis and C. Papavassiliou, “Engineering the maxwell-wagner polarization effect,” *Applied Surface Science*, vol. 255, no. 15, pp. 6989–6994, May 2009.
- [56] J.A. Davis, D. Brown, and W. Henderson, “Fractal electrode formation in metal-insulator composites near the percolation threshold,” *IEEE Transactions on Nanotechnology*, vol. 12, pp. 725–733, 5 Sep. 2013.

- [57] W. Kahan, *On the cost of floating-point ... - eecs at uc berkeley.*
- [58] S.-T. Tu, W.-Z. Cai, Y. Yin, and X. Ling, *Numerical simulation of saturation behavior of physical properties in composites with randomly distributed second-phase*, Apr. 2005.
- [59] D. Wilkinson, J. S. Langer, and P. N. Sen, “Enhancement of the dielectric constant near a percolation threshold,” *Physical Review B*, vol. 28, no. 2, pp. 1081–1087, 1983.
- [60] C. C. Wang, G. Z. Liu, M. He, and H. B. Lu, “Low-frequency negative capacitance in la<sub>0.8</sub>sr<sub>0.2</sub>mno<sub>3</sub>nb-doped SrTiO<sub>3</sub> heterojunction,” *Applied Physics Letters*, vol. 92, no. 5, p. 052 905, Feb. 2008.
- [61] S. Salahuddin and S. Datta, “Use of negative capacitance to provide voltage amplification for low power nanoscale devices,” *Nano Letters*, vol. 8, no. 2, pp. 405–410, Dec. 2007.
- [62] H. Brandstätter, I. Hanzu, and M. Wilkening, “Myth and reality about the origin of inductive loops in impedance spectra of lithium-ion electrodes — a critical experimental approach,” *Electrochimica Acta*, vol. 207, pp. 218–223, 2016.
- [63] M. Hoffmann, P. V. Ravindran, and A. I. Khan, “A microscopic “toy” model of ferroelectric negative capacitance,” in *2020 4th IEEE Electron Devices Technology & Manufacturing Conference (EDTM)*, IEEE, Apr. 2020.
- [64] J. Zheng *et al.*, “Programmable negative differential resistance effects based on self-assembled au@ppy core–shell nanoparticle arrays,” *Advanced Materials*, vol. 30, no. 35, p. 1 802 731, Jul. 2018.
- [65] A. Ashery, S. A. Gad, A. E. H. Gaballah, and G. M. Turky, “Novel negative capacitance and conductance in all temperatures and voltages of au/CNTs/n-si/al at low and high frequencies,” *ECS Journal of Solid State Science and Technology*, vol. 10, no. 11, p. 111 007, Nov. 2021.
- [66] C. Xu *et al.*, “Tuning the microstructure of batio<sub>3</sub>@sio<sub>2</sub> core-shell nanoparticles for high energy storage composite ceramics,” *Journal of Alloys and Compounds*, vol. 784, pp. 173–181, May 2019.
- [67] K. Bi *et al.*, “Ultrafine core-shell BaTiO<sub>3</sub>@SiO<sub>2</sub> structures for nanocomposite capacitors with high energy density,” *Nano Energy*, vol. 51, pp. 513–523, Sep. 2018.